

**3D radiative transfer in arbitrary
velocity fields:
The Eulerian approach**

Dissertation

**zur Erlangung des Doktorgrades
des Department Physik
der Universität Hamburg**

vorgelegt von

Andreas M. Seelmann

aus Nürtingen

Hamburg

2011

Gutachter der Dissertation:	Prof. Dr. P. Hauschildt Prof. Dr. E. Baron
Gutachter der Disputation:	Prof. Dr. S. Dreizler Prof. Dr. J. Schmitt
Datum der Disputation:	21.04.2011
Vorsitzender des Prüfungsausschusses:	Dr. R. Baade
Vorsitzender des Promotionsausschusses:	Prof. Dr. J. Bartels
Dekan der MIN-Fakultät:	Prof. Dr. H. Graener
Leiter des Department Physik:	Prof. Dr. D. Pfannkuche

This is how 'the physics thing' began...

 **physikbücher**

7. Thomas Hirschberger [Profil anzeigen](#)

Newsgroups: **de.sci.physik**

Von: **Thomas.Hirschber...@physik.uni-muenchen.de** (Thomas Hirs

Datum: **1998/05/06**

Betreff: **Re: physikbücher**

[Antwort an Autor](#) | [Weiterleiten](#) | [Drucken](#) | [Einzelne Nachricht](#) | [Original anzeigen](#)
[Autors suchen](#)

On Sun, 3 May 1998 01:17:54 +0200, "andreas seelmann"

<andreas.seelm...@metronet.de> wrote:

>hallo,

>kennt irgend jemand ein paar gute physik bücher?

>bitte helft mir...

Bisschen wenig konkret gefragt zwar, aber anschaulich und unterhaltsam
sind Feynmans Vorlesungen ueber Physik (Oldenbourg).

Grüß Thomas

[Antwort an Autor](#) [Weiterleiten](#)

Abstract

This work describes the treatment of arbitrary velocity fields in radiative transfer problems with focus on stellar/planetary atmospheres. In general, the influence of velocity fields onto the radiative transfer equations can be described in two reference frames: The Lagrangian and the Eulerian frame. In this thesis, a new Eulerian frame formulation of arbitrary velocity fields in three spatial dimensions is developed including a modified operator splitting scheme in order to handle scattering in the Eulerian frame.

The newly developed method is tested in a two-level atom test framework in spherical geometry. It is compared to a well tested, spatial one dimensional, Lagrangian frame formulation with the help of the general purpose stellar atmosphere code `PHOENIX`. The comparison revealed differences in specific test setups between the two formulations. Those differences were reviewed in detail and constraints on the usability of the Eulerian frame formalism are posed.

After the limitations have been clarified, the Eulerian frame method was modified to handle 'real world' absorption of atoms and molecules in local thermo-dynamical equilibrium. A spectrum of a simple G-type stellar atmosphere with a linearly increasing velocity field in spherical geometry is calculated in both frames and the results are compared.

The Eulerian frame formalism is extended to other, spatial three dimensional, geometries: Cartesian coordinates with and without periodic boundary conditions and cylindrical coordinates. The influence of an atmospheric velocity field onto the spectrum formation is shown for a model atmosphere with atoms and molecules in local thermodynamic equilibrium. This extension of the Eulerian frame formalism allows the computation of spectra from, e.g., solar convection models in cartesian geometry and circumstellar discs models in cylindrical geometry with arbitrary velocity fields.

Then, a snapshot from a solar convection model with an inherent velocity field is used as input into the Eulerian frame radiative transfer calculation and the resulting spectrum is shown. A snapshot from a intermediate global circulation Hot Jupiter model is used as input and the emergent spectra are presented.

The Eulerian frame radiative transfer calculation has been implemented in the stellar atmosphere code `PHOENIX` with two modes: The necessary (opacity) data can be read from a file or kept in memory. The calculation is very time consuming, therefore, an idea of how to speed up the calculation on modern supercomputers is given.

The agreement between the Eulerian and the Lagrangian formalism is shown to be excellent as long as the limitations are considered. The new formulation of arbitrary velocity fields in the Eulerian frame will allow, together with the stellar atmosphere code `PHOENIX`, the computation of three dimensional models of stellar/planetary atmospheres with a correct treatment of arbitrary, atmospheric velocity fields.

Zusammenfassung

Diese Doktorarbeit beschreibt die Behandlung von beliebigen Geschwindigkeitsfeldern in Strahlungstransportproblemen im Hinblick auf Stern-/ Planetenatmosphären. Der Einfluss von Geschwindigkeitsfeldern auf die Strahlungstransportgleichungen kann in zwei Bezugssystemen beschrieben werden: Dem Lagrange und dem Euler Bezugssystem. In dieser Arbeit wird die Behandlung von beliebigen Geschwindigkeitsfeldern in einem räumlich dreidimensionalen Euler Bezugssystem entwickelt sowie ein modifiziertes 'operator splitting' schema um Streuung im Euler Bezugssystem zu berücksichtigen.

Die neue Methode wird in einer zwei-Level Atom Umgebung in sphärische Koordinaten getestet. Sie wird mit Hilfe des Sternatmosphären Codes PHOENIX mit einer 'gut getesteten', räumlich eindimensionalen Lagrange Formulierung verglichen. Im Vergleich ergeben sich Unterschiede für bestimmte Konfigurationen. Diese Unterschiede werden im Detail untersucht und Einschränkungen der Formulierung im Euler Bezugssystem werden aufgestellt.

Nachdem diese Einschränkungen spezifiziert wurden, wird die Behandlung auf Absorption 'echter' Atome und Moleküle im lokalen thermodynamischen Gleichgewicht im Euler Bezugssystem ausgedehnt. Ein Spektrum einer G-Typ Sternatmosphäre mit linear ansteigendem Geschwindigkeitsfeld wird in beiden Bezugssystemen berechnet und verglichen.

Die Formulierung im Euler Bezugssystem wird auf andere, räumlich dreidimensionale Geometrien ausgeweitet: Kartesische Koordinaten mit und ohne periodischen Randbedingungen und Zylinderkoordinaten. Der Einfluss eines atmosphärischen Geschwindigkeitsfeldes auf die Bildung des Spektrums in Modelatmosphären mit Atomen und Molekülen im lokalen thermodynamischen Gleichgewicht wird gezeigt. Diese Erweiterung des Euler Formalismus mit beliebigen Geschwindigkeitsfeldern erlaubt die Berechnung von Spektren von, z.B., solaren Konvektionsmodellen in kartesischen und zirkumstellaren Scheiben in zylindrischen Koordinaten.

Eine Momentaufnahme eines solaren Konvektionsmodells mit Geschwindigkeitsfeld wird als Input in den Euler Formalismus benutzt und das austretende Spektrum wird gezeigt. Eine Momentaufnahme von einem globalen Zirkulationsmodell eines Hot Jupiters wird benutzt und das Spektrum wird gezeigt.

Der Euler Formalismus wurde auf zwei Arten in den Sternatmosphärencode PHOENIX implementiert: Die benötigten (Opazitäts) Daten können aus Dateien oder aus dem Computerspeicher gelesen werden. Die Berechnung ist sehr zeitintensiv, darum wurden Ideen entwickelt, wie man die Rechnung auf modernen Supercomputern beschleunigen kann.

Die Übereinstimmung der Euler zu der Lagrange Formulierung ist exzellent, sofern die Einschränkungen beachtet werden. Die neue Beschreibung von beliebigen Geschwindigkeitsfeldern im Euler Bezugssystem ermöglicht, zusammen mit dem Sternatmosphärencode PHOENIX, 'realistische', dreidimensionale Modelle von Sternatmosphären mit der korrekten Behandlung von beliebigen, atmosphärischen Geschwindigkeitsfeldern.

Contents

1	Introduction	1
2	Basic theory of radiative transfer	5
2.1	General derivation of the radiative transfer equation	5
2.2	Sources and sinks of the radiation field	6
2.2.1	Emission	7
2.2.2	Extinction	7
2.2.3	Scattering	7
2.2.4	Optical depth	8
2.2.5	The source function	8
2.3	Moments of the radiation field	9
2.4	Formal solution and operator splitting	9
2.4.1	The formal solution and the Λ operator	9
2.4.2	Operator splitting	10
2.5	The Redistribution Function	11
2.5.1	Complete Redistribution	12
2.5.2	Coherent Scattering	12
2.6	Thermodynamics: LTE and Non-LTE	12
2.6.1	Local thermodynamic Equilibrium (LTE)	12
2.6.2	Non - local thermodynamic equilibrium (Non-LTE)	13
2.7	Calculation of the Opacity	13
2.7.1	Non-LTE two-level atom with complete redistribution (CRD)	14
2.7.2	Atoms and molecules in LTE	14
3	Radiative transfer in moving atmospheres	17
3.1	Lagrangian formalism	18
3.2	Eulerian formalism	19
4	The stellar atmosphere code PHOENIX	23
4.1	What is PHOENIX in general?	23
4.2	Solid angle integration in 3DRT	24
4.3	The 3D Λ^* Operator	25
4.4	Numerical and geometrical effects of 3DRT	25
4.4.1	Geometrical effects	26
4.4.2	Spatial resolution	27
4.4.3	Angular resolution	29
4.4.4	Cartesian coordinates with PBCs - Limiting the characteristics	32

5	The Eulerian frame versus the Lagrangian frame	33
5.1	Consistency tests of the Eulerian formalism	33
5.2	The testing environment	34
5.3	Results	36
5.4	Limitations of the Eulerian formalism	39
5.4.1	Covering the profile	39
5.4.2	Relativistic effects	41
6	3D Eulerian versus 1D Lagrangian with atoms in LTE	43
6.1	The Atmosphere	43
6.1.1	Shapes of spectral lines	44
6.2	Results	45
6.2.1	The atomic H_α line with Gauss and Voigt profiles	45
6.2.2	More atomic lines with Gauss and Voigt profiles	46
6.2.3	Molecular lines with Gauss and Voigt profiles	47
7	The Eulerian formalism in other geometries	49
7.1	Cartesian with and without PBCs	49
7.1.1	Cartesian with PBCs	50
7.1.2	Cartesian without PBCs	52
7.2	Cylindrical	54
8	Application examples	55
8.1	Three dimensional hydro-dynamical models	55
8.2	A model of solar convection	55
8.3	Hot Jupiter	61
9	Conclusions and Outlook	65
9.1	Conclusions	65
9.2	Outlook and future work	66
A	Implementation in PHOENIX/3D	67
A.1	Domain decomposition in PHOENIX/3D	67
A.2	Numerical performance and storage issues	70
A.2.1	Storage issues	70
A.2.2	Overall speedup	71
A.3	Logical variables regarding the Eulerian frame	73
B	Doppler widths	75
	Acknowledgments	81

Chapter 1

Introduction

Astrophysical research is based on observations of the sky with telescopes on the Earth or in space. The desire to understand and interpret the observed objects in detail lead to complicated theoretical models. This hand in hand process is continuously driven by better observation technics and increased availability of supercomputer power where sophisticated theoretical models can be computed and simplifications in those models can be dropped. This team-work is very enlightening and leads to a lot of interesting results and different interpretations not only in an astrophysical context.

One key element in this co-operation is the theory of radiative transfer which, for example, describes the radiative energy transport within a stellar atmosphere, as only the radiative energy emerging from a stellar object can be observed directly. Major advances in this field were achieved in the 20th and 21th century¹, starting with the classical formulation of the radiation transfer equation by Schuster (1905), which is extensively used in astrophysics. The introduction of operator splitting (Cannon, 1973) and operator perturbation (Scharmer, 1981) methods which accelerate the convergence of the radiation transport equations. The work of Avrett (1965) provided a simple (analytical) environment to analyze line transfer problems, the work of Olson & Kunasz (1987) and Olson et al. (1986) who introduced a short characteristics solution of the line transfer problem. Finally, Hauschildt & Baron (2006), Baron & Hauschildt (2007), Hauschildt & Baron (2008) developed a spatial three dimensional radiative transfer code in different geometries. The interested reader is referred to Wehrse & Kalkofen (2006) and Baron & Hauschildt (2009) for a greater overview on the advances of radiative transfer and radiative transfer in the next decade. It is now possible to obtain 'realistic' three dimensional computer models of radiation transport in stellar/planetary atmospheres (e.g. Hauschildt & Baron, 2010). The computation of those model atmospheres requires substantial amount of computing time.

This work aims to extend three dimensional models of stellar and planetary atmospheres by including the treatment of arbitrary velocity fields in the modeling of radiative transfer. There are several ways to solve the radiative transfer equations in moving atmospheres in spatial one dimension, for example Monte Carlo calculations (Auer & van Blerkom, 1972; Caroff et al., 1972; Magnan, 1970), Sobolev methods (Castor, 1970), tangent ray methods (Mihalas et al., 1976) and the DOME method (Hauschildt & Wehrse, 1991) - modern implementations use iterative techniques based on operator splitting. Furthermore, the problem of how moving atmospheres change the radiative transfer equations

¹only a few milestones are mentioned here

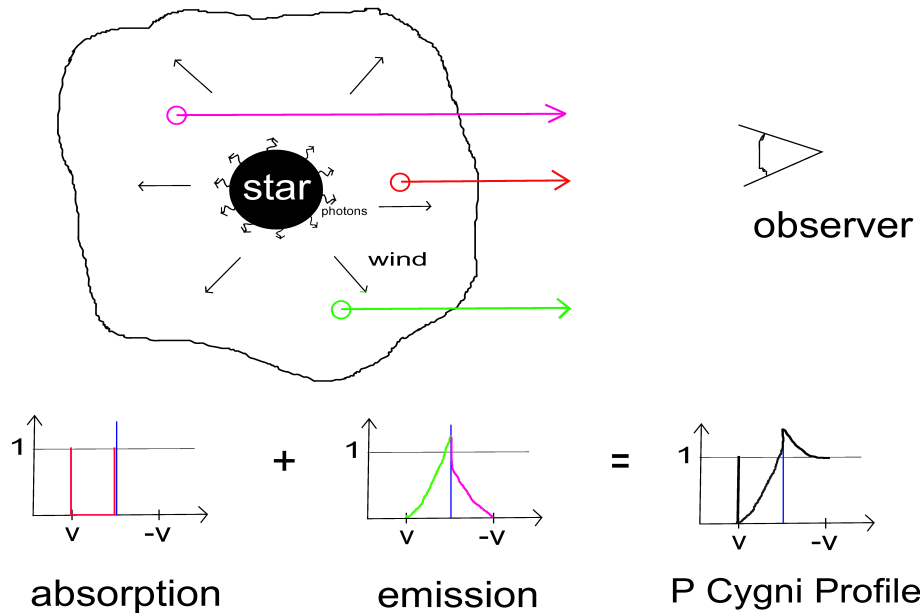


Figure 1.1: P Cygni profile formation, see text for an explanation.

can be described in two reference frames: the Lagrangian (the problem is transferred in the frame moving with the atmosphere) and the Eulerian frame (which is the frame at the rest position of the observer). This work describes iterative methods to solve the radiative transfer equations in the Eulerian frame.

The treatment of velocity fields in stellar atmospheres is fundamental as it can change the emergent spectrum significantly. Evidence of radial expansion or outflow of gas has been known for some time. A prominent example for radial expansion is the star P Cygni which has been observed for more than 400 years (de Groot & Sterken, 2001), the resulting line profiles are called 'P Cygni profile'. Figure 1.1 shows schematically the influence of a radial velocity field onto the spectrum formation. The resulting P Cygni profile consists basically of emission and absorption features arising in different atmospheric regions:

- The part of the atmosphere which is moving towards the observer (red arrow in figure 1.1) produces a blue shifted absorption.
- The atmospheric region in front of the star (green arrow) produces an emission peak with a maximum at the rest wavelength.
- The atmospheric region behind (from the point of view of the observer) the star (purple arrow) also produces an emission peak but often cannot be observed

The combination of those features in the different atmospheric regions gives the typical P Cygni profile as we observe it.

In general, every atmosphere is moving due to thermal motion, expansion, contraction or gas outflow². For example, the sun has no remarkable overall velocity field in a distinguished direction but the convective motion of the atmosphere is translated into line asymmetries in the emergent spectrum (Gray, 2008). The correct treatment of this

²no atmosphere is static

convective motion in the radiative transfer equations is very important for, e.g., the sun. Element abundances are derived from the spectral lines of the sun (Asplund et al., 2005) at very high precision. These abundances values in turn are the standards, which are commonly used in stellar atmosphere modeling.

Nowadays, the search for extrasolar planets is very popular in astrophysical research, starting with the discovery of the first extrasolar planet by Mayor & Queloz (1995). Up to now more than 500 extrasolar planets orbiting a host star have been detected. Those planets are irradiated by their host stars, leading to a day-night energy flow in the atmosphere. The application of the Eulerian frame method in the computation of the emergent radiation field of a hydro-dynamical structure of an extrasolar planet, e.g. Hot Jupiter, will reveal if and how the spectral lines are influenced by that day-night energy flow.

As a baseline of this work, the one dimensional formulation of the treatment of monotonic, radial velocity fields in the Lagrangian frame is used (Hauschildt, 1992*a*). This formulation was used extensively over the last 20 years and has been compared to many observations. Therefore, it provides a good environment to test the newly developed Eulerian frame method.

This thesis is structured as follows: Chapter 2 presents basic theory needed to describe radiative transfer in atmospheres. The basic theory is extended in chapter 3 to handle the influence of a velocity field onto the radiative transfer equations. The one dimensional Lagrangian and the newly developed three dimensional Eulerian frame method are explained there.

To be able to compare the two approaches, a numerical framework has to be used. Chapter 4, therefore, describes properties of the PHOENIX package, in which the Lagrangian frame method is implemented and in which the Eulerian frame method has been implemented for this work.

Chapter 5 presents the comparison of the approaches in a test environment and explains limitations of the Eulerian frame method. In chapter 6, the two approaches are compared in 'real world' applications. As the Lagrangian formalism was developed for supernova applications in spherical geometry, the comparison of the two formalism has been done in spherical geometry.

In order to extend the usability of the Eulerian formalism, it has been also adopted to cartesian³ and cylindrical coordinate systems, presented in chapter 7.

Chapter 8 presents the application of the Eulerian frame formalism in arbitrary velocity fields for an hydro-dynamical structure of the sun and a global circulation, Hot Jupiter model. Finally, chapter 9 gives an outlook to further work.

Appendix A explains the implementation into the stellar atmosphere code PHOENIX and gives an idea of how to optimize the calculations.

³with and without periodic boundary conditions

Chapter 2

Basic theory of radiative transfer

The theory of radiative transfer in astrophysical media is needed to calculate the radiation field within and the radiation emerging from an atmosphere. The radiation emerging from a stellar object can be observed by telescopes on the earth or in space. Therefore, the theory of radiative transfer is the key to understand the formation of spectral lines and the processes that affect them in the atmosphere.

This chapter describes the basic equations needed to solve the radiative transfer problem in three spatial dimensions without the influence of a global velocity field. In section 2.1 a general derivation of the radiative transfer equation is given followed by the physical description of the processes that emit or absorb radiation in section 2.2. Sections 2.3, 2.4 and 2.5 give an overview of the mathematical descriptions of radiation and show the main problem in radiative transfer and also an iterative solution to solve the scattering problem. Sections 2.6 and 2.7 summarize the basic thermodynamic properties of stellar atmospheres and describe the treatment of two-level atoms and atoms in local thermodynamic equilibrium in stellar atmospheres. The theory presented here follows mainly Mihalas (1978), Rutten (2003) and Peraiah (2001) if not mentioned otherwise.

2.1 General derivation of the radiative transfer equation

The energy that passes through a surface element $d\sigma$ in wavelength interval $d\lambda$ into solid angle $d\omega$ may be written as

$$dE_\lambda = I_\lambda(\vec{r}, \vec{\Omega}, t) \cos \theta \, d\sigma \, d\omega \, dt \, d\lambda, \quad (2.1)$$

where $I_\lambda(\vec{r}, \vec{\Omega}, t)$ is the specific intensity at the position \vec{r} in the atmosphere at wavelength λ , θ the angle between the normal to the surface and the direction of the ray $\vec{\Omega}$. We define that radiation with intensity $I_\lambda(\vec{r}, \vec{\Omega}, t)$ in the wavelength interval $d\lambda$, passes in time dt through a volume element of length ds and cross section $d\sigma$ normal to the direction of the ray $\vec{\Omega}$ into the solid angle $d\omega$. Let the intensity of the radiation emerging at $\vec{r} + \Delta\vec{r}$ at the end of time $t + \Delta t$ be $I_\lambda(\vec{r} + \Delta\vec{r}, \vec{\Omega}, t + \Delta t)$. This energy is the difference between the energy absorbed and emitted in the volume element, therefore

$$\begin{aligned} [I_\lambda(\vec{r} + \Delta\vec{r}, \vec{\Omega}, t + \Delta t) - I_\lambda(\vec{r}, \vec{\Omega}, t)] \, d\sigma \, d\omega \, d\lambda \, dt \\ = [\eta_\lambda(\vec{r}, \vec{\Omega}, t) - \chi_\lambda(\vec{r}, \vec{\Omega}, t)] \, ds \, d\omega \, d\lambda \, dt \end{aligned} \quad (2.2)$$

where η_λ and χ_λ are the emission and absorption coefficients respectively, see section 2.2.1 and 2.2.2.

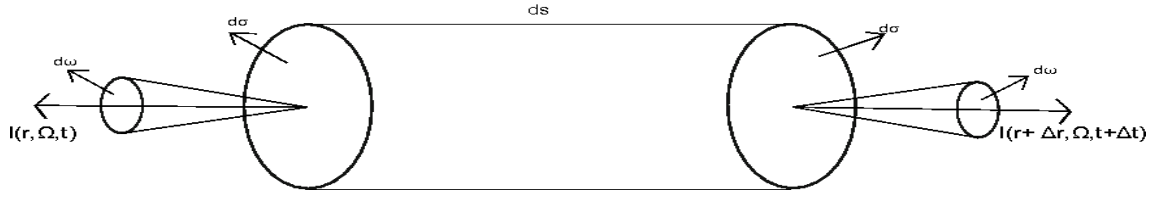


Figure 2.1: Schematic diagram of transfer of radiation

Let s be the path length along a ray of photons passing through this volume element, then $\Delta t = \Delta s/c$ and

$$I_\lambda(\vec{r} + \Delta\vec{r}, \vec{\Omega}, t + \Delta t) - I_\lambda(\vec{r}, \vec{\Omega}, t) = \left(\frac{1}{c} \frac{\partial I_\lambda}{\partial t} + \frac{\partial I_\lambda}{\partial s} \right) ds, \quad (2.3)$$

where c is the speed of light, see figure 2.1 for a schematic diagram. With equations 2.2 and 2.3 we obtain the transfer equation along a beam in the atmosphere

$$\left(\frac{1}{c} \frac{\partial}{\partial t} + \frac{\partial}{\partial s} \right) I_\lambda(\vec{r}, \vec{\Omega}, t) = \eta_\lambda(\vec{r}, \vec{\Omega}, t) - \chi_\lambda(\vec{r}, \vec{\Omega}, t) I_\lambda(\vec{r}, \Omega, t). \quad (2.4)$$

In general, the radiative transfer equation can be written as

$$\frac{1}{c} \frac{\partial I_\lambda}{\partial t} + \vec{\Omega} \cdot \nabla I_\lambda = \eta_\lambda - \chi_\lambda I_\lambda, \quad (2.5)$$

where $\vec{\Omega}$ is the unit vector in the direction of the radiation. In the following we assume time independence and write equation 2.4 as

$$\frac{\partial I_\lambda(\vec{r}, \vec{\Omega})}{\partial s} = \eta_\lambda(\vec{r}, \vec{\Omega}) - \chi_\lambda(\vec{r}, \vec{\Omega}) I_\lambda(\vec{r}, \vec{\Omega}) \quad (2.6)$$

respectively

$$\nabla(\vec{\Omega} I_\lambda(\vec{r}, \vec{\Omega})) = \eta_\lambda(\vec{r}, \Omega) - \chi_\lambda(\vec{r}, \vec{\Omega}) I_\lambda(\vec{r}, \vec{\Omega}). \quad (2.7)$$

Equation 2.6 is a very useful form of the transport equation as it can be tracked through any 3D geometry along a beam s in direction $\vec{\Omega}$.

2.2 Sources and sinks of the radiation field

As photons are moving through the atmosphere, there are multiple ways of how they interact with matter. Those processes are divided in absorption, emission and scattering (more details in section 2.7). The microscopic description of those processes requires knowledge in quantum mechanics and is very complicated for atoms other than hydrogen. Usually, semi-empirical models are utilized to obtain the microscopic quantities of specific atoms and molecules, which are needed to describe the interactions of radiation with matter in a macroscopic manner.

2.2.1 Emission

The description of emission in stellar material is done by introducing a macroscopic emission coefficient $\eta_\lambda(\vec{r}, \vec{\Omega}, t)$ such that the amount of energy added to a beam is described by

$$\delta E = \eta_\lambda(\vec{r}, \vec{\Omega}, t) d\Sigma ds d\omega d\lambda dt, \quad (2.8)$$

where $d\Sigma$ is the geometrical cross-section of the emitting material at position \vec{r} , ds the length of the geometrical path considered in the atmosphere, $d\omega$ the solid angle in which the energy is emitted within a wavelength band $d\lambda$ in direction $\vec{\Omega}$ and in time interval dt . The emission coefficient itself can be divided in emission from particles $\eta_{\lambda,e}$ and scattering of photons $\eta_{s,\lambda}$ into the beam, respectively

$$\eta_\lambda(\vec{r}, \vec{\Omega}, t) = \eta_{\lambda,e}(\vec{r}, \vec{\Omega}, t) + \eta_{\lambda,s}(\vec{r}, \vec{\Omega}, t). \quad (2.9)$$

In terms of intensity, the gain of photons along a beam in the atmosphere can be written as

$$dI_\lambda(\vec{r}, \vec{\Omega}) = \eta_\lambda(\vec{r}, \vec{\Omega}) ds, \quad (2.10)$$

again assuming time independence.

2.2.2 Extinction

The extinction describes the loss of photons in the beam along a geometrical path in the atmosphere. It also consists of two processes: absorption and scattering. The energy decreases along a beam in the atmosphere and we obtain

$$\delta E_\lambda = \chi_\lambda(\vec{r}, \vec{\Omega}, t) I_\lambda(\vec{r}, \vec{\Omega}, t) dS ds d\omega d\lambda dt, \quad (2.11)$$

where

$$\chi_\lambda(\vec{r}, \vec{\Omega}, t) = \kappa_\lambda(\vec{r}, \vec{\Omega}, t) + \sigma_\lambda(\vec{r}, \vec{\Omega}, t) \quad (2.12)$$

is the macroscopic extinction coefficient. $\kappa_\lambda(\vec{r}, \vec{\Omega}, t)$ accounts for the absorption and $\sigma_\lambda(\vec{r}, \vec{\Omega}, t)$ for the scattering, it is assumed that both processes are linear and additive. Assuming time independence, the loss of photons along a beam is written as

$$dI_\lambda(\vec{r}, \vec{\Omega}) = -\chi_\lambda(\vec{r}, \vec{\Omega}) I_\lambda(\vec{r}, \vec{\Omega}) ds. \quad (2.13)$$

The extinction coefficient summarizes the atomic absorption cross-sections multiplied by the number densities of the absorbers summed over all states that can interact with a photon at a certain wavelength λ and adds the removal of photons due to scattering to the total extinction. Therefore, $1/\chi_\lambda$ is the mean free path of photons in the atmosphere at wavelength λ .

2.2.3 Scattering

Scattering occurs in stellar atmospheres and, depending on the energy, temperature, pressure, etc. different kinds of scattering can occur. For low energy photons and free electrons, Thompson scattering, which is independent of the wavelength λ , is relevant:

$$\sigma_\lambda^T = \sigma^T = \frac{8\pi}{3} r_e^2 = 6.65 \times 10^{-25} \text{ cm}^2. \quad (2.14)$$

Scattering of photons by bound electrons is described by Rayleigh scattering. For photons with $\lambda \ll \lambda_0$ scattered by electrons bound with a characteristic binding energy $h\lambda_0$, we can write

$$\sigma^R \approx f_{lu} \sigma^T \left(\frac{\lambda}{\lambda_0} \right)^4, \quad (2.15)$$

with the oscillator strength f_{lu} and wavelength λ_0 characterizing the major bound-bound "resonance transition" of the bound electrons. Absorption and instant emission of a photon by an atom accounts also for scattering because no energy is imparted to the material.

To describe scattering in a realistic manner, it is important to account for the redirection of the photon after the scattering event and a possible shift in the photon's wavelength. In stellar atmosphere problems, the redistribution function is introduced to describe the contribution of scattering to a beam at a given wavelength into a given direction, see section 2.5.

2.2.4 Optical depth

It is convenient to define the optical depth along a path (s, s') in direction $\vec{\Omega}$ to account for the total extinction along a beam. With equation 2.12 we may write

$$\tau_\lambda(s, s') = - \int_s^{s'} \chi_\lambda(s) ds, \quad (2.16)$$

where s is the geometrical path in the atmosphere. τ_λ can also be considered to be the number of mean free paths in the atmosphere.

2.2.5 The source function

To account for the net change of radiation passing through a volume element, we introduce the source function S . With the total emissivity $\eta_\lambda(\vec{r}, \vec{\Omega})$ and the total extinction $\chi_\lambda(\vec{r}, \vec{\Omega})$, we define

$$S_\lambda(\vec{r}) = \frac{\eta_\lambda(\vec{r}, \vec{\Omega})}{\chi_\lambda(\vec{r}, \vec{\Omega})}. \quad (2.17)$$

With this definition and equation 2.16, we can write the transfer equation 2.6 in its standard form

$$\frac{\partial I_\lambda(\vec{r}, \vec{\Omega})}{-\chi_\lambda(\vec{r}, \vec{\Omega}) \partial s} = \frac{\partial I_\lambda(s, s')}{\partial \tau_\lambda(s, s')} = I_\lambda(s, s') - S_\lambda(s, s') \quad (2.18)$$

along a beam (s, s') in the atmosphere.

If we, for example, consider thermal emission $\kappa_\lambda B_\lambda$, absorption κ_λ and coherent scattering σ_λ at a specific point in the atmosphere, we can write the source function (omitting the s dependence) as

$$S_\lambda = \frac{\kappa_\lambda}{\kappa_\lambda + \sigma_\lambda} B_\lambda + \frac{\sigma_\lambda}{\kappa_\lambda + \sigma_\lambda} J_\lambda \quad (2.19)$$

where B_λ is the Planck function and J_λ the mean intensity (see section 2.3) at wavelength λ . This equation can be recast into

$$S_\lambda = \epsilon_\lambda B_\lambda + (1 - \epsilon_\lambda) J_\lambda, \quad (2.20)$$

with the thermal coupling parameter ϵ_λ defined as

$$\epsilon_\lambda = \frac{\kappa_\lambda}{\kappa_\lambda + \sigma_\lambda}. \quad (2.21)$$

This parameter describes the coupling of the radiation field to the thermal pool of the stellar material, e.g., with no scattering in the atmosphere the thermal emission equals the thermal absorption and $\epsilon_\lambda = 1$, thus $S_\lambda = B_\lambda$. It should be noted that every source function can be recast into the general form of equation 2.20.

2.3 Moments of the radiation field

It is common to define higher moments of the specific intensity I in terms of integrals over solid angle. The mean intensity J , is defined as

$$J_\lambda(\vec{r}) = \frac{1}{4\pi} \oint_{4\pi} I_\lambda(\vec{r}, \vec{\Omega}) d\Omega = \frac{1}{4\pi} \int_0^{2\pi} \int_{-1}^{+1} I_\lambda(\vec{r}, \vec{\Omega}) d\mu d\phi \quad (2.22)$$

with the solid angle $d\Omega = \sin\theta d\theta d\phi = -d\mu d\phi$ and $\mu = \cos\theta$, the common abbreviation in radiative transfer theory. The flux is defined as a vector, which accounts for the net radiative energy flux to an arbitrary orientated surface $d\sigma$ per time and wavelength. In cartesian geometry, we obtain

$$\vec{F}_\lambda(\vec{r}) = \oint I_\lambda(\vec{r}, \vec{\Omega}) \vec{n} d\Omega = \int_0^{2\pi} \int_{-1}^{+1} (I_\lambda(\vec{r}, \vec{\Omega}) p_x, I_\lambda(\vec{r}, \vec{\Omega}) p_y, I_\lambda(\vec{r}, \vec{\Omega}) p_z) d\mu d\phi, \quad (2.23)$$

where p_x, p_y and p_z are the unit vectors. In spherical symmetry, where μ is the azimuth angle, the flux in the radial direction is written as

$$\vec{F}_\lambda^r(\vec{r}) = \oint I_\lambda(\vec{r}, \vec{\Omega}) \mu d\Omega = \oint I_\lambda(\vec{r}, \vec{\Omega}) \cdot \mu \cdot d\mu d\phi. \quad (2.24)$$

It is possible to define higher order moments of the intensity which are yielding more insight in the physical atmospheric properties for particular problems or are reducing the complexity of the problem. As they are not used in this thesis, the reader is referred to literature (for example Mihalas, 1978; Rutten, 2003).

2.4 Formal solution and operator splitting

2.4.1 The formal solution and the Λ operator

Equation 2.18 can formally be solved by introducing an integrating factor $\exp(-\tau)$, integration along a path $s = s(\vec{\Omega})$ yields

$$I_\lambda(s) = I_\lambda(0) \exp[-\tau(s, 0)] + \int_0^s S_\lambda(s') \exp[-\tau_\lambda(s, s')] \chi_\lambda(s') ds'. \quad (2.25)$$

Equation 2.25 gives the *formal solution* along beams in the atmosphere, we can rewrite this equation in a *localized form* (Olson & Kunasz, 1987) using piecewise integration:

$$I_\lambda(\tau_i) = I_\lambda(\tau_{i-1}) \exp(-\Delta\tau_i) + \Delta I_{i,\lambda}(S) \quad (2.26)$$

where

$$\Delta I_{i,\lambda}(S) = \alpha_i S_{i-1} + \beta_i S_i + \gamma_i S_{i+1}. \quad (2.27)$$

The indices i label the volume elements through which the beam is passing in the atmosphere and the coefficients α, β, γ are τ dependent and can be found in Olson & Kunasz

(1987). Furthermore, they depend on either a linear or parabolic interpolation of the source function between the volume elements. $\Delta\tau_i$ is the optical depth between the volume elements, calculated, e.g., by using piecewise linear interpolation of the opacity along the beam:

$$\Delta\tau_{i-1} = (\chi_{i-1} + \chi_i) \cdot |s_{i-1} - s_i|/2. \quad (2.28)$$

With equation 2.26 the formal solution can be obtained in numerical models in any three dimensional geometry.

The mean intensity J_λ is given by

$$J_\lambda = \Lambda_\lambda[S_\lambda], \quad (2.29)$$

where Λ_λ is the scattering operator. The construction in three spatial dimensions is explained in detail in section 4.3. The Λ operator consists of angle-dependent contributions $\Lambda_{\mu,\phi}$:

$$\Lambda = \int_0^{2\pi} \int_{-1}^{+1} \Lambda_{\mu,\phi} d\mu d\phi. \quad (2.30)$$

Generally, any procedure that delivers J_λ from S_λ may be regarded as a Λ operator. In a more general sense, it is possible to define a Λ operator which delivers the intensity I from S rather than just the angle-averaged mean intensity.

Equation 2.25 is called a **formal solution** because the source function S generally depends on the radiation field through equation 2.19 whereas the radiation field itself depends upon the source function, a solution can be found iterative: Rewriting equation 2.20 with equation 2.29, dropping all indices, into

$$S = (1 - \epsilon)\Lambda[S] + \epsilon B. \quad (2.31)$$

See next section for a solution.

2.4.2 Operator splitting

The classical idea to solve equation 2.31 is to 'Lambda-iterate' this expression as

$$S_\lambda^{n+1} = (1 - \epsilon_\lambda)\Lambda_\lambda[S_\lambda^n] + \epsilon_\lambda B_\lambda, \quad (2.32)$$

starting with a initial guess S^1 , for example $S^1 = B$ to a prescribed accuracy. The classical Λ iteration fails in the case of large optical depths and small ϵ_λ . The failure is caused by the fact that the largest eigenvalue of the amplification matrix is approximately $\lambda_{\max} \approx (1 - \epsilon)(1 - T^{-1})$ (Mihalas et al., 1975), where T is the optical thickness. For small ϵ and large T , this is very close to unity. Thus, the convergence rate of the iteration is very poor, for a physical description of this effect see Mihalas (1980). A solution can be found by operator splitting.

To solve the slow convergence properties of the Λ iteration, Cannon (1973), Scharmer (1981) introduced Λ -like operators. We split the Λ operator

$$\Lambda_\lambda = \Lambda_\lambda^* + (\Lambda_\lambda - \Lambda_\lambda^*), \quad (2.33)$$

the mean intensity, equation 2.29, is then given by

$$J_\lambda = \Lambda_\lambda^*[S_\lambda] + (\Lambda_\lambda - \Lambda_\lambda^*)[S_\lambda]. \quad (2.34)$$

Rewriting this equation with the unknown source function S^{new} gives

$$J_{\lambda}^{\text{new}} = \Lambda_{\lambda}^*[S_{\lambda}^{\text{new}}] + (\Lambda_{\lambda} - \Lambda_{\lambda}^*)[S_{\lambda}^{\text{old}}]. \quad (2.35)$$

Both equations are equivalent in the case of convergence. After some algebra the new mean intensity is found to be

$$J_{\lambda}^{\text{new}} = [1 - (1 - \epsilon_{\lambda})\Lambda_{\lambda}^*]^{-1} \left\{ J_{\lambda}^{\text{FS}} - \Lambda_{\lambda}^* [(1 - \epsilon_{\lambda})J_{\lambda}^{\text{old}}] \right\} \quad (2.36)$$

where $J^{\text{FS}} = \Lambda[S^{\text{old}}]$ is the mean intensity from the formal solution. The 'approximate Λ operator' Λ^* can, in principle, be chosen freely. The best convergence can be achieved with elements from the original operator (Olson et al., 1986). The whole procedure reduces the eigenvalues of the Λ operator due to a decrease of the diagonal elements (Hauschildt, 1992*b*; Hauschildt et al., 1994), which leads to an accelerated iteration which prevents false convergence. The iteration can further be accelerated using methods such as described by Ng (1974).

2.5 The Redistribution Function

In general, when a photon with wavelength λ and direction \vec{n} is scattered it will have a different wavelength λ' and a different propagation direction \vec{n}' . These changes are described by the redistribution function:

$$R(\lambda', \vec{n}' | \lambda, \vec{n}) d\lambda' d\lambda (d\omega'/4\pi) (d\omega/4\pi), \quad (2.37)$$

which gives the probability that a photon with direction \vec{n}' in solid angle $d\omega'$ and wavelength λ' is scattered in direction \vec{n} in solid angle $d\omega$ and wavelength λ . The redistribution function is normalized such that

$$(4\pi)^{-2} \oint d\omega' \oint d\omega \int_0^{\infty} d\lambda' \int_0^{\infty} d\lambda R(\lambda', \vec{n}' | \lambda, \vec{n}) = 1. \quad (2.38)$$

The energy of emitted or absorbed line photons is not sharp but described by profile functions which are, in general, different from each other. To obtain the emission profile ψ , the Redistribution function must be integrated over all incoming wavelengths and solid angle whereas the absorption profile ϕ is obtained by integrating over all outgoing wavelengths

$$\psi(\lambda', \vec{n}') = \oint \int R(\lambda, \lambda'; \vec{n}, \vec{n}') d\lambda d\omega / (4\pi), \quad (2.39)$$

$$\phi(\lambda', \vec{n}') = \oint \int R(\lambda, \lambda'; \vec{n}, \vec{n}') d\lambda' d\omega' / (4\pi). \quad (2.40)$$

It is very difficult to treat scattering in the generality of equations 2.39 and 2.40. Simplifications can be made to reduce the complexity of the problem, for example, the angle-average redistribution function can be written as

$$R(\lambda', \lambda) = \frac{1}{4\pi} \oint R(\lambda', \vec{n}' | \lambda, \vec{n}) d\omega' = \frac{1}{4\pi} \oint R(\lambda', \vec{n}' | \lambda, \vec{n}) d\omega, \quad (2.41)$$

which gives the redistribution probability from $(\lambda', \lambda' + d\lambda')$ to $(\lambda, \lambda + d\lambda)$.

2.5.1 Complete Redistribution

When atoms are strongly perturbed by collisions during the scattering process so that the excited atoms are randomly distributed over sub-states of the upper level, both the absorption and emission probabilities are independently proportional to the number of sub-states available at each wavelength of the line. The joint probability $R(\lambda', \lambda)$ is then the product of those two independent distributions

$$R(\lambda', \lambda) = \phi(\lambda')\phi(\lambda) \quad (2.42)$$

and is called Complete Redistribution if $\phi(\lambda') = \phi(\lambda)$ holds.

2.5.2 Coherent Scattering

When the photons are scattered by large particles, for example in planetary atmospheres, it is assumed that the scattering is coherent $\lambda' = \lambda$. The redistribution function is then simply

$$R(\lambda', \lambda) = \phi(\lambda')\delta(\lambda - \lambda'), \quad (2.43)$$

where $\delta(\lambda - \lambda')$ is the delta function.

2.6 Thermodynamics: LTE and Non-LTE

Atmospheres consist of regions with high temperature and low density, therefore the gas is mainly composed of single atoms, ions and free electrons. In cooler stars, molecules can form. At these densities the gas behaves as an ideal gas. The state of the gas is completely described if the level-occupation numbers of all atoms and molecules are known, which is also necessary to calculate the opacity. One approach to achieve this is to apply the equilibrium relations of statistical mechanics and thermodynamics at the local values of the (gas) temperature and density. This assumption is called the local thermodynamic equilibrium (LTE). However, as stars in general have intense radiation fields which dominates the occupation numbers, the radiative rates (see section 2.6.2) dominate the collisional rates and LTE does not hold. On the other side, the radiation field depends on the occupations numbers. This is one of the essential difficulties of radiative transfer problems. In this case the occupation numbers must be determined from equations of statistical equilibrium, this approach is called Non-LTE, and the solution requires a self-consistent simultaneous solution of both the radiative transfer and the statistical equilibrium equations.

2.6.1 Local thermodynamic Equilibrium (LTE)

In LTE, the excitation distribution of the atoms and molecules is described by the *Boltzmann excitation formula*:

$$\left[\frac{n_{r,s}}{n_{r,t}} \right]_{\text{LTE}} = \frac{g_{r,s}}{g_{r,t}} \exp[-(\chi_{r,s} - \chi_{r,t})/kT], \quad (2.44)$$

where k is the Boltzmann constant, T the temperature, $n_{r,s}$ is the number of atoms in level s of ionization stage r , $g_{r,s}$ the corresponding statistical weight and $\chi_{r,s}$ the excitation energy of level s in stage r measured from the ground level ($r, 1$). The *Saha distribution* describes the population ratio between the ground states of successive ionization states:

$$\left[\frac{n_{r+1,1}}{n_{r,1}} \right]_{\text{LTE}} = \frac{1}{N_e} \frac{2g_{r+1,1}}{g_{r,1}} \left(\frac{2\pi m_e kT}{h^2} \right)^{\frac{3}{2}} \exp(-\chi_r/kT), \quad (2.45)$$

with N_e as the electron density, h is Planck's constant, m_e the electron mass, $n_{r+1,1}$ and $n_{r,1}$ the population densities of the two ground states of the successive ionization stages r and $r + 1$, χ_r the ionization energy of stage r and $g_{r+1,1}$, $g_{r,1}$ the statistical weights of the two ground states.

Using the local temperature in equation 2.45 gives the occupation numbers of the levels and, therefore, the complete state of the gas is known.

2.6.2 Non - local thermodynamic equilibrium (Non-LTE)

To account for the influence of the radiation field upon the stellar material and thus the level populations, the equations of statistical equilibrium must be applied. The level populations are now permitted to differ from the local Saha-Boltzmann values. Statistical equilibrium implies that the level populations and the radiation field in all directions does not change with time:

$$\frac{dn_i(\vec{r})}{dt} = \sum_{j \neq i}^N n_j(\vec{r})P_{ji}(\vec{r}) - n_i(\vec{r}) \sum_{j \neq i}^N P_{ij}(\vec{r}) = 0, \quad (2.46)$$

where n_i is the population of a particular level, N the total number of levels that are important for the population of level n_i one way or another. The transition rates P_{ij} for radiative and collisional processes are given per particle in state i or j by

$$P_{ij} = R_{ij} + C_{ij}. \quad (2.47)$$

R_{ij} is the radiative rate and C_{ij} the collisional rate. They are directly connected to the atomic and molecular properties of the composing stellar material (see e.g. Mihalas, 1970)

2.7 Calculation of the Opacity

To calculate the opacity χ or emissivity η at a given wavelength, all relevant transitions of all atoms and molecules of the composing material must be considered. This is, without any simplifications, computationally very time consuming and vast databases must be processed which hold the atomic or molecular line data. Transitions can be divided in emission and extinction transitions depending on whether a photon is removed or added to the beam:

- (a) thermal extinction \rightarrow radiative extinction by a beam photon followed by collisional de-excitation
- (b) spontaneous scattering extinction \rightarrow radiative excitation by a beam photon followed by spontaneous de-excitation
- (c) induced scattering extinction \rightarrow radiative excitation by a beam photon followed by induced de-excitation
- (d) spontaneous thermal emission \rightarrow collisional excitation followed by spontaneous emission of a photon
- (e) induced thermal emission \rightarrow collisional excitation followed by induced emission of a photon into the beam

- (f) spontaneous scattering emission \rightarrow radiative excitation followed by spontaneous emission of a photon into the beam
- (g) induced scattering emission \rightarrow radiative excitation followed by induced emission of a photon into a beam

The transition probabilities are given by the Einstein coefficients which are related to the atomic or molecular oscillator strengths and can be calculated with quantum mechanics or obtained via experiments.

2.7.1 Non-LTE two-level atom with complete redistribution (CRD)

Avrett (1965) published an analytical solution of the treatment of hypothetical non-LTE two-level atoms with complete redistribution in stellar atmosphere problems. Assuming that the whole atmosphere consists of the same atoms with only one transition $1 \rightarrow 2$, the statistical equilibrium equation 2.46 is written as

$$\frac{dn_2}{dt} = n_1 P_{12} - n_2 P_{21} = 0. \quad (2.48)$$

With the assumption of complete redistribution and the consideration of possible transitions explained in section 2.7, the line source function, S_λ^l , can be written as

$$\begin{aligned} S_\lambda^l &= \frac{\bar{J} + \epsilon'_\lambda B_\lambda}{1 + \epsilon'_\lambda} \\ &= (1 - \epsilon'_\lambda) \bar{J} + \epsilon'_\lambda B \end{aligned} \quad (2.49)$$

with

$$\bar{J} = \int_0^\infty J_\lambda \phi_\lambda d\lambda. \quad (2.50)$$

Considering a background continuum, the total source function can be written as

$$S_\lambda^{\text{total}} = \frac{\chi_\lambda^l S_\lambda^l + \chi_\lambda^c S_\lambda^c}{\chi_\lambda^l + \chi_\lambda^c}, \quad (2.51)$$

where S_λ^c is the continuum source function and χ_λ^c the continuum opacity, respectively. The line opacity χ_λ^l is parameterized by the ratio of the profile averaged line opacity $\chi_\lambda^l \equiv \chi_\lambda^{l,\phi}$ to the continuum opacity χ_λ^c

$$x = \frac{\chi_\lambda^{l,\phi}}{\chi_\lambda^c} \rightarrow \chi_l = x \cdot \chi_c. \quad (2.52)$$

For complete redistribution the iteration scheme 2.36 must be carried out with $J_\lambda \equiv \bar{J}$ and $\Lambda_\lambda^* \equiv \bar{\Lambda}^*$ where

$$\bar{\Lambda}^* = \int_0^\infty \Lambda_\lambda^* \phi_\lambda d\lambda. \quad (2.53)$$

2.7.2 Atoms and molecules in LTE

In general, the calculation of the opacity is much more complicated than the simple two-level atom. If the whole problem must be treated in non-LTE it is implied that statistical equilibrium must be considered and the population densities of the atomic levels are given by the rate equations 2.47. This is computationally very time consuming and currently not feasible in three spatial dimensions.

A first simplification of the problem is the assumption of LTE which allows the application of the equations in section 2.6.1. The line extinction coefficient with induced emission correction in LTE is given by

$$[\chi_\lambda^l]^{\text{LTE}} = \frac{\pi e^2}{m_e c} n_l^{\text{LTE}} f_{lu} [1 - \exp(-h\lambda_0/kT)] \phi(\lambda - \lambda_0), \quad (2.54)$$

where n_l^{LTE} is the LTE population density, f_{lu} the oscillator strength of transition $l \rightarrow u$ and $\phi(\lambda - \lambda_0)$ the profile of the line. The line extinction coefficient must be calculated for every volume element in the three dimensional grid. The profile of the line $\phi(\lambda - \lambda_0)$ can be approximated with a Voigt profile and under certain circumstances with a Gaussian shaped profile.

Chapter 3

Radiative transfer in moving atmospheres

Radiative transfer in moving atmospheres is a research field in astrophysics which is still under development. The problem of how moving atmospheres change the radiation field and, thus, the emergent spectrum of stellar atmospheres can be described in two reference frames:

1. The observers frame in which the radiation field is computed at the observer's position with respect to the center of the star. This approach is called Eulerian formalism.
2. The co-moving frame which is the frame moving locally with the gas. This approach is called Lagrangian formalism.

The Lagrangian formalism has the advantage that the opacity and the emissivity are isotropic but all wavelengths are coupled whereas, in the Eulerian formalism, the opacities have a complicated anisotropic profile - until now no solution of three dimensional radiative transfer in arbitrary velocity fields in the co-moving frame has been published. In arbitrary velocity fields, the Eulerian formalism has the advantage that there is no coupling to higher or lower wavelengths and, therefore, the calculation at one wavelength point can be done independently of all the others. In the Lagrangian frame, the exact memory demands are known when a solution in three spatial dimensions is published.

In one spatial dimension Hauschildt (1992*a*) developed a solution in the Lagrangian frame with relativistic monotonic velocity fields using an operator splitting technique. Baron & Hauschildt (2004) extended this approach to arbitrary velocity fields in one spatial dimension and finally Baron et al. (2009) developed a solution in three spatial dimension but with the restriction to homologous flows. A further extend to arbitrary velocity fields is under development by Baron and Hauschildt and should be published soon. For comparison, this work uses the Hauschildt (1992*a*) approach with monotonic velocity fields in one spatial dimension. This method is tested extensively and the results were compared to observations in the past years.

This chapter describes the Lagrangian approach of Hauschildt (1992*a*) in one spatial dimension in section 3.1 and then proceeds to the spatial three dimensional description of arbitrary velocity fields in the Eulerian frame in section 3.2.

3.1 Lagrangian formalism

The transfer equation in the co-moving frame was first posed by McCrea & Mitra (1936) and solved by various authors. Mihalas (1980) showed that the frequency-integrated moment equations are equivalent to the four-divergence of the radiation stress-energy tensor and obtained the same results as Castor (1972). The co-moving frame equation in a spherically symmetric medium may, therefore, be written as

$$\begin{aligned} \gamma(\mu + \beta) \frac{\partial I}{\partial r} + \frac{\partial}{\partial \mu} \left\{ \gamma(1 - \mu^2) \left[\frac{1 + \beta\mu}{r} - \gamma^2(\mu + \beta) \frac{\partial \beta}{\partial r} \right] I \right\} - \\ \frac{\partial}{\partial \nu} \left\{ \gamma \left[\frac{\beta(1 - \mu^2)}{r} + \gamma^2 \mu(\mu + \beta) \frac{\partial \beta}{\partial r} \right] \nu I \right\} + \\ \gamma \left\{ \frac{2\mu + \beta(3 - \mu^2)}{r} + \gamma^2(1 + \mu^2 + 2\beta\mu) \frac{\partial \beta}{\partial r} \right\} I = \eta - \chi I, \end{aligned} \quad (3.1)$$

with r the radius, ν the frequency, $I = I(r, \nu, \mu)$ the specific intensity at radius r , frequency ν and angle $\mu = \cos \theta$, $\beta = v/c$ where c is the speed of light and γ is given by $\gamma = 1/\sqrt{1 - \beta^2}$. The relation between the observers and co-moving frame is obtained by applying the Lorentz transformation (see Mihalas, 1970). The opacity, emissivity and the intensity are given by

$$I(\mu, \nu) = (\nu/\nu_0)^3 I_0(\mu_0, \nu_0) \quad (3.2)$$

$$\chi(\mu, \nu) = (\nu/\nu_0) \chi_0(\nu_0) \quad (3.3)$$

$$\eta(\mu, \nu) = (\nu/\nu_0)^2 \eta_0(\nu_0) \quad (3.4)$$

where the suffix zero denotes the quantities in the co-moving frame. For the co-moving frame frequencies and angles we find

$$\nu_0 = \nu \gamma (1 - \beta \mu) \quad (3.5)$$

$$\mu_0 = \frac{\mu - \beta}{1 - \beta \mu}. \quad (3.6)$$

Note the anisotropy of the absorption (3.3) and the emissivity (3.4) in the observer's frame due to equation 3.5.

Rewriting equation 3.1 in wavelength scale gives

$$a_r \frac{\partial I}{\partial r} + a_\mu \frac{\partial I}{\partial \mu} + a_\lambda \frac{\partial \lambda I}{\partial \lambda} + 4a_\lambda I = \eta - \chi I \quad (3.7)$$

with

$$a_r = \gamma(\mu + \beta), \quad (3.8)$$

$$a_\mu = \gamma(1 - \mu^2) \left[\frac{1 + \beta\mu}{r} - \gamma^2(\mu + \beta) \frac{\partial \beta}{\partial r} \right], \quad (3.9)$$

$$a_\lambda = \gamma \left[\frac{\beta(1 - \mu^2)}{r} + \gamma^2 \mu(\mu + \beta) \frac{\partial \beta}{\partial r} \right]. \quad (3.10)$$

Along a geometrical path with a specific direction in the atmosphere (from now on: characteristic) equation 3.7 is written as

$$\frac{\partial I}{\partial s} + a_\lambda \frac{\partial \lambda I}{\partial \lambda} = \eta - (\chi + 4a_\lambda) I \quad (3.11)$$

where s is the geometrical path length along a ray. The characteristics are then given by

$$\frac{dr}{ds} = a_r, \quad (3.12)$$

$$\frac{d\mu}{ds} = a_\mu. \quad (3.13)$$

For monotonic velocity fields the wavelength derivative in equation 3.11 can be discretized with a fully implicit method as

$$\left. \frac{\partial \lambda I}{\partial \lambda} \right|_{\lambda=\lambda_l} = \frac{\lambda_l I_{\lambda_l} - \lambda_{l-1} I_{\lambda_{l-1}}}{\lambda_l - \lambda_{l-1}}. \quad (3.14)$$

With that, equation 3.11 becomes

$$\frac{dI_{\lambda_l}}{ds} + a_\lambda \frac{\lambda_l I_{\lambda_l} - \lambda_{l-1} I_{\lambda_{l-1}}}{\lambda_l - \lambda_{l-1}} = \eta_{\lambda_l} - (\chi_{\lambda_l} + 4a_\lambda) I_\lambda \quad (3.15)$$

defining the optical depth scale along a ray as

$$d\tau \equiv \chi + a_\lambda \left(4 + \frac{\lambda_l}{\lambda_l - \lambda_{l-1}} \right) \equiv \hat{\chi} ds \quad (3.16)$$

and introducing the source function, $S = \eta/\chi$, we can write

$$\frac{dI}{d\tau} = I - \frac{\chi}{\hat{\chi}} \left(S + \frac{a_\lambda}{\chi} \frac{\lambda_{l-1}}{\lambda_l - \lambda_{l-1}} I_{\lambda_{l-1}} \right) \equiv I - \hat{S}. \quad (3.17)$$

The formal solution of this equation can be obtained with equation 2.26 where $S = \hat{S}$. The construction of the Λ operator must be modified due to the additional terms that arise in the spherically symmetric radiative transfer equation (see Hauschildt, 1992*a*).

The Lagrangian formalism extends the standard boundary condition problem in radiative transfer by an initial value problem in wavelength due to equation 3.17. This problem is much more complex for arbitrary velocity fields where, depending on the direction of the velocity vector, a coupling to higher and lower wavelengths appear in the equations (see Baron & Hauschildt, 2004). In three spatial dimensions, this wavelength coupling can be the reason for huge computational costs in the Lagrangian formalism¹.

3.2 Eulerian formalism

The Eulerian formalism presented here is non-relativistic, which implies that the velocity of the moving atoms in the atmosphere has to fulfill the relation $v \ll c$. In the stationary frame of the observer the absorbers 'see' the photon at a Doppler shifted wavelength according to

$$\lambda_{\text{atom}} = \lambda_{\text{observer}} \cdot \left(1 + \frac{\vec{e}_{\text{char}} \cdot \vec{v}}{c} \right), \quad (3.18)$$

where \vec{e}_{char} is the unit vector of the characteristic, c the speed of light and \vec{v} the velocity of the absorbers. It is common to measure wavelength displacements from the line center in terms of Doppler widths, defining x as

$$x' = x + \mu V \quad (3.19)$$

¹depending on the exact implementation of the formalism

where $x = (\lambda - \lambda_0)/\Delta\lambda_D$ and x' defined similarly, with $\Delta\lambda_D$ the Doppler width given by $\Delta\lambda_D = \lambda_0 v_{th}/c$, $\mu = \cos(\alpha)$ the angle between the characteristic and the velocity vector of the atom and v_{th} the thermal velocity parameter,

$$v_{th} = \sqrt{\frac{2kT}{m} + \xi^2}. \quad (3.20)$$

Here, ξ accounts for the micro-turbulence, T is the temperature, k the Boltzmann constant and m the mass of the atom. To measure the velocity in the same units, we define $V = v_{atom}/v_{th}$.

The change of the photon wavelength in the continuum is negligible because the continuum terms do not vary much over the wavelength range implied by velocity shifts in the Eulerian frame ($v \ll c$), whereas the velocity field introduces angle-dependent opacity and emissivity in the lines which can change the opacities substantially. Depending on the direction of the photon, the line-emissivity and line-absorption become direction dependent in the Eulerian frame

$$\chi_l(\lambda_{atom}) \equiv \chi'_l(\lambda_{atom}, \mu, \phi), \quad \eta_l(\lambda_{atom}) \equiv \eta'_l(\lambda_{atom}, \mu, \phi), \quad (3.21)$$

where $\chi'_l = \chi(\lambda) \cdot \phi(\lambda, \mu, \phi)$ and $\eta'_l = \eta(\lambda) \cdot \phi(\lambda, \mu, \phi)$. $\phi(\lambda, \mu, \phi)$ is the normalized profile function given, for example, by a Gaussian

$$\phi(\lambda, \mu, \phi) = \frac{1}{\sqrt{\pi}\lambda_D} \exp\left[-\frac{(x + \mu V)^2}{\lambda_D^2}\right]. \quad (3.22)$$

The direction dependent opacities and emissivities are due to the direction dependent profile. This implicates a wavelength-angular coupling in the radiative transfer problem because the line profile also depends on the angular resolution of the radiation field.

This leads, first, to an angle-dependent line source function which has to be evaluated for every solid angle

$$S_l(\lambda) \equiv S_l(\lambda, \mu, \phi). \quad (3.23)$$

Equation 2.19 has to be rewritten in the Eulerian frame as

$$S_\lambda(\mu, \phi) = \frac{\kappa_\lambda(\mu, \phi)}{\sigma_\lambda(\mu, \phi) + \kappa_\lambda(\mu, \phi)} B_\lambda + \frac{\sigma_\lambda(\mu, \phi)}{\kappa_\lambda(\mu, \phi) + \sigma_\lambda(\mu, \phi)} J_\lambda \quad (3.24)$$

respectively

$$S(\lambda, \mu, \phi) = \epsilon_\lambda(\mu, \phi) B_\lambda + (1 - \epsilon_\lambda(\mu, \phi)) J_\lambda. \quad (3.25)$$

In general, B_λ is also direction dependent due to the wavelength shift in the Eulerian frame. As B_λ does not vary much over the wavelength range implied by velocity shifts ($v \ll c$), this is neglected.

And, second, to a modified operator splitting scheme to account for scattering. The thermalization parameter ϵ is direction dependent due to the anisotropic opacity and emissivity. We have to adjust the operator splitting scheme 2.36 to account for the angular coupling. Putting the solid angle dependence of the thermalization parameter $\epsilon(\mu, \phi)$ in equation 2.30, we define

$$\Lambda_\lambda^O = \int_0^{2\pi} \int_{-1}^{+1} \Lambda_{\lambda, \mu, \phi} \cdot (1 - \epsilon_\lambda(\mu, \phi)) d\mu d\phi, \quad (3.26)$$

$$J_\lambda = \Lambda_\lambda^O[S_\lambda]. \quad (3.27)$$

Using the elements from the Λ^O operator to construct the new $\Lambda^{O,*}$ operator, we can rewrite the iteration scheme, equation 2.36, as

$$J_\lambda^{\text{new}} = [1 - \Lambda_\lambda^{O,*}]^{-1} \{J_\lambda^{\text{FS}} - \Lambda_\lambda^{O,*} J_\lambda^{\text{old}}\}. \quad (3.28)$$

For complete redistribution, the mean intensity must be calculated with the direction dependent profile, equation 2.50 is then rewritten as

$$\bar{J} = \int_0^\infty \int_{-1}^1 \int_0^{2\pi} I_\lambda(\mu, \phi) \phi(\lambda, \mu, \phi) d\phi d\mu d\lambda, \quad (3.29)$$

and the $\bar{\Lambda}^{O,*}$ operator is constructed as

$$\bar{\Lambda}^{O,*} = \int_0^\infty \int_{-1}^1 \int_0^{2\pi} \Lambda_\lambda^{O,*} \phi(\lambda, \mu, \phi) d\phi d\mu d\lambda. \quad (3.30)$$

Complete redistribution is questionable in moving atmospheres because the non-uniform motion of the matter compromise the mechanism of trapping radiation which produces isotropic intensities in the line core. Rybicki (1970) gives an overview of the problems arising in moving atmospheres and concludes that complete redistribution can be assumed as long as $v \ll c$ in the Eulerian frame.

Chapter 4

The stellar atmosphere code PHOENIX

The basic theory of radiative transfer developed in chapter 2 and the treatment of moving atmospheres in the Lagrangian frame in section 3.1 is implemented in the stellar atmosphere code PHOENIX in one spatial dimension. The new 3DRT module in PHOENIX/3D allows the calculation of the radiation field in three spatial dimensions in cartesian, cylindrical and spherical coordinate systems.

This chapter gives an overview of the basic features of the PHOENIX code: Section 4.1 describes some main features apart from radiative transfer relevant to this work, in section 4.2 a short description of the solid angle integration in 3DRT is given followed by the construction of the Λ^* operator in three spatial dimensions in section 4.3. In section 4.4 the numerical behavior of the 3DRT code and geometrical effects arising in different coordinate systems are discussed.

4.1 What is PHOENIX in general?

PHOENIX is a general purpose stellar atmosphere code which can simulate stellar atmospheres and, therefore, the emergent spectrum of, e.g., main-sequence stars, stars with winds, novae, supernovae, brown dwarfs and extrasolar planets. The computer code PHOENIX can treat atmospheres in LTE and Non-LTE and can handle scattering. It has basically one main mode which allows the computation of model atmospheres of the before mentioned stars. Furthermore, it has the possibility to construct parameterized (toy) atmospheres with two-level atoms to test new algorithms. The radiation field in 3DRT is computed along characteristics.

The main flow-chart is shown in figure 4.1: The atmosphere structure is, in this example, obtained by hydrostatic equilibrium which sets the pressure and the density of the atmosphere on an initial temperature structure. The Equation of State (EOS) is solved to obtain the number densities of the atoms, ions and molecules. The absorption coefficient is calculated and the radiative transfer equations are iterated and solved for every desired wavelength point. In one spatial dimension there is the possibility to use the temperature correction routines to obtain a final temperature structure. In three spatial dimensions it would make more sense to use a three dimensional hydro-dynamical structure as input and compute the radiation field which, in turn, gives radiative feedback to the hydro-dynamical calculation. However, this approach is far beyond nowadays computer capacities.

Figure 4.2 shows the flow chart of the test framework in the 3DRT code. First, a parameterized (toy) atmosphere structure is constructed. Second, the line absorption

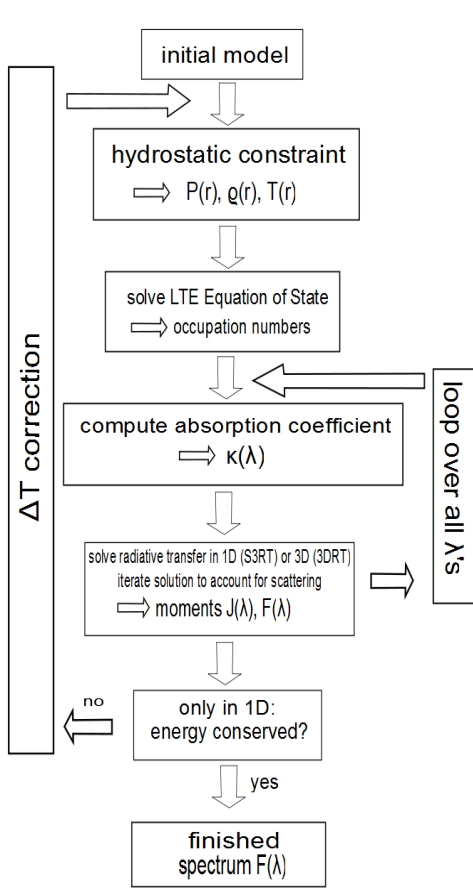


Figure 4.1: Flow chart of the main PHOENIX computer code

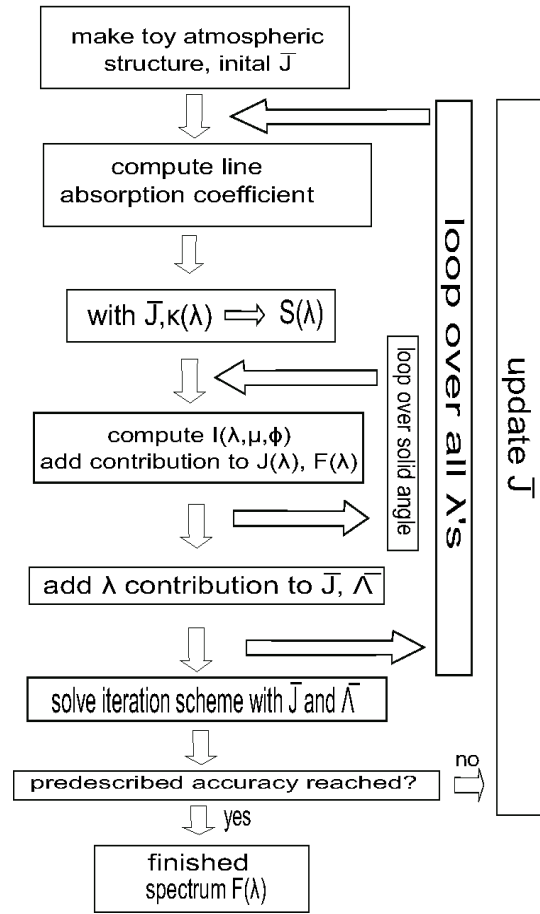


Figure 4.2: Flow chart of the 3DRT two-level atom setup

coefficient and then the source function is calculated and the radiative transfer is carried out as described in section 2.7.1. The iteration process is stopped if the prescribed accuracy of the radiative field is reached.

4.2 Solid angle integration in 3DRT

The integration of the moments of the radiation field and the Λ^* Operator is done by a 'pseudo' Monte Carlo integration where the accuracy increases with more solid angle points (Hauschildt & Baron, 2006; Baron & Hauschildt, 2007). 'Pseudo' means here that the solid angle points for the integration are not distributed arbitrarily over the integration interval but uniform. This will have some advantages in the cartesian coordinate system as we will see in section 4.4. For example, the mean intensity J_λ is calculated as

$$J_\lambda(\vec{r}) = \frac{1}{4\pi} \int_0^{2\pi} \int_{-1}^1 I_\lambda(\vec{r}, \mu, \phi) d\mu d\phi = \frac{1}{4\pi} \cdot \frac{4\pi}{N_{\text{solid angle}}} \left[\sum_{\theta, \phi} I(\theta, \phi) \right] \quad (4.1)$$

A more detailed explanation of the general Monte-Carlo integration method can be found, e.g., in Press et al. (1992).

4.3 The 3D Λ^* Operator

In one spatial dimension, the tridiagonal Λ^* operator in a specific layer is constructed with respect to the subsequent upper and lower layers. However, in three spatial dimensions a volume element is surrounded by $3^3 - 1 = 26$ volume elements which have to be considered in the construction of the operator. Therefore, the construction in three spatial dimensions follows Hauschildt (1992b) with consideration of all 26 surrounding volume elements (hereafter: voxel), the contribution to the Λ operator in a volume element j on a characteristic is given by

$$\Lambda_{i,j} = 0 \text{ for } i < j - 1 \quad (4.2)$$

$$\Lambda_{j-1,j} = \gamma_{j-1} \text{ for } i = j - 1 \quad (4.3)$$

$$\Lambda_{j,j} = \Lambda_{j-1,j} \exp(-\Delta\tau_{j-1}) + \beta_j^k \text{ for } i = j \quad (4.4)$$

$$\Lambda_{j+1,j} = \Lambda_{j,j} \exp(-\Delta\tau_j) + \alpha_{j+1} \text{ for } i = j + 1 \quad (4.5)$$

$$\Lambda_{i,j} = \Lambda_{i-1,j} \exp(-\Delta\tau_{i-1}) \text{ for } j + 1 < i, \quad (4.6)$$

where i labels the volume elements along the characteristic. These contributions have to be added in one specific voxel for every characteristic that passes through it and integrated over solid angle (Hauschildt & Baron, 2006; Baron & Hauschildt, 2007). For a nearest-neighbor approach equation 4.6 has to be stopped after $i = j + 1$. A larger operator needs more memory and does not warrant its use in terms of accelerating the iteration (Hauschildt & Baron, 2006).

4.4 Numerical and geometrical effects of 3DRT

3DRT requires substantial amounts of computing power to compute the emerging spectrum to a prescribed accuracy. This section summaries numerical effects of 3DRT to understand the different numerical behavior of the one and three spatial dimensional models in the next chapters. Furthermore, the properties of the 3DRT code in different coordinate systems are discussed. Basically three properties have a direct influence on the results:

1. Geometrical effects
2. The spatial resolution of the atmosphere
3. The angular resolution of the radiation field

Those effects are discussed in the following subsections. Furthermore, subsection 4.4.4 deals with a special property of cartesian coordinates with periodic boundary conditions¹.

The explanations of these three effects are carried out in cartesian coordinates with periodic boundary conditions (hereafter: PBCs) and in spherical coordinates. The numerical and geometrical effects in the cartesian grid without PBCs are the same as those with PBCs and the effects in the spherical grid corresponds to the effects in the cylindrical grid². Therefore, the focus of this discussion lies on the spherical and cartesian PBC

¹periodic boundary conditions means here: when a characteristic leaves a outermost (x, z) or (y, z) face in the cartesian grid, it is continued at the other side

²because the local coordinate systems in the volume elements of the cylindrical and spherical grid have different directions from one voxel to another whereas, in cartesian geometry, they are equal

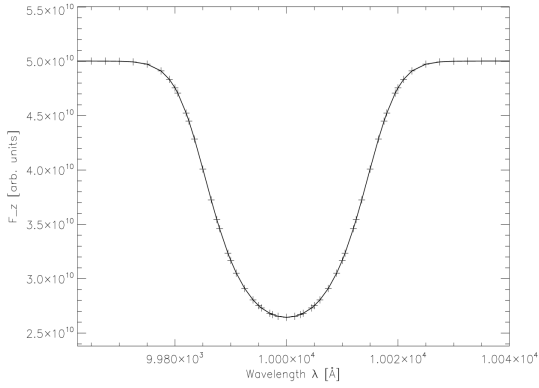


Figure 4.3: Spectrum from all outermost voxels in the cartesian grid with periodic boundary conditions

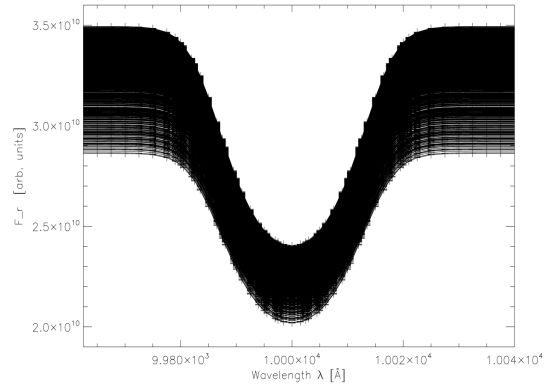


Figure 4.4: Spectrum from all outermost voxels in the spherical grid

geometry.

The examples shown in this section are obtained by using the parameterized (toy) atmosphere setup with two-level atoms with complete redistribution in 3DRT. The atmospheric structure depends only on r (or z in the cartesian examples) to show the numerical behavior more clearly. Generally, the atmospheric structure does not influence the effects explained here in any geometry.

4.4.1 Geometrical effects

3DRT is set up in three different three dimensional coordinate systems: Cartesian with and without periodic boundary conditions (PBCs), cylindrical and spherical. The characteristics in all geometries are tracked globally through the spatial grids which leads to a different behavior of the moments of the radiative field in different coordinate systems. The examples shown here explain the behavior of the flux in the outermost voxels in 3DRT as this quantity is compared to S3RT³ in chapter 5.

³S3RT is the one dimensional radiative transfer module

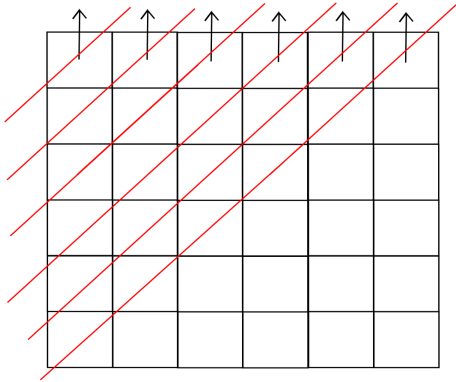


Figure 4.5: One $y = \text{const}$ plane in the 3D cartesian grid, the red lines show some characteristics through the grid under one constant solid angle

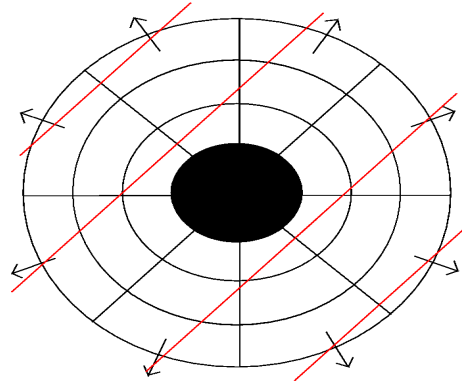


Figure 4.6: One $\phi = \text{const}$ plane in the 3D spherical grid, the red lines show some characteristics through the grid under one constant solid angle

In Figure 4.3 the spectrum of all outermost voxels in the cartesian grid with PBCs is plotted, the flux vectors in all voxels have the same value. In Figure 4.4 the spectrum in all outermost voxels in the spherical grid is plotted, the flux vectors in r direction differ from voxel to voxel. In both calculations the solid angle space was discretised by $n_{\theta,c} = n_{\phi,c} = 64$ angle points and the physical setup of the atmosphere is similar. It is obvious that the emergent flux in the cartesian grid is higher than in the spherical grid, as the surface in the spherical geometry increases with r^2 and therefore the energy density decreases as $1/r^2$ whereas, in the cartesian grid, the surface does not increase.

The reason for this different flux behavior is the global tracking of the characteristics throughout the grid. In cartesian coordinates, the coverage of the local solid angle space from voxel to voxel is similar as the angle of the characteristic to the flux vector is equal in each voxel, see Figure 4.5. In spherical coordinates, the local angle of the characteristic to the flux vector is different in each voxel, as seen in Figure 4.6. Therefore, the local solid angle space is covered differently from voxel to voxel which leads to different flux values in different voxels. The so called 'band-spectrum' shown in Figure 4.4 reduces in width when more solid angle points are used, the coverage of the local solid angle space adjusts to the others. Also, the number of volume elements used in the calculation reduces the width of the 'band-spectrum' as we shall see in the next subsection.

4.4.2 Spatial resolution

It is evident that, when more voxels are used, the better is the spatial resolution and, therefore, the resolution of the atmospheric properties.

Spherical coordinates

In Figure 4.7 the band spectrum of an atmosphere with three different spatial resolutions is shown. The solid angle discretization in all calculations is $n_{\theta,c} = n_{\phi,c} = 128$, whereas

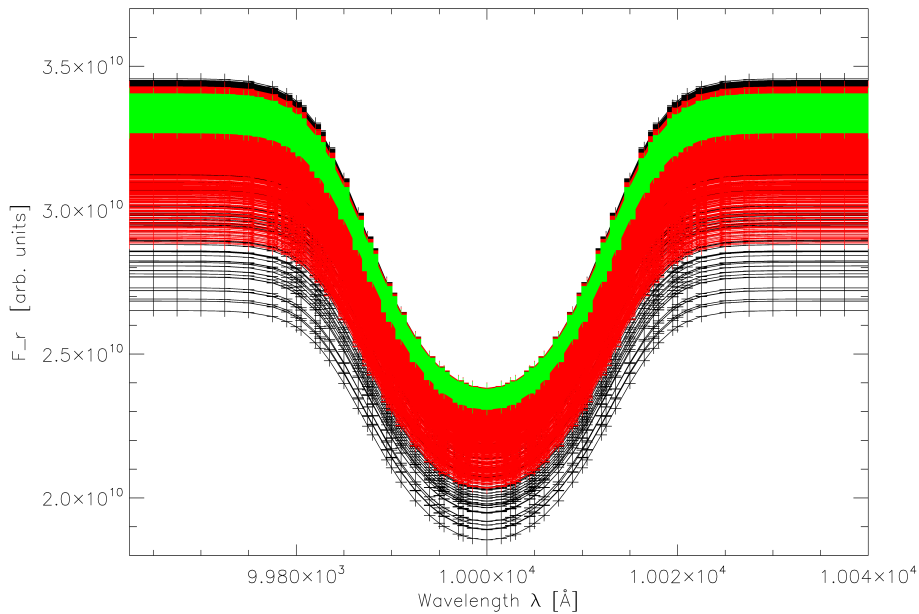


Figure 4.7: Band spectrum from all outermost voxels in a spherical atmosphere with different spatial resolutions: Black: $(n_r, n_\theta, n_\phi) = (31, 15, 31) = 14,415$, red: $(n_r, n_\theta, n_\phi) = (65, 31, 65) = 130,975$ and green $(n_r, n_\theta, n_\phi) = (131, 65, 131) = 1,115,465$ voxels. The solid angle discretization is $n_{\theta,c} = n_{\phi,c} = 128$.

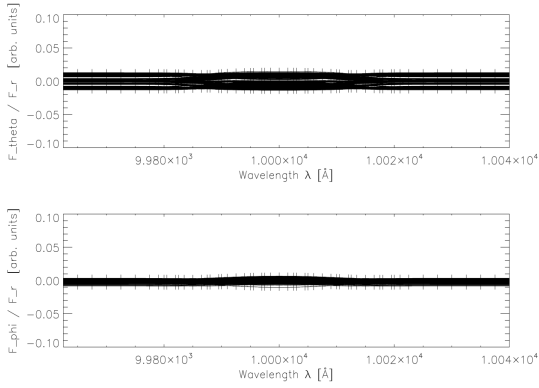


Figure 4.8: F_θ/F_r and F_ϕ/F_r in the spherical atmosphere with $(n_r, n_\theta, n_\phi) = (31, 15, 31)$ and $n_{\theta,c} = n_{\phi,c} = 128$ solid angle points

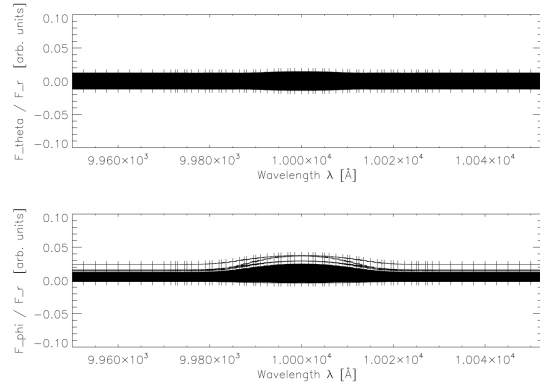


Figure 4.9: F_θ/F_r and F_ϕ/F_r in the spherical atmosphere with $(n_r, n_\theta, n_\phi) = (65, 31, 65)$ and $n_{\theta,c} = n_{\phi,c} = 128$ solid angle points

the black band-spectrum shows a calculation with $(n_r, n_\theta, n_\phi) = (31, 15, 31) = 14,415$ voxels, the red a calculation with $(n_r, n_\theta, n_\phi) = (65, 31, 65) = 130,975$ and the green band-spectrum shows as calculation with $(n_r, n_\theta, n_\phi) = (131, 65, 131) = 1,115,465$ voxels. The band-spectrum width reduces with a higher spatial resolution as the physical properties are mapped finer onto the three dimensional grid and the voxel size reduces.

As an error indicator of the solid angle integration of the radiation field (equation 4.1) the following is considered: In an atmosphere where the atmospheric properties only depend on the spatial coordinate r , the ratio F_θ/F_r and F_ϕ/F_r should be zero in a perfect computer model. In Figure 4.8 this ratio is plotted for the volume discretization of $(n_r, n_\theta, n_\phi) = (31, 15, 31)$, figure 4.9 shows the ratio in the $(n_r, n_\theta, n_\phi) = (65, 31, 65)$ discretised atmosphere.

The error in the solid angle integration does not decrease with the number of voxels used in the calculation as it just changes the mapping of the physical quantities onto the three dimensional grid. It does not change the angular resolution of the radiation field.

Cartesian coordinates with PBCs

In Figure 4.10 the spectra of atmospheres with a solid angle discretization of the radiation field of $n_{\theta,c} = n_{\phi,c} = 128$ solid angle points and different spatial resolutions in cartesian geometry is shown. The black spectrum shows a $(n_x, n_y, n_z) = (29, 29, 31) = 26,071$, the red a $(n_x, n_y, n_z) = (57, 57, 61) = 198,189$ and the green a $(n_x, n_y, n_z) = (127, 127, 131) = 2,112,899$ spatial discretised atmosphere. As in the spherical coordinate system, the mapping of the physical quantities onto the spatial grid is finer, the size of the voxels reduces. The more volume elements are used the more accurate the solution.

In Figure 4.11 and 4.12 the ratio F_x/F_z and F_y/F_z is shown for the atmospheres from figure 4.10 with $(n_x, n_y, n_z) = (29, 29, 31) = 26,071$ and $(n_x, n_y, n_z) = (127, 127, 131) = 2,112,899$ voxels. The ratio is negligible in the cartesian coordinate systems which is caused by the symmetry of the cartesian grid and the 'pseudo' Monte Carlo integration: For every direction of a characteristic in the cartesian grid there is exactly one characteristic with the opposite direction so that the errors cancel in the Monte Carlo integration. The ratio in the cartesian coordinate system is of the order $F_{x,y}/F_z = 10^{-6}$ and is caused by round-off errors.

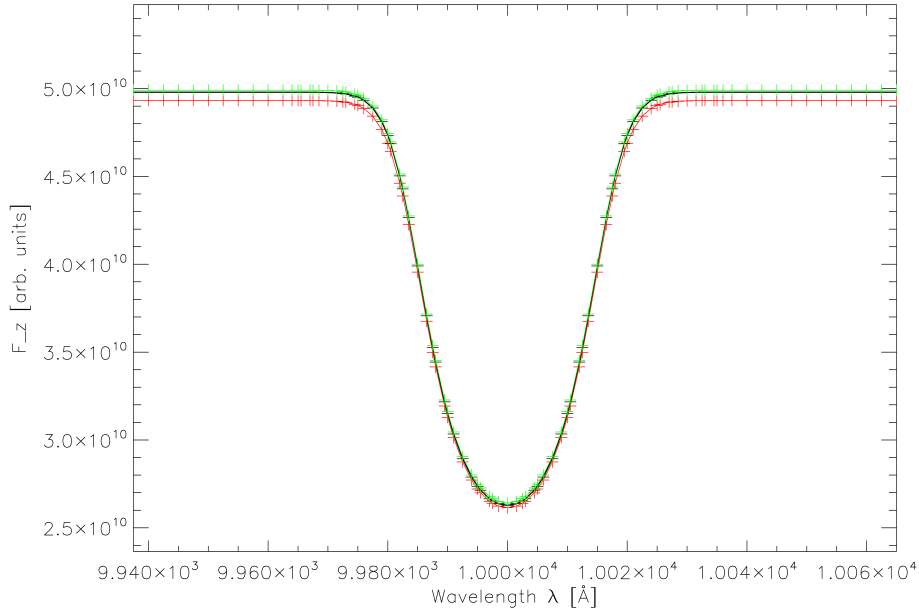


Figure 4.10: Spectra from a cartesian atmosphere with periodic boundary conditions and different kinds of spatial resolutions: Black: $(n_x, n_y, n_z) = (29, 29, 31) = 26, 071$, red: $(n_x, n_y, n_z) = (57, 57, 61) = 198, 198$ and green: $(n_x, n_y, n_z) = (127, 127, 131) = 2, 112, 899$. The solid angle discretization is $n_{\theta,c} = n_{\phi,c} = 128$.

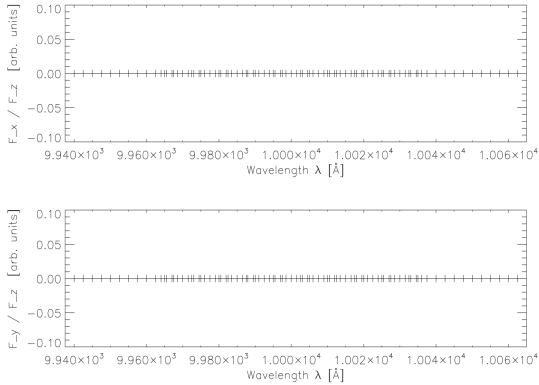


Figure 4.11: The ratio F_x/F_z and F_y/F_z in the cartesian grid with periodic boundary conditions and $(n_x, n_y, n_z) = (29, 29, 31) = 26, 071$ voxels and a $n_{\theta,c} = n_{\phi,c} = 128$ solid angle discretization.

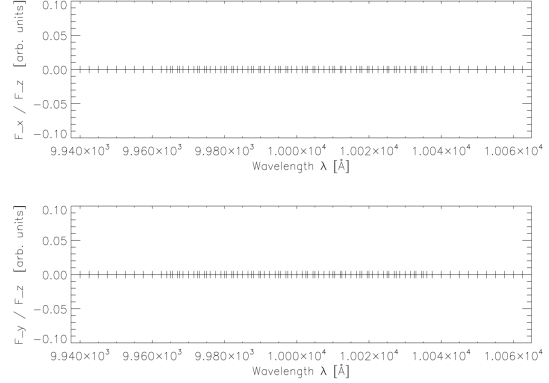


Figure 4.12: The ratio F_x/F_z and F_y/F_z in the cartesian grid with periodic boundary conditions and $(n_x, n_y, n_z) = (127, 127, 131) = 2, 112, 899$ voxels and a $n_{\theta,c} = n_{\phi,c} = 128$ solid angle discretization.

4.4.3 Angular resolution

The angular resolution controls the error in the Monte Carlo integration in equation 4.1. The more solid angle points are used the better the angular resolution of the radiation field and, therefore, the more accurate the solution of the integration over solid angle.

Spherical coordinates

In Figure 4.13 the band-spectrum of an atmospheric structure with the same spatial resolution $(n_r, n_{\theta}, n_{\phi}) = (65, 31, 65)$ but with different numbers of solid angle points is shown.

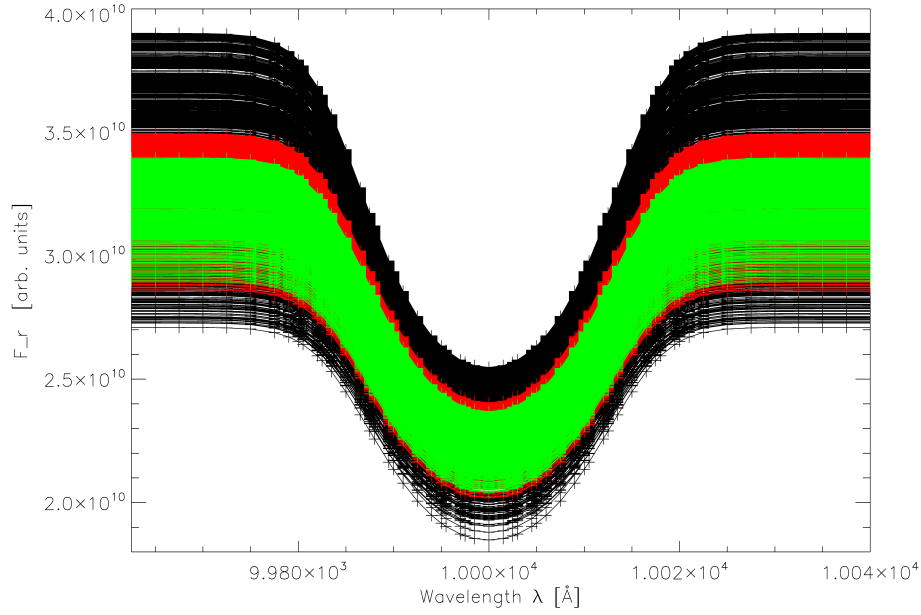


Figure 4.13: Band spectra from a spherical atmospheric setup with different kinds of solid angle discretization. Black: $n_{\theta,c} = n_{\phi,c} = 16$, red: $n_{\theta,c} = n_{\phi,c} = 64$ and green $n_{\theta,c} = n_{\phi,c} = 256$ solid angle points

The black band-spectrum shows a $n_{\theta,c} = n_{\phi,c} = 16$, the red $n_{\theta,c} = n_{\phi,c} = 64$ and the green band-spectrum $n_{\theta,c} = n_{\phi,c} = 256$ solid angle points. The number of solid angle points reduces the width of the band-spectrum due to the improved coverage of the local solid angle space from one voxel to the another voxels in spherical geometry. In addition, the radiation field is better resolved. Now, in Figure 4.14 and 4.15 the ratio F_{θ}/F_r and F_{ϕ}/F_r is decreasing with the number of solid angle points used in the calculation.

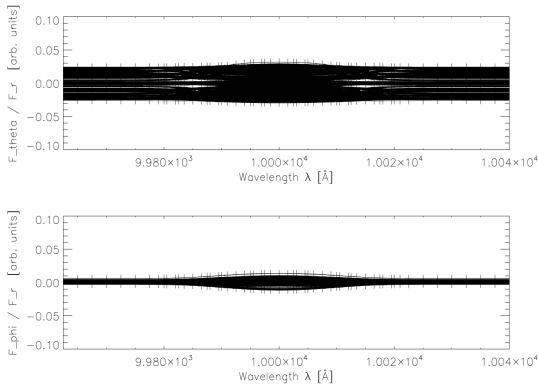


Figure 4.14: The ratio F_{θ}/F_r and F_{ϕ}/F_r in a spherical atmospheric setup with $(n_r, n_{\theta}, n_{\phi}) = (65, 31, 65)$ and $n_{\theta,c} = n_{\phi,c} = 64$ solid angle points

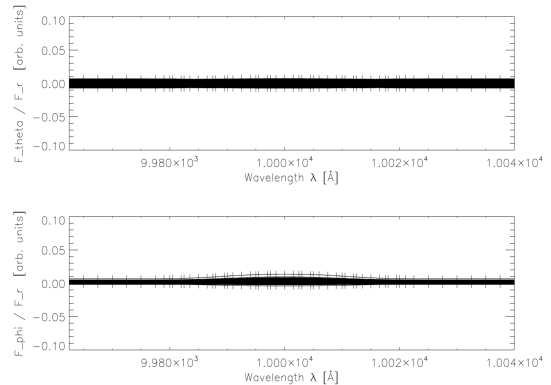


Figure 4.15: The ratio F_{θ}/F_r and F_{ϕ}/F_r in a spherical atmospheric setup with $(n_r, n_{\theta}, n_{\phi}) = (65, 31, 65)$ and $n_{\theta,c} = n_{\phi,c} = 256$ solid angle points

Cartesian coordinates with PBCs

Using more solid angle points in cartesian geometry leads also to a better representation of the radiation field. In figure 4.16 a cartesian atmosphere with the spatial extend $(n_x, n_y, n_z) = (29, 29, 31)$ and a solid angle resolution of the radiation field of: black $(n_{\theta,c}, n_{\phi,c}) = (32, 32)$, red: $(n_{\theta,c}, n_{\phi,c}) = (64, 64)$ and green $(n_{\theta,c}, n_{\phi,c}) = (256, 256)$ is shown.

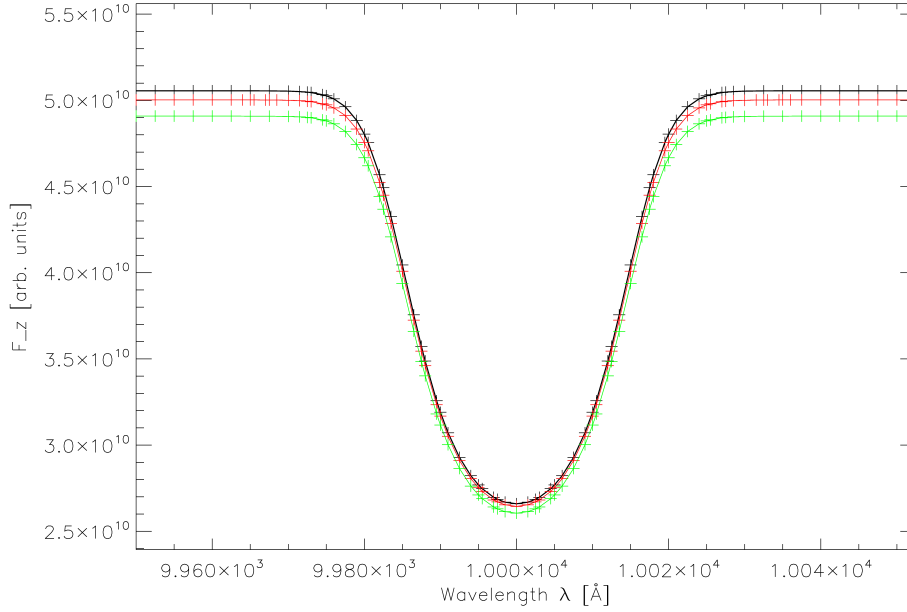


Figure 4.16: Spectra from all outermost voxels in the cartesian atmosphere with a spatial resolution of $(n_x, n_y, n_z) = (29, 29, 30) = 25.230$ voxels and a solid angle discretization of: Black: $n_{\theta,c} = n_{\phi,c} = 32$, red $n_{\theta,c} = n_{\phi,c} = 64$ and green $n_{\theta,c} = n_{\phi,c} = 256$ solid angle points.

Again, the ratio in $F_{x,y}/F_z$ (figure 4.17 and 4.18) is negligible as it cancels for the mentioned reasons in subsection 4.4.2.

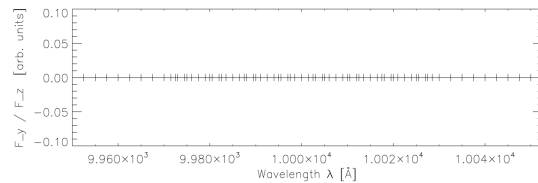
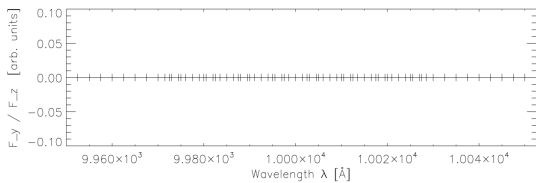
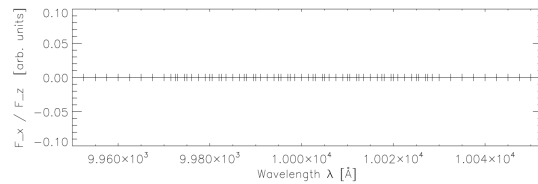
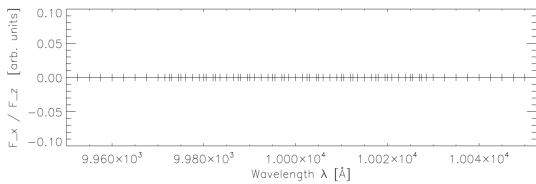


Figure 4.17: The ratio F_x/F_z and F_y/F_z in the cartesian grid with PBCs and $(n_x, n_y, n_z) = (29, 29, 31) = 26.071$ voxels and $n_{\theta} = n_{\phi} = 32$

Figure 4.18: The ratio F_x/F_z and F_y/F_z in the cartesian grid with PBCs and $(n_x, n_y, n_z) = (29, 29, 31) = 26.071$ voxels and $n_{\theta} = n_{\phi} = 256$

4.4.4 Cartesian coordinates with PBCs - Limiting the characteristics

In cartesian geometry with periodic boundary conditions there is another property which has direct influence on the formation of the spectral lines. Applying periodic boundary conditions on the spatial cartesian grid implies that characteristics which leave, for example, the $(-x, y - z)$ face are continued on the $(x, y - z)$ face until they reach the upper or lower boundary where they are terminated. To limit the computational cost of the calculation and to cut off grazing angles which would, for example, for a $\mu = 0$ characteristic to be continued forever, a limiting parameter is introduced, such that:

$$\text{steps per } z \text{ voxel} = \frac{\text{distance to upper and lower } z \text{ voxel}}{\mu \cdot s} \quad (4.7)$$

limits the times a characteristic is passing through a z voxel. s denotes the shortest path length to the next voxel in any (x, y, z) direction and $\mu = \cos(\theta)$ is the azimuthal angle of the characteristic.

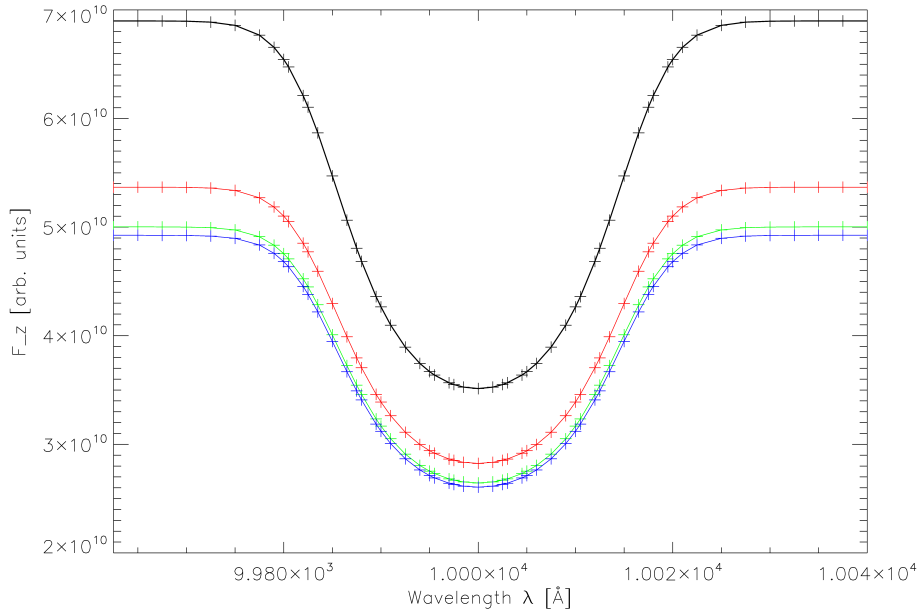


Figure 4.19: Spectrum of the cartesian code with PBCs and a varying limiting parameter to cut off characteristics with grazing angles. Black: 2, red: 6, green: 12 and blue: 16 steps per z voxel.

Figure 4.19 shows the influence of that limiting factor onto the spectrum as it cuts off characteristics with grazing angles. Using a low limitation factor cuts off to many characteristics which results in a poorly resolved radiation field. This causes the high flux for the 'two steps per z voxel' spectral line in figure 4.19. Using more than 16 steps per z voxel does not significantly change the flux in the spectral line anymore.

Chapter 5

The Eulerian frame versus the Lagrangian frame

This chapter deals with the comparison of the Lagrangian with the Eulerian formalism. To be able to compare both formalisms, a numerical framework has to be used to solve the radiative transfer equations in the corresponding framework. Therefore, the radiative transfer module **S3RT** is used in which the Lagrangian formalism has been implemented by Hauschildt (1992*a*) in one spatial dimension. To compare the results of the two approaches, a parameterized (toy) atmospheric setup is used. The atmospheric structures obtained do not claim to be realistic atmospheres, but they allow the comparison of the two approaches besides any other effects that may arise in more complex atmospheric structures.

Section 5.1 describes the consistency tests that check the construction of the scattering operator $\Lambda^{O,*}$ in the Eulerian frame. Section 5.2 outlines the construction of the test atmosphere used for the comparison. Section 5.3 shows the comparison between the one dimensional Lagrangian and the three dimensional Eulerian formalism. The limitations of the Eulerian formalism are presented in section 5.4.

5.1 Consistency tests of the Eulerian formalism

In order to handle scattering in the atmosphere, a modified scattering operator ($\Lambda^{O,*}$) has to be constructed for the Eulerian frame to account for the anisotropic line profiles and thermalization parameters as described in section 3.2. In general, the nearest neighbor Λ operator in three spatial dimensions can be considered as a spatial 'cube' with 27 entries. To account for scattering this 'cube' has to be constructed in every voxel in the atmosphere to propagate the effect of scattering throughout the atmosphere. The construction itself can be tested with the help of the formal solution and the source function and must be verified for each solid angle. The procedure in three spatial dimensions is as follows:

- Set the source function to zero except in one test voxel in the whole spatial three dimensional atmosphere. The source function in the test voxel is set to one and is called a pulse.
 - Perform a formal solution under a specific solid angle
 - Check if the Λ 'cube' with its 27 entries equals the intensities in the corresponding voxels. The central entry of the Λ matrix corresponds to the voxel where the operator is constructed, the surrounding entries correspond to the surrounding voxels. Check if all entries of the Λ operator equal the intensities in the corresponding voxels.
-

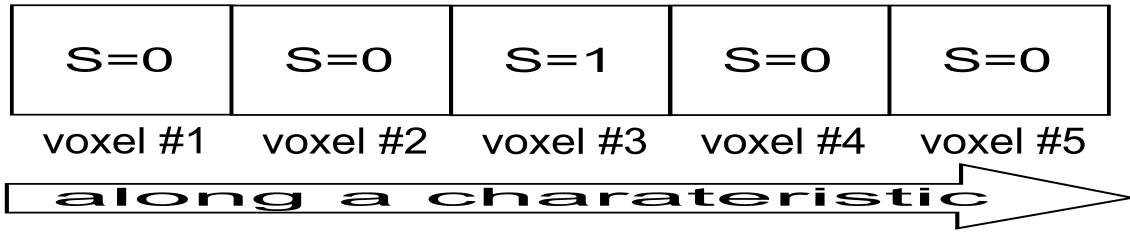


Figure 5.1: Schematic diagram of the Λ construction test in, for simplicity, cartesian geometry

- Do this for every desired solid angle
- Check the integrals over solid angle

For example, in figure 5.1 the voxels along a characteristic for a specific solid angle and the corresponding source functions are shown. The Λ operator and its entries are constructed, for example, in test voxel #3. For the formal solution (equation 2.26) we find the intensities in the voxels to be:

$$\begin{aligned}
 \text{voxel \#1 :} & \quad I_1 = 0 \\
 \text{voxel \#2 :} & \quad I_2 = \gamma_2 \\
 \text{voxel \#3 :} & \quad I_3 = I_2 \cdot \exp(-\Delta\tau_2) + \beta_3 \\
 \text{voxel \#4 :} & \quad I_4 = I_3 \cdot \exp(-\Delta\tau_3) + \alpha_4 \\
 \text{voxel \#5 :} & \quad I_5 = I_4 \cdot \exp(-\Delta\tau_4) \\
 \text{voxel } > \text{\#5 :} & \quad I_i = I_{i-1} \cdot \exp(-\Delta\tau_{i-1}).
 \end{aligned}$$

The entries in the operator, equations 4.3 to 4.5, here $j = 3$, must equal the intensities in the corresponding voxels to ensure the consistency. In the Eulerian frame, the opacity (equation 3.21), therefore, the optical depth τ and thus the parameters α, β, γ are solid angle dependent. The testing scheme above reveals any errors in the Λ^O construction.

For two-level atoms an additional test has to be made: The iteration scheme has to be carried out over the wavelength integrated quantities \bar{J} and $\bar{\Lambda}$. In the Eulerian frame, the angle dependent profile (equation 3.22) has to be multiplied for every solid angle to the mean intensity and the Λ operator (equations 3.29 and 3.30). In the testing scheme above, \bar{J} in the voxels have to be compared to the entries of the $\bar{\Lambda}^{O,*}$ operator to verify the correct construction of the operator.

5.2 The testing environment

The Lagrangian formalism in one spatial dimension was developed for supernova applications in spherical geometry. Therefore, the spatial structure of the testing environment is in spherical geometry in both approaches. The comparison of both approaches is a verification for the Eulerian formalism, as the Lagrangian method is well tested over the last 20 years.

The test atmosphere is assumed to consist only of hypothetic two-level atoms with complete redistribution (see section 2.7.1 and 2.5.1). The ratio $\chi_{\text{line}}/\chi_{\text{continuum}}$ is set to 10^4 to simulate a strong line. The background continuum and the thermal sources are

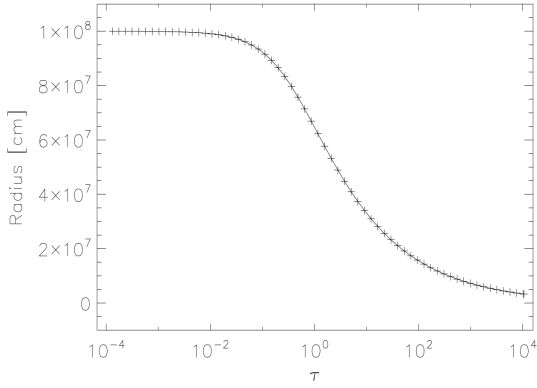


Figure 5.2: The radius is plotted over the optical depth in the continuum.

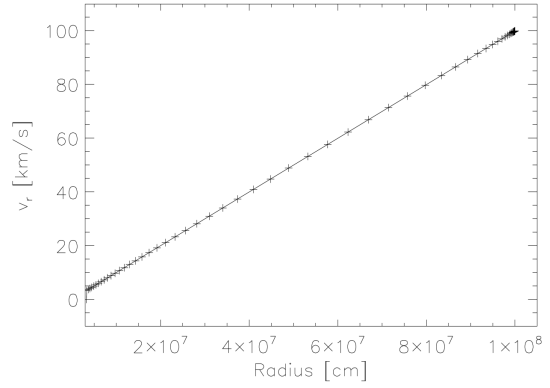


Figure 5.3: The velocity is plotted over the radius with $v_{\max} = 1 \cdot 10^2 \text{ km s}^{-1}$

constant over wavelength. Therefore, only one line over an otherwise flat continuum is seen. The continuum opacity is parameterized by a power law,

$$\chi_i = \chi_0 \left(\frac{r_{\max}}{r_i} \right)^n, \quad (5.1)$$

where i labels the atmospheric layers in one spatial dimension and r is the radius. The parameter n and the radius were chosen so that the diffusion approximation can be applied at the inner boundary and that the atmosphere ranges from optically thick to optically thin regions. With this setup, the continuum optical depth scale in the test atmosphere ranges from $\tau_{\max} = 10^4$ to $\tau_{\min} = 10^{-4}$ and the radius of the sphere from $r_{\min} = 3.3 \cdot 10^6$ cm to $r_{\max} = 1 \cdot 10^8$ cm and has a total extend of 976 km (see figure 5.2).

The (grey) temperature structure in the atmospheric layers is obtained with the help of the Hopf function. Setting the effective temperature T_{eff} (in the test atmospheres $T_{\text{eff}} = 10^4$ K), the τ dependent temperature is given by

$$T^4(\tau) = T_{\text{eff}}^4 \cdot \frac{3}{4}(\tau + q(\tau)), \quad (5.2)$$

where $q(\tau)$ is the Hopf function. With the analytic approximation of the Hopf function by Labs (1950), the temperature structure is given by

$$T_i^4 = T_{\text{eff}}^4 \cdot \frac{3}{4}(\tau_i + 0.7104 - 0.1331 \exp(-3.4488\tau_i)). \quad (5.3)$$

In the Eulerian formalism, the velocity field can be arbitrary at every atmospheric layer but, for the Lagrangian formalism, it is important that the atmospheric layers are moving monotonically as the wavelength derivative is discretised by a stable upwind scheme (equation 3.17). Therefore, the velocity field in the testing atmosphere is monotonically increasing as

$$v_i = \frac{v_{\max}}{r_{\max}} \cdot r_i, \quad (5.4)$$

where v_{\max} is the maximal velocity in the outer layer. Figure 5.3 shows the velocity depending on the radius in an atmosphere with $v_{\max} = 1 \cdot 10^2 \text{ km s}^{-1}$. Throughout the tests that have been done in this chapter, the maximum velocity v_{\max} was varied in the atmosphere and the two resulting spectra have been compared in the frame of the observer. The other atmospheric quantities have been kept constant.

The atmospheric structure, constructed in one spatial dimension, is interpolated onto the three dimensional sphere and, therefore, the three dimensional atmospheric properties are independent of the spatial polar and azimuthal angle. The number of radial layers in one and three spatial dimensions are similar.

In general, the two formalisms are independent of the atmospheric structures, besides the restriction to monotonic velocity fields in the Lagrangian frame and the restriction to non relativistic moving atmospheres in the Eulerian frame as we shall see in section 5.4. Therefore, the two approaches can have been compared in any test atmospheres which fulfill these requirements.

5.3 Results

This section summaries the results of the comparison of the two formalisms. In real world applications with more spectral lines, the Eulerian formalism is suitable in atmospheres where the velocity field corresponds to, at most, a few Doppler widths. Because the coverage of the line profile depends on the magnitude of the velocity field and the width of the line. The problems arising in applications with high velocity fields, high velocity field gradients or small Doppler widths are discussed in section 5.4. In this section, velocity fields up to $1 \cdot 10^3 \text{ km s}^{-1}$ were used to stress-test the algorithm with a broad spectral line. Before the comparison was done, the $\Lambda^{O,*}$ operator passed the consistency test successfully.

The spectral line was assumed to be Gaussian, so that the profile of the line is written as

$$\phi(\lambda) = \frac{1}{\sqrt{\pi}\omega_{\text{line}}} \exp \left[-\frac{(\lambda - \lambda_0)^2}{\omega_{\text{line}}^2} \right], \quad (5.5)$$

where λ_0 is the central wavelength and $\omega_{\text{line}} = \lambda_D$ the width of the Gaussian. The central wavelength is at $5 \cdot 10^4 \text{ \AA}$ and, therefore, the width of the line corresponds to a thermal velocity of 60 km s^{-1} . All spectral lines have a line thermal parameter of $\epsilon_l = 10^{-2}$.

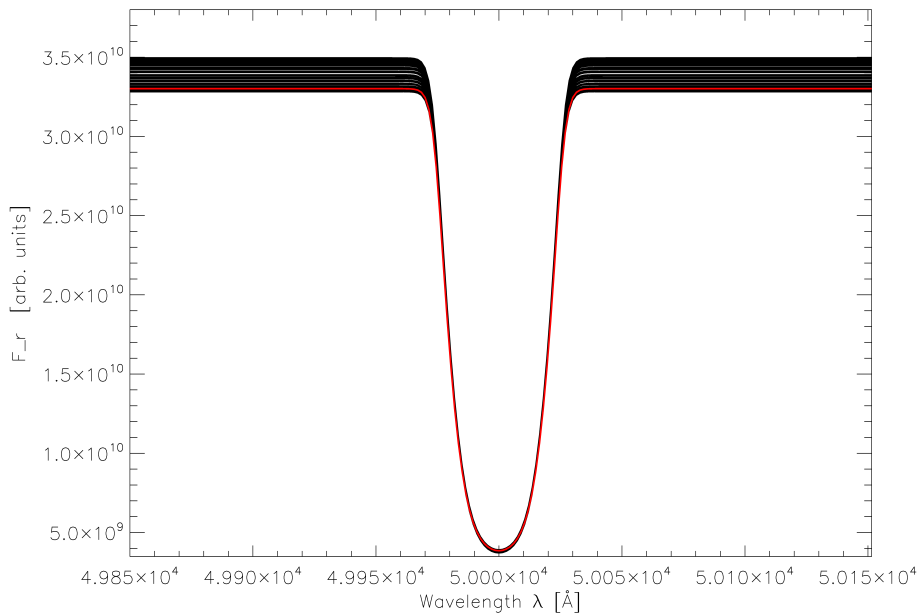


Figure 5.4: Comparison of the 1D Lagrangian (red) and the 3D Eulerian (black) formalism in a static atmosphere.

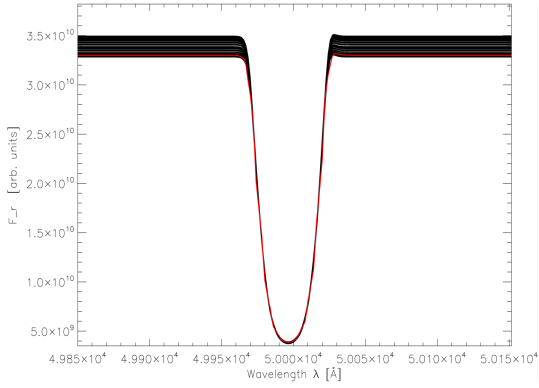


Figure 5.5: Comparison of the 1D Lagrangian and the 3D Eulerian formalism with a velocity field with $v_{\max} = 30 \text{ km s}^{-1}$. The magnitude of the velocity field corresponds to half a Doppler width of the spectral line.

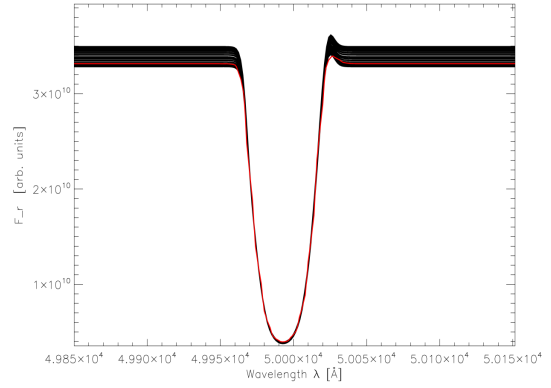


Figure 5.6: Comparison of the 1D Lagrangian and the 3D Eulerian formalism with a velocity field with $v_{\max} = 60 \text{ km s}^{-1}$. The magnitude of the velocity field corresponds to one Doppler width of the spectral line.

As a first test, the Eulerian formalism was applied to a static atmospheric structure, the corresponding spectrum is shown in figure 5.4. The agreement between the one dimensional and the three dimensional Eulerian solution is, under consideration of the numerical effects discussed in section 4.4, excellent. A detailed comparison shows that the angle dependent opacity and the $\Lambda^{O,*}$ operator is calculated correctly within the Eulerian formalism.

Figure 5.5 shows the emergent spectrum with $v_{\max} = 30 \text{ km s}^{-1}$ which corresponds to half the intrinsic Doppler width of the spectral line. Figure 5.6 shows the result for $v_{\max} = 60 \text{ km s}^{-1}$ in the atmosphere. The typical emission feature in expanding atmos-

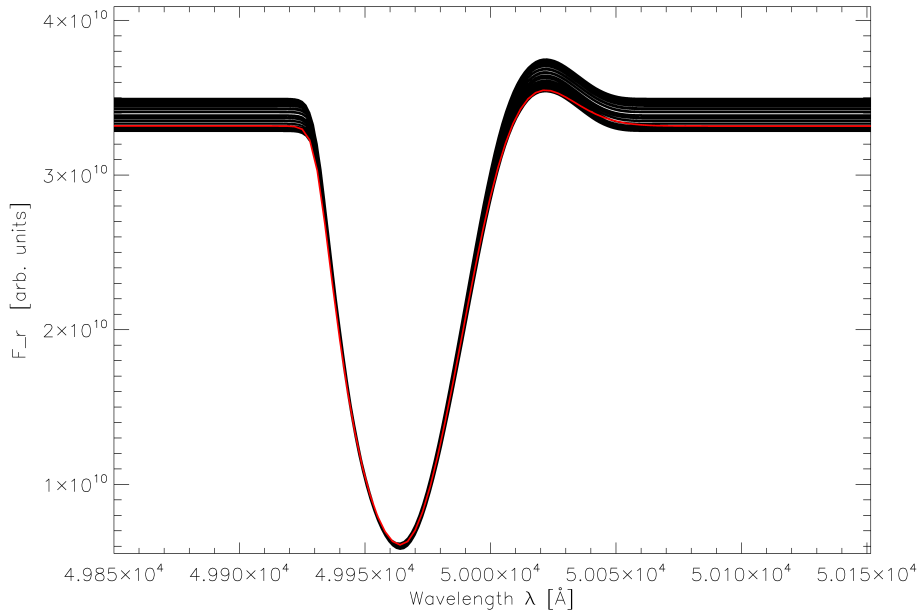


Figure 5.7: Comparison of the 1D Lagrangian and the 3D Eulerian formalism with a velocity field with $v_{\max} = 300 \text{ km s}^{-1}$. The magnitude of the velocity field corresponds to five Doppler widths of the spectral line.

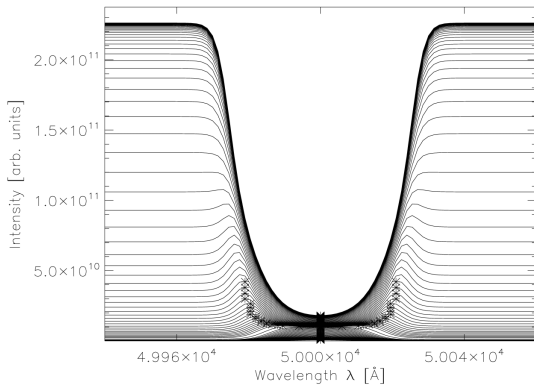


Figure 5.8: The intensity for characteristics with $-1 \leq \mu \leq 1$ in a, for simplicity, one dimensional static atmosphere. The intensity is shown in the second layer from the top. The crosses mark the maximum of the intensity.

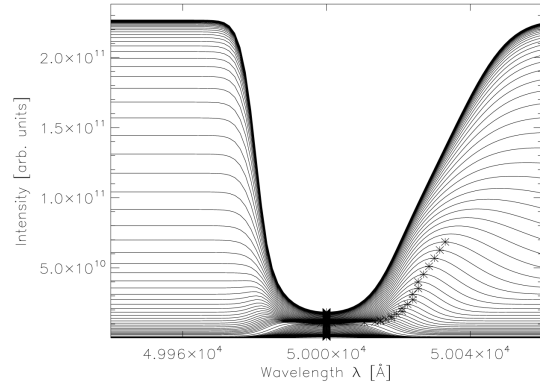


Figure 5.9: The intensity for characteristics with $-1 \leq \mu \leq 1$ in a one dimensional atmosphere for simplicity in the second layer from the top. The atmosphere has as velocity field with $v_{\max} = 300 \text{ km s}^{-1}$. The crosses mark the maximum of the intensity.

pheres at the rest wavelength of the line is already visible, the agreement between the two formalism is excellent. This feature increases with the magnitude of the velocity field in the atmosphere, see figure 5.7. The blue shifted absorption emerges from the part of the atmosphere which is moving towards the observer, the emission feature at the rest wavelength emerges from the 'edges' of the atmosphere perpendicular to the observer. In static atmospheres, the emission and absorption occur at the same wavelength, therefore, in the here presented static atmosphere with optical thin outer layers no emission feature is seen¹. In expanding atmospheres, the absorption and emission takes place at different wavelengths, due to different angles of the velocity field to the characteristics (or: line of sight to the observer) in different layers. In figure 5.8 the intensity is plotted against the wavelength for all characteristics in, for simplicity, in a one dimensional atmosphere in

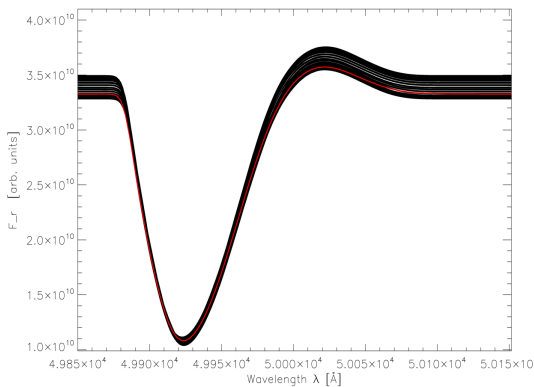


Figure 5.10: Comparison of the 1D Lagrangian and the 3D Eulerian formalism with a velocity field with $v_{\max} = 600 \text{ km s}^{-1}$. The magnitude of the velocity field corresponds to ten Doppler widths of the spectral line.

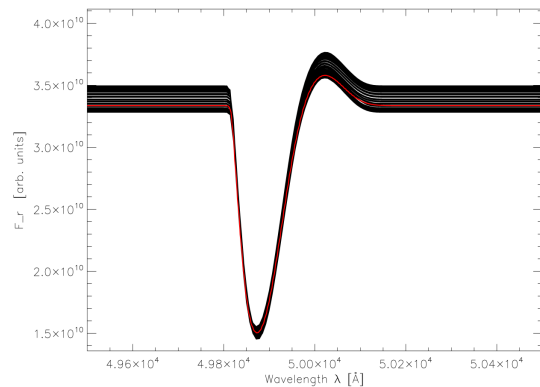


Figure 5.11: Comparison of the 1D Lagrangian and the 3D Eulerian formalism with a velocity field with $v_{\max} = 1.000 \text{ km s}^{-1}$. The magnitude of the velocity field corresponds roughly to 18 Doppler widths of the spectral line.

¹In general, those emission features can be seen

the second layer from the top. In the static, here presented, atmosphere the emission feature vanishes. In expanding atmospheres, the emission feature gets Doppler-shifted and, therefore, contribute to other wavelength points. Figure 5.9 shows the intensity against the wavelength for all characteristics in spatial one dimension in a moving atmosphere with $v_{\max} = 300 \text{ km s}^{-1}$. The displacement of the emission peak is clearly visible in comparison to figure 5.8².

For completeness, figures 5.10 and 5.11 show the comparisons of the Lagrangian and Eulerian formalism for $v_{\max} = 600 \text{ km s}^{-1}$ and $v_{\max} = 1.000 \text{ km s}^{-1}$ which corresponds to ten respectively 18 Doppler widths of the spectral line. The agreement is very good.

This section shows that the results obtained with the Eulerian formalism is in excellent agreement with the results from the well-tested Lagrangian formalism. The comparison covered atmospheric velocities from $0 - 1.000 \text{ km s}^{-1}$ with monotonically increasing velocities due to the limitation in the Lagrangian formalism. With the consistency test in section 5.1 and the results in this section, the Eulerian formalism is shown to work correctly.

5.4 Limitations of the Eulerian formalism

The section summaries the limitations of the Eulerian formalism. In subsection 5.4.1 the problem with small Doppler widths and high velocity fields are discussed, where 'high' still means $v \ll c$. Subsection 5.4.2 outlines relativistic effects which are not implemented in the Eulerian formalism.

5.4.1 Covering the profile

The angle dependent profile of the line (equation 3.22) must be resolved in the solid angle space and the wavelength discretization must be fine enough so that the profile of the line can be covered sufficiently. The wavelength discretization has to be finer than the maximum Doppler shift at a specific specific wavelength point,

$$\Delta\lambda_{\max \text{ doppler}} > \Delta\lambda_{\text{discretization}}, \quad (5.6)$$

to ensure that the intrinsic profile of the line can be covered by the Doppler shifted wavelength point. The coverage itself depends on the number of solid angle points. Figure 5.12 shows the resulting spectra in one volume element of a poor solid angle discretised calculation. If not enough solid angle points are used, the resulting spectrum has a 'wiggly' shape due to the poor coverage of the profile of the line: Some characteristics 'see' the line and some do not. In static and Lagrangian line transfer problems it is necessary that the line is covered by the discretised wavelength grid used in the calculation, as the profile does only depend on the wavelength $\phi \equiv \phi(\lambda)$. In the Eulerian moving atmosphere the profile depends on the wavelength-angle coupling of equation 3.22 and, therefore, also on the solid angle discretization.

In Figure 5.13, the profile in the (Eulerian moving) *line center* is plotted: The plus signs show the profile in the static case. As it is not solid angle dependent it is unity everywhere. The triangles show the anisotropic profile of a poor solid angle discretization and the rectangles of a medium quality solid angle discretization in the moving atmosphere in the Eulerian frame: The profile in the line center is not hit at all, this causes a wiggly or even no spectral line. The asterisks show a good quality solid angle discretization, the

²The intensity in the moving atmosphere is shown in the co-moving frame.

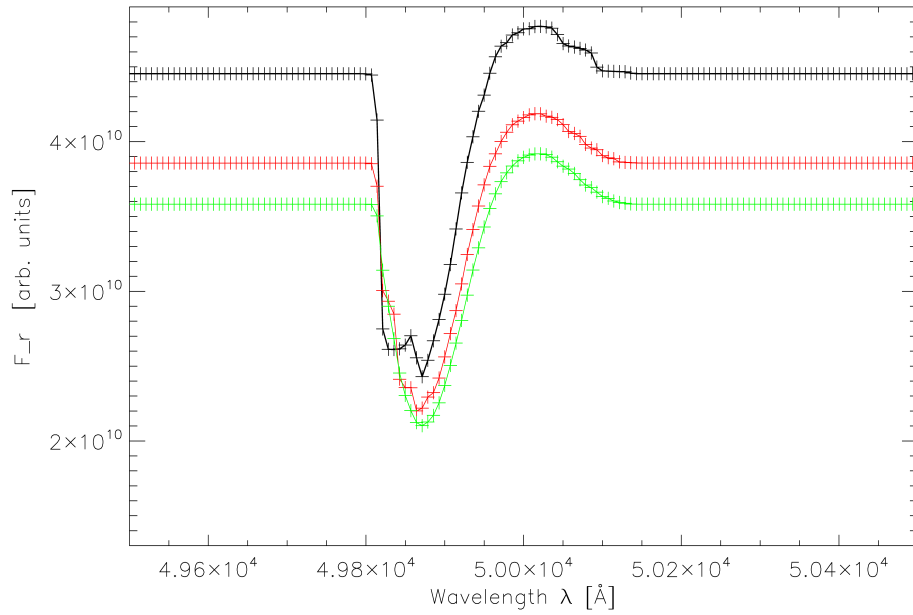


Figure 5.12: Resulting wiggly spectra with a poor solid angle discretization in one outermost voxel in a spherical geometry with a monotone increasing velocity field with $v_{\max} = 1 \cdot 10^3 \text{ km s}^{-1}$ in the Eulerian frame. Black: 64, red: 256 and green: 1024 solid angle points (the difference in the continuum flux is explained in section 4.4).

anisotropic profile in the Eulerian moving atmosphere hits the line center and the profile is well covered.

This effect is driven by the velocity field and the Doppler width of the spectral lines

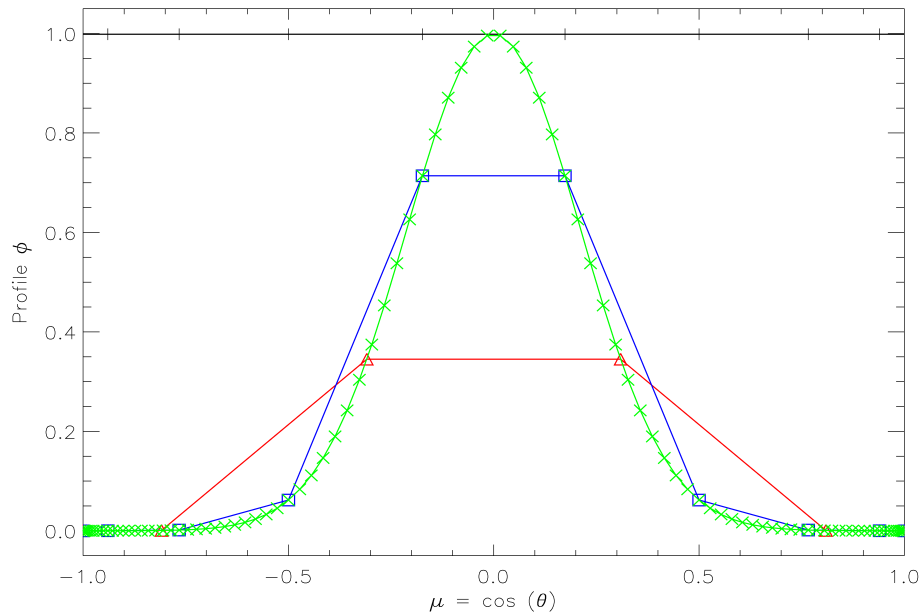


Figure 5.13: Plot to illustrate the problem of resolving the profile of a line. The line with the triangles/rectangles shows a poor/medium and the line with the asterisk show a good solid angle discretization in the Eulerian moving atmosphere.

in the atmosphere: The smaller the Doppler width or the higher the velocity field the more solid angle points are necessary to cover the line profile. It is not possible to pose a quantitative constraint on the solid angle discretization as, for a perfect coverage of the line profile, an infinite amount of solid angle points would have to be used. In real world applications with many spectral lines, the number of solid angle points should be increased until the differences in the spectral lines of different solid angle discretized calculations vanishes. The gradient of the velocity field between two volume elements is also important: If the gradient is too large, the line vanishes from one voxel to the another on a characteristic. This can be avoided by using more volume elements.

5.4.2 Relativistic effects

The formulation of the Eulerian method in the observers frame in this work is non-relativistic as only the Doppler shift of the photon is taken into account but no additional terms of higher order in (v/c) are included. As a consequence, the Eulerian frame formulation has to show differences in comparison to the Lagrangian formalism when those higher order terms start to influence the solution.

In figure 5.14, the spectrum in spherical geometry for different atmospheric velocities is shown for the Lagrangian frame formalism. When the velocity of the atmosphere is about 1% of the speed of light, the continuum increases due to the fact that the photons are less interacting with the stellar material which is caused by the Lorentz boost. From equation 3.3 we find that

$$\chi_0 = \frac{\chi}{\gamma(1 - \beta\mu)} \xrightarrow{v \rightarrow c} 0. \quad (5.7)$$

The Lorentz boost decrease the opacity seen by the photons in the co-moving frame, as v gets closer to c this effect increases. In Figure 5.15 the spectrum in a spherical atmosphere for the same atmospheric velocities as in the co-moving frame is shown in the Eulerian frame. As relativistic effects are neglected in this approach, no increase in the flux is seen.

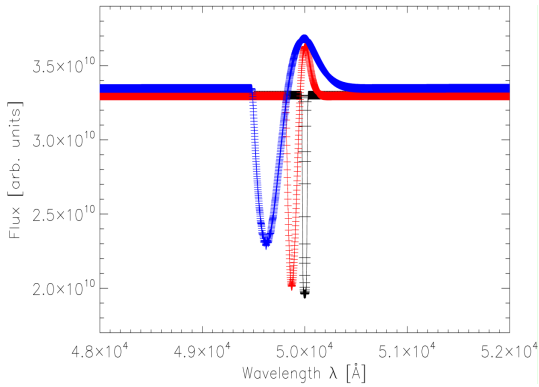


Figure 5.14: Relativistic effects in the 1D Lagrangian formalism. Black: $v_{\max} = 0 \text{ km s}^{-1}$, red: $v_{\max} = 1 \cdot 10^3 \text{ km s}^{-1}$ and blue: $v_{\max} = 3 \cdot 10^3 \text{ km s}^{-1} \approx 1 \% c$

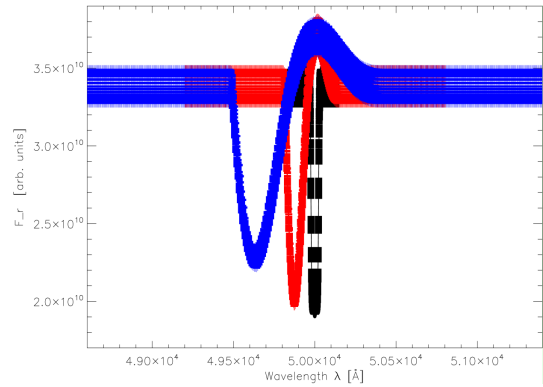


Figure 5.15: No relativistic effects in the 3D Eulerian frame formalism. Black: $v_{\max} = 0 \text{ km s}^{-1}$, red: $v_{\max} = 1 \cdot 10^3 \text{ km s}^{-1}$ and blue: $v_{\max} = 3 \cdot 10^3 \text{ km s}^{-1} \approx 1 \% c$

In general, it is possible to include higher terms of the order (v/c) in the Eulerian approach. But, as the Eulerian frame method in this work was designed to be used in calculations of convection and global circulation models in which the magnitude of the velocity field is always $v_{\max} \ll c$, it was not necessary to do so.

Chapter 6

3D Eulerian versus 1D Lagrangian with atoms in LTE

Section 5.3 showed that the comparison of the spatial three dimensional Eulerian frame formalism to the one dimensional Lagrangian formalism was, with respect to the numerical and geometrical effects, excellent. In section 5.4 the limitations of the Eulerian formalism were explained, it was outlined that the Eulerian frame formalism should only be used in atmospheres where the maximal velocity corresponds to a few Doppler widths of the spectral line with the smallest Doppler width. In this section, the Eulerian frame formalism is applied to atmospheres with atoms in local thermodynamic equilibrium with small monotonic velocity fields and compared to the Lagrangian frame formalism. This section is a proof of concept for the Eulerian formalism in 'real world' applications. The comparison between the two frameworks in this chapter has been performed with the PHOENIX code.

Section 6.1 summaries the specific atmospheric properties in which the comparison was performed. Section 6.1.1 explains the shapes of line profiles in stellar atmosphere and, finally, section 6.2 shows the results of the comparison of the two formalism for Gaussian and Voigt shaped line profiles of atoms and molecules.

6.1 The Atmosphere

A short description of the general setup of the PHOENIX code is given in section 4.1. This chapter describes the main PHOENIX setup, how to construct an atmosphere and to obtain the relevant atmospheric properties. The geometry of the model atmosphere in the Lagrangian and the Eulerian formulation is chosen to be spherical, as the Lagrangian formalism is developed for this geometry. The atmospheric structure is obtained by applying the hydrostatic equilibrium, the pressure must therefore follow

$$\nabla P(r) = -\rho(r)g, \quad (6.1)$$

where P is the total pressure, r the radius, ρ the density and g is the gravitational acceleration which follows

$$g(r) = \frac{GM(r)}{r^2}. \quad (6.2)$$

Here, $M(r)$ is the mass of the star inside r and G the gravitational constant. The atmosphere is assumed to be in thermal equilibrium, therefore, the gradient of the luminosity must be zero:

$$\nabla L = 0. \quad (6.3)$$

With the constant luminosity, a formal effective temperature can be associated with the atmosphere by

$$4\pi r^2 \sigma T_{\text{eff}}^4 = L, \quad (6.4)$$

where σ is the Stefan-Boltzmann constant. The parameters T_{eff} and $\log(g)$ can be used to construct the model atmosphere. In this chapter, the model atmospheres have the values $T_{\text{eff}} = 5000 \text{ K}$ and $\log(g) = 4$ which corresponds roughly to a late G-type star. Furthermore, solar abundances are assumed. The velocity field is monotonically increasing because of the restriction in the Lagrangian approach, described in the last chapter. The velocity field follows

$$v_i = \frac{v_{\text{max}}}{r_{\text{max}} - r_{\text{min}}} \cdot (r_i - r_{\text{min}}), \quad (6.5)$$

where i labels the atmospheric layers. The atmosphere is constructed in one spatial dimension and is interpolated onto the three dimensional grid in spherical coordinates. The atmospheric properties are, therefore, independent of the spatial azimuthal and polar angle in the three dimensional grid, the discretization in r is similar in both setups.

6.1.1 Shapes of spectral lines

The line profiles of spectral lines are very important for the understanding of stellar spectra. They contain information about the physical conditions, for example, the temperature, the density and the chemical composition of the object. A spectral line is broadened by, basically, three processes: Natural broadening, Doppler broadening and pressure or collisional broadening.

Natural broadening is an effect of the limited life time an electron has in a certain excited state. The reason for this is the energy-time-uncertainty which leads to a natural broadening of the line. The profile of the line shape can be described by a Lorentzian,

$$\phi(\Delta\lambda) = \frac{\Delta\lambda_L}{2\pi} \frac{1}{\Delta\lambda^2 + \Delta\lambda^2/4}, \quad (6.6)$$

where $\Delta\lambda_L = (\lambda_0^2/\pi c)\gamma_{\text{nat}}$ with γ_{nat} is the half width at half maximum of the Lorentzian.

Doppler broadening is caused by the motion of the atoms in the atmosphere. This motion results from thermal motion and follows the Maxwell-Boltzmann distribution. The line profile of this effect is described by a Gaussian

$$\phi(\Delta\lambda) = \frac{1}{\sqrt{\pi}\lambda_D} \exp\left[-\frac{\Delta\lambda^2}{\Delta\lambda_D^2}\right], \quad (6.7)$$

where λ_D is the Doppler width. The microturbulence parameter ξ (equation 3.20) in the results presented in this chapter is set to a typical value of 2 km s^{-1} , see Allard & Hauschildt (1995).

The state of the atom can also be disturbed by collisions with neutral atoms or by close encounters with the electromagnetic field of an ion. Such processes are also described by Lorentzian profiles. The overall line shape is then given by the convolution of the Doppler profile and the two Lorentz profiles, and is called a Voigt profile:

$$\phi(\Delta\lambda) = \frac{1}{\sqrt{\pi}\Delta\lambda_D} H(\alpha, y) = \frac{1}{\sqrt{\pi}\Delta\lambda_D} \frac{\alpha}{\pi} \int_{-\infty}^{+\infty} \frac{\exp(x^2)}{\alpha^2 + (y-x)^2} dx. \quad (6.8)$$

Here, $H(\alpha, y)$ is the Voigt function with $\alpha = 2\gamma\lambda_0^2/(4\pi c\Delta\lambda_G)$ the damping parameter, γ the damping constant and $y = \Delta\lambda/\Delta\lambda_G$. The Voigt profile is dominated by Doppler

broadening in the line core, the line wings are dominated by the Lorentzian damping profile.

For example, purely Gaussian lines are a good approximation for supernovae and giants, where the density is very small that pressure or collisional broadening can be neglected. Spectral lines of the sun, for example, are generally well approximated by Voigt profiles.

6.2 Results

In order to extend the Eulerian frame method in its applicability, the framework has been adopted to be used with atoms and molecules in LTE with Gaussian and Voigt shaped lines and coherent scattering. This modification only influences the calculation of the opacity χ and the character of scattering, see chapter 2. The formalism and the limitations of the method are similar to the treatment of two-level atoms in parameterized (toy) atmospheres.

The results presented in this section show the comparison between the Eulerian and Lagrangian formalism for atomic and molecular LTE lines with Gaussian and Voigt profiles. For the comparison of the atomic lines the broad H_α line, for the comparison of the molecular lines, a line of a CO band was chosen. To account for the limitations in the Eulerian formalism, only a velocity field which correspond to one Doppler width of those spectral lines is used. The hypothetic line scattering albedo in LTE models was set to $\epsilon_l = 1$, therefore, only scattering in the continuum was considered. The spectral lines of the G-type star are Voigt shaped, as the density is very high and collision occur often. Therefore, the Gaussian H_α line is only shown here for testing purposes. The spatial resolution of the here presented results is $(n_r, n_\theta, n_\phi) = (65, 33, 65) = 139, 425$ and the solid angle resolution is $n_{\theta,c} = n_{\phi,c} = 64$.

6.2.1 The atomic H_α line with Gauss and Voigt profiles

As a first test, the Eulerian formalism was applied in a static atmosphere. The corresponding comparison is shown in figure 6.1 for the Gaussian and in figure 6.2 for the Voigt shaped H_α line. The agreement of the three dimensional, angle-dependent solution in the Eulerian frame with the one dimensional solution is excellent. In figure 6.3 and 6.4 the

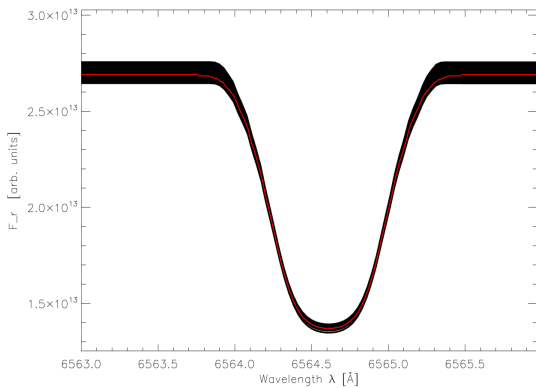


Figure 6.1: Comparison of the Gaussian H_α line in the 1D (red) and the 3D (black) Eulerian formalism in a static atmosphere

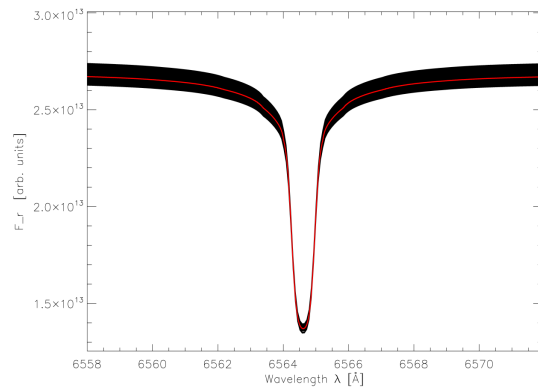


Figure 6.2: Comparison of the Voigt H_α line in the 1D (red) and the 3D (black) Eulerian formalism in a static atmosphere

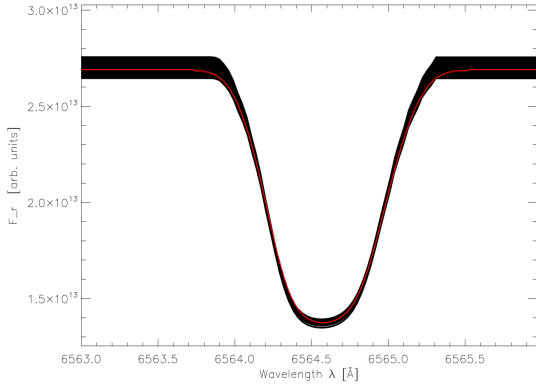


Figure 6.3: Comparison of the Lagrangian and the Eulerian formalism with a Gaussian shaped H_α line. The magnitude of the velocity $v_{\max} = 15.66 \text{ km s}^{-1}$ corresponds to one Doppler width of the line

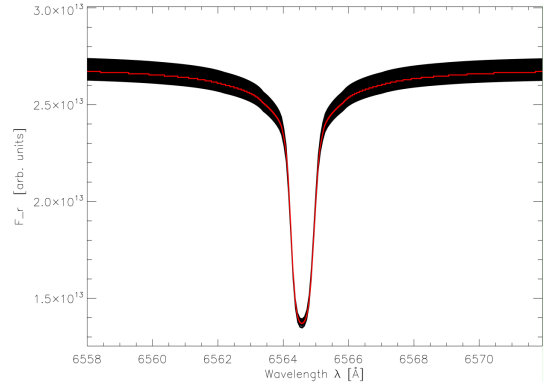


Figure 6.4: Comparison of the Lagrangian and the Eulerian formalism with a Voigt shaped H_α line. The magnitude of the velocity $v_{\max} = 15.66 \text{ km s}^{-1}$ corresponds to one Doppler width of the line

magnitude of the velocity field $v_{\max} = 15.66 \text{ km s}^{-1}$ corresponds to one Doppler width of the H_α line. The typical spectral emission peak is not visible in those spectra as the velocity field compared to the Doppler width is too low to produce a visible separation between the emission and absorption feature in the atmosphere. The agreement between the two formalism with Gaussian and Voigt shaped lines is excellent.

6.2.2 More atomic lines with Gauss and Voigt profiles

A comparison of the two formulations with more spectral lines is shown in figure 6.5 and 6.6. The rest wavelengths, thermal velocities and Doppler widths of the lines used is given

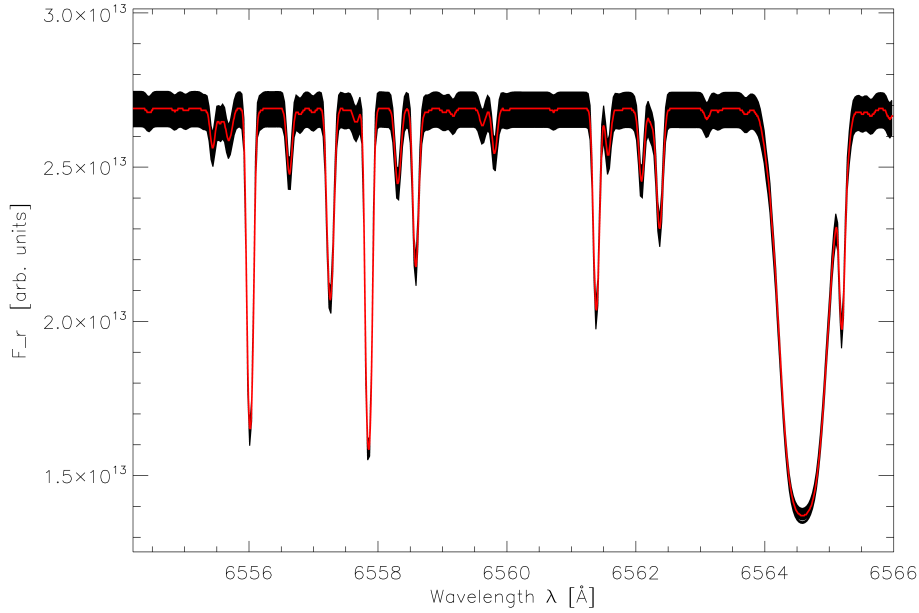


Figure 6.5: Comparison of the Lagrangian (red) and the Eulerian (black) formalism. The magnitude of the atmospheric velocity field is $v_{\max} = 10 \text{ km s}^{-1}$ which corresponds roughly to five Doppler widths of the smallest spectral line. This figure shows Gaussian shaped lines.

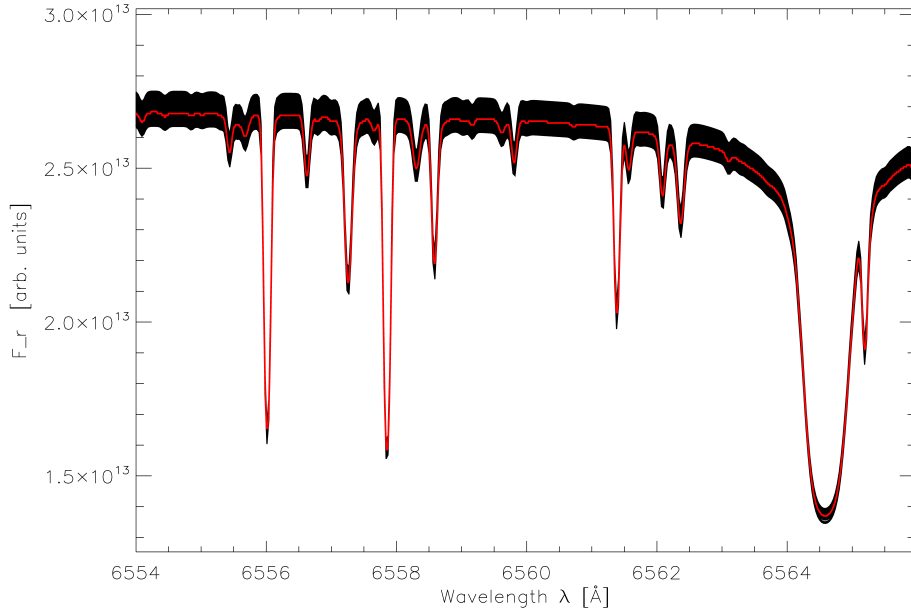


Figure 6.6: Comparison of the Lagrangian (red) and the Eulerian (black) formalism. The magnitude of the atmospheric velocity field is $v_{\max} = 10 \text{ km s}^{-1}$ which corresponds roughly to five Doppler widths of the smallest spectral line. This figure shows Voigt shaped lines.

in appendix B. In the atmosphere, the magnitude of the velocity field is $v_{\max} = 10 \text{ km s}^{-1}$ which corresponds roughly to five Doppler widths of the smallest line. The figures show that the agreement between the two approaches is very good.

The Eulerian formulation can be used in applications with many spectral lines as long as the magnitude of the velocity field in the atmosphere corresponds to a few Doppler widths of the narrowest line.

6.2.3 Molecular lines with Gauss and Voigt profiles

In general, the Eulerian formalism can be used with molecular lines, but, as molecules have rotational and vibrational spectral bands which can include hundreds of single lines with small Doppler widths, the application of the formalism is very time consuming because the opacities for each single line have to be computed in all volume element for all solid angles. Furthermore, it is necessary to figure out the line with the smallest Doppler width in the molecular band and then ensure that the magnitude of the velocity field does not extend a few Doppler widths of this line. In this work, a CO line out of a CO molecular band was isolated and compared in the Lagrangian and Eulerian formalism. The magnitude of the velocity field was set to $v_{\max} = 2.54 \text{ km s}^{-1}$ which corresponds to one Doppler width of the CO line, figure 6.7 and 6.8 shows the comparison with a Gaussian and Voigt profile. The agreement between the two solutions for molecular lines is also confirmed.

A spectrum from a molecular band was not computed during this work but it is possible to do when the limitations of the Eulerian formalism are considered and enough computing power is available.

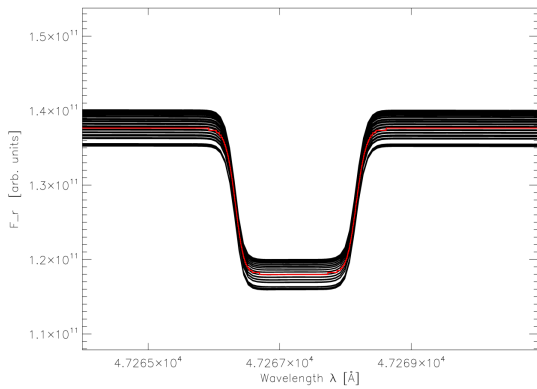


Figure 6.7: An isolated CO line from a CO band. The comparison of the Lagrangian (red) and Eulerian (black) formalism is excellent. The magnitude of the velocity field $v_{\max} = 2.545 \text{ km s}^{-1}$ corresponds to one Doppler width. The shape of the line is Gaussian.

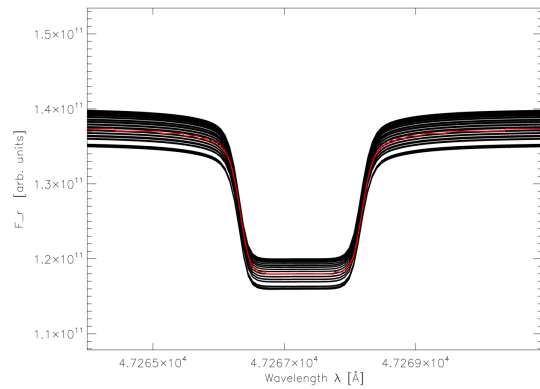


Figure 6.8: An isolated CO line from a CO band. The comparison of the Lagrangian (red) and Eulerian (black) formalism is excellent. The magnitude of the velocity field $v_{\max} = 2.545 \text{ km s}^{-1}$ corresponds to one Doppler width. The shape of the line is Voigt.

Chapter 7

The Eulerian formalism in other geometries

The comparison of the new developed three dimensional Eulerian framework to the one dimensional Lagrangian framework with help of the PHOENIX code has been successful as shown in the previous chapters. This comparison is the verification of the Eulerian approach developed in this work. The method can now be used to calculate the emergent spectrum from, for example, global circulation models with velocity fields in spherical geometry. In Chapter 8 this has been done for a Hot Jupiter model. In order to extent the usability of the Eulerian framework, it has been adopted to other geometries:

- Models from solar convection are usually described in cartesian geometry with periodic boundary conditions.
- Young stellar objects like circumstellar disks are best described in cylindrical geometry and
- interstellar moving medium models are usually described in cartesian geometry.

The limitations of the Eulerian formalism in those geometries correspond to those in spherical geometry, presented in chapter 5. During this work, the Eulerian formalism has been implemented in all before mentioned geometries in the 3DRT module of the stellar atmosphere code PHOENIX/3D. The formulation of the Eulerian formalism in other geometries than the spherical is similar to the formulation in spherical geometry, as the radiative transfer equations are solved, in this work, along characteristics. They are tracked globally through any three dimensional geometry, which leads to differences¹ depending on the geometry, see section 4.4.

This chapter explains the Eulerian formalism in cartesian geometry with and without periodic boundary conditions in section 7.1 and shows the influence of an atmospheric velocity field onto the solutions. It briefly describes the formalism in cylindrical geometry in section 7.2.

7.1 Cartesian with and without PBCs

The calculation of the radiative quantities in cartesian geometry with and without periodic boundary conditions is similar, the only difference between the two descriptions is where

¹differences in the spectrum formation

the characteristics are terminated in the three dimensional grid. Without periodic boundary conditions, they are terminated when they leave an outermost $(x, y), (x, z)$ or (y, z) face. With periodic boundary conditions, characteristics which leave a (x, z) or (y, z) face are continued on the opposite face of the grid until they hit the upper or lower boundary, where they are finally terminated. The consistency test of the construction of the $\Lambda^{O,*}$ operator explained in section 5.1 can directly be applied in cartesian geometry with and without periodic boundary conditions. This test was successful in both descriptions.

7.1.1 Cartesian with PBCs

In cartesian geometry with periodic boundary conditions, it is possible to set up a plane parallel atmospheric structure. The one dimensional, spherical symmetric atmospheric setup explained in section 6.1 is utilized and interpolated onto the z direction in the cartesian three dimensional grid at every (x, y) point for testing. Therefore, the atmospheric quantities depend only on the z coordinate. The atoms are assumed to be in local thermodynamic equilibrium. The calculation of the opacity χ and a specific line profile does not depend on the spatial structure of the atmosphere, therefore only Gaussian shaped spectral lines are presented here. In the computation of the emergent spectrum of the plane-parallel atmosphere, a wavelength range was used which corresponds to the range used in section 6.2.2. The specific lines with their rest wavelength, Doppler widths and thermal velocities can be found in appendix B. The limiting parameter which cuts off characteristics with grazing angles, explained in section 4.4.4, is set to 16. The spatial resolution is $(n_x, n_y, n_z) = (61, 61, 61) = 226.981$ and the solid angle resolution is $n_{\theta,c} = n_{\phi,c} = 64$. The other atmospheric properties correspond to the setup in section 6.1, including the construction of the velocity field.

Figure 7.1 shows the emergent spectrum of all outermost voxels of the static plane parallel atmosphere in black and the plane parallel atmosphere with a velocity field with

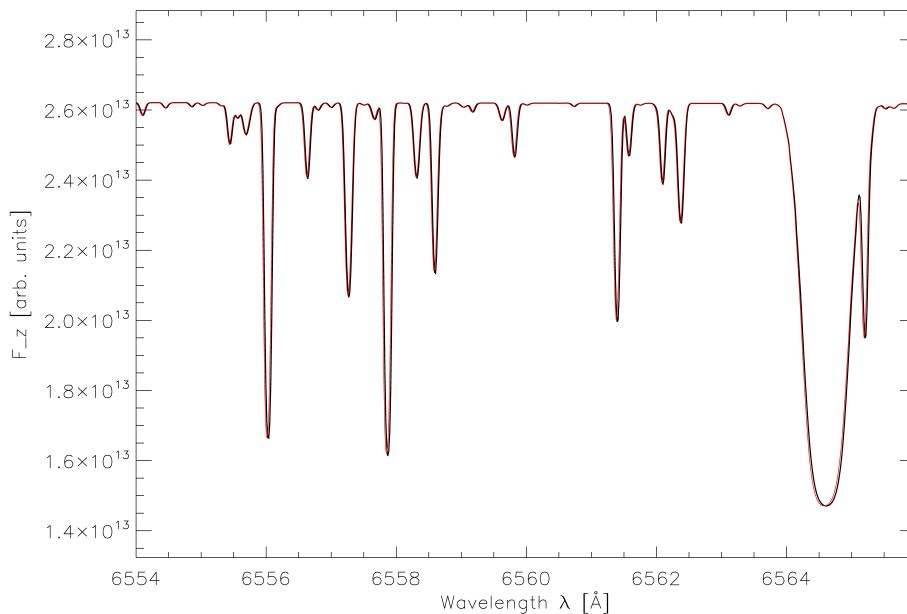


Figure 7.1: The emergent spectrum from all outermost voxels in cartesian geometry with PBC. Black: static atmosphere and red: with a velocity field with $v_{\max} = 10 \text{ km s}^{-1}$, which corresponds to roughly five Doppler width of the smallest spectral line. This figure shows Gaussian shaped lines.

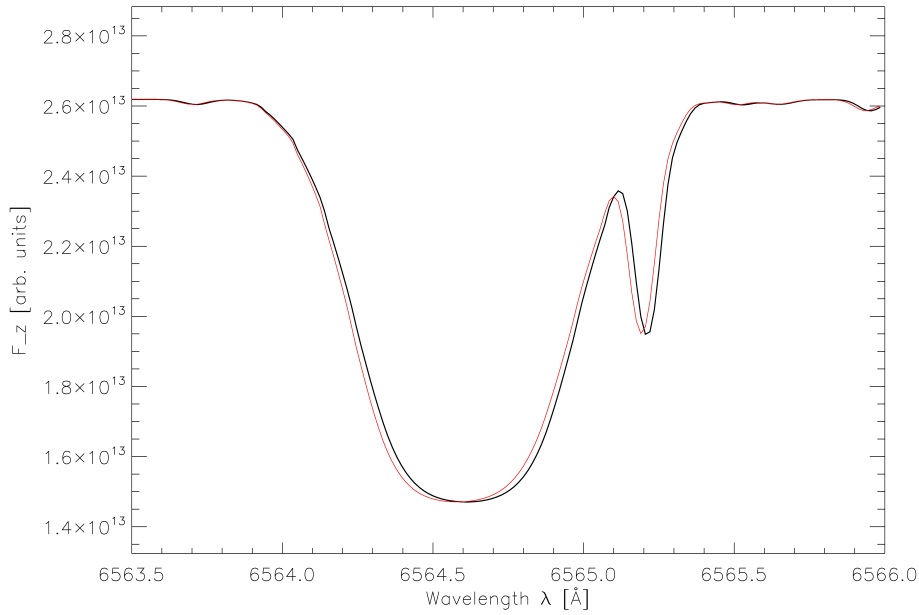


Figure 7.2: Separated broad lines from the spectrum in figure 7.1. Black: static atmosphere and red: with a velocity field with $v_{\max} = 10 \text{ km s}^{-1}$ which corresponds to roughly five Doppler widths of the smallest spectral line in figure 7.1. This figure shows Gaussian shaped lines.

$v_{\max} = 10 \text{ km s}^{-1}$ in red. The difference between the two spectral lines is not easily visible. This figure should give an overview over the spectral range used in the calculation. Figure 7.2 shows separated, broad spectral lines and figure 7.3 shows separated, narrow spectral lines

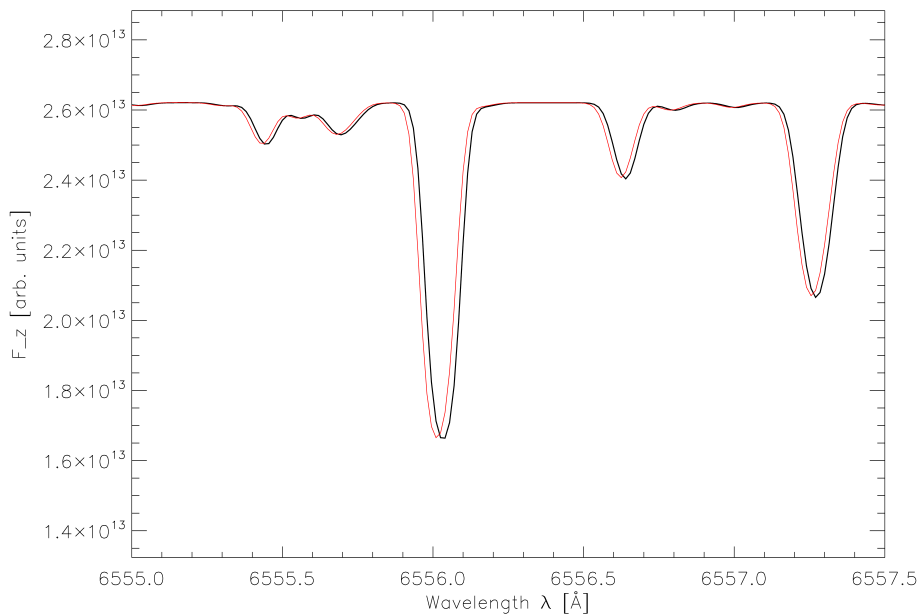


Figure 7.3: Separated small lines from the spectrum in figure 7.1. Black: static atmosphere and red: with a velocity field with $v_{\max} = 10 \text{ km s}^{-1}$ which corresponds to roughly five Doppler widths of the smallest spectral line in figure 7.1. This figure shows Gaussian shaped lines.

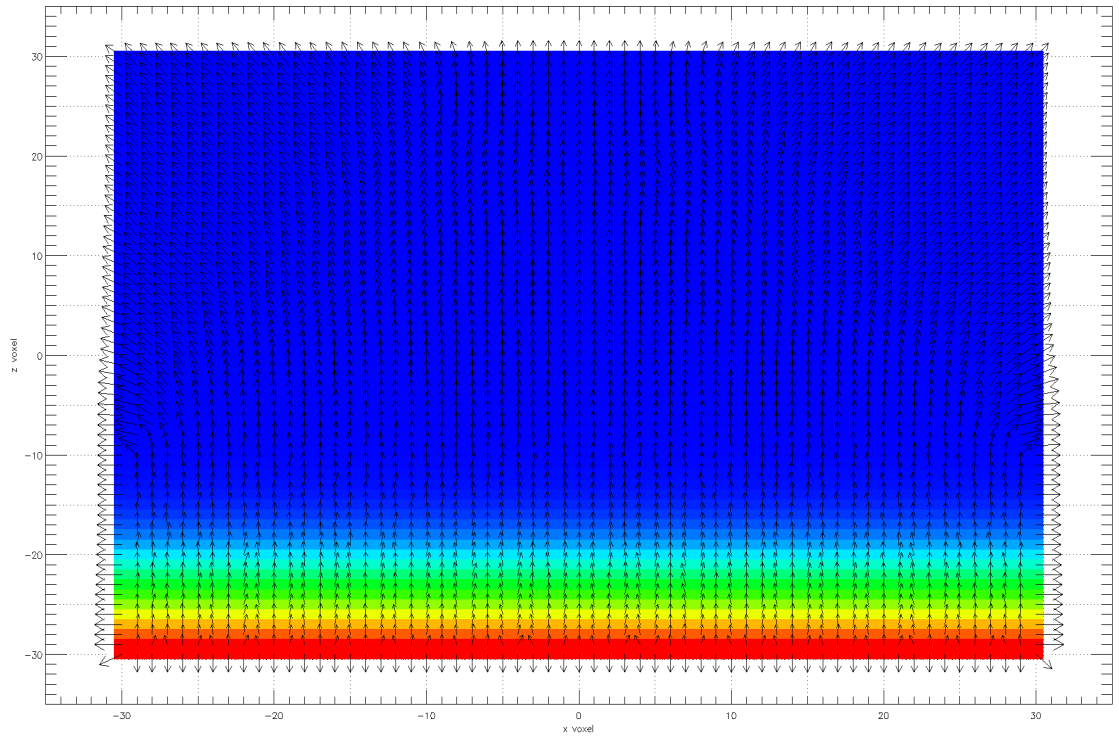


Figure 7.4: The flow of the (logarithmic) flux in cartesian geometry in the plane-parallel atmospheric structure without PBCs. Arrows: flux and colors: temperature in a $(x - z)$ plane.

from the spectrum in figure 7.1. The influence of the atmospheric velocity field onto the formation of the spectral lines is clearly visible. The figures show that the Eulerian frame formalism is working in cartesian geometry with periodic boundary conditions.

7.1.2 Cartesian without PBCs

In cartesian geometry without PBCs, it is not possible to construct a simple atmospheric structure to show the influence of a velocity field onto the spectrum formation in a simple, but global², manner. Constructing an atmosphere, starting in the central voxels would lead to different flux values in different outermost voxels because the geometrical path length to the outermost voxels is different. Setting up a plane parallel atmosphere structure would cause that the energy would flow out of the cartesian box at the sides and the bottom because the PBCs are missing, see figure 7.4. This also leads to different flux values in different outermost voxels. To show the influence of a velocity field onto the spectrum formation in cartesian geometry, the flux is only plotted in one outermost voxel. The atmospheric setup is, for testing, plane-parallel and is similar to the one in the last section.

Figure 7.5 shows the emergent spectrum in the central outermost voxel in the cartesian atmosphere without PBCs. Here, only emission lines are seen, which is caused by the geometry: The energy from the deep layers of the atmosphere, flows mainly out of the grid at the sides and to the bottom, as the PBCs are missing. Therefore, the spectrum is

²global means here: in the cartesian geometry with PBCs, the flux was plotted in **all** outermost voxels, therefore, the influence of the velocity field onto the spectrum formation was shown in a greater extend. In cartesian geometry without PBCs this is not possible.

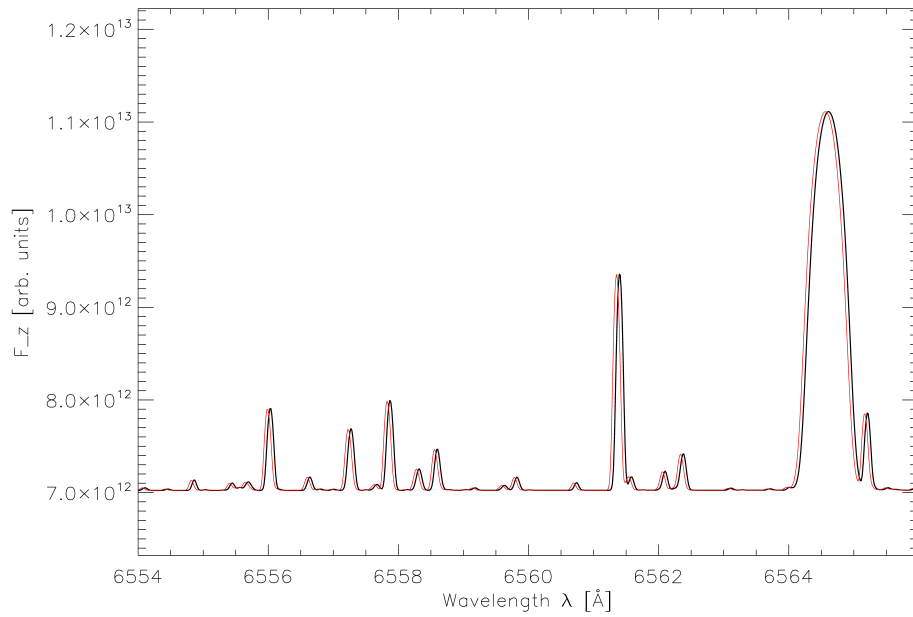


Figure 7.5: The emergent spectrum from the central voxel on top of the cartesian geometry without PBC. Black: static atmosphere and red: with a velocity field with $v_{\max} = 10 \text{ km s}^{-1}$, which corresponds to roughly five Doppler width of the smallest spectral line. This figure shows Gaussian shaped lines.

dominated by emission features arising in the shallow layers of the atmosphere. Again, the influence of the velocity field is not clearly visible in the figure due to the wide spectral

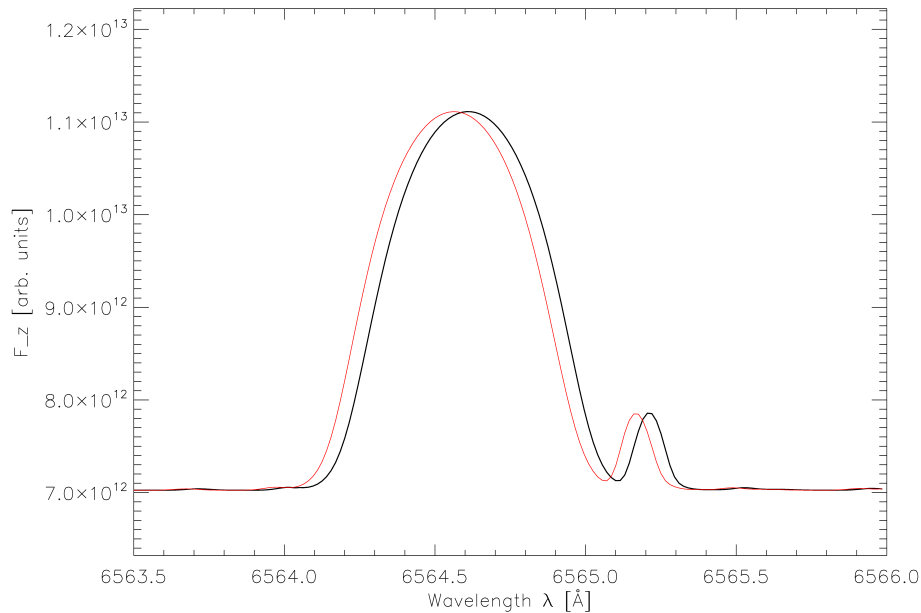


Figure 7.6: The emergent spectrum from the central voxel on top of the cartesian geometry without PBC for a separated spectral line from figure 7.5. Black: static atmosphere and red: with a velocity field with $v_{\max} = 10 \text{ km s}^{-1}$, which corresponds to roughly five Doppler width of the smallest spectral line in figure 7.5. This figure shows Gaussian shaped lines.

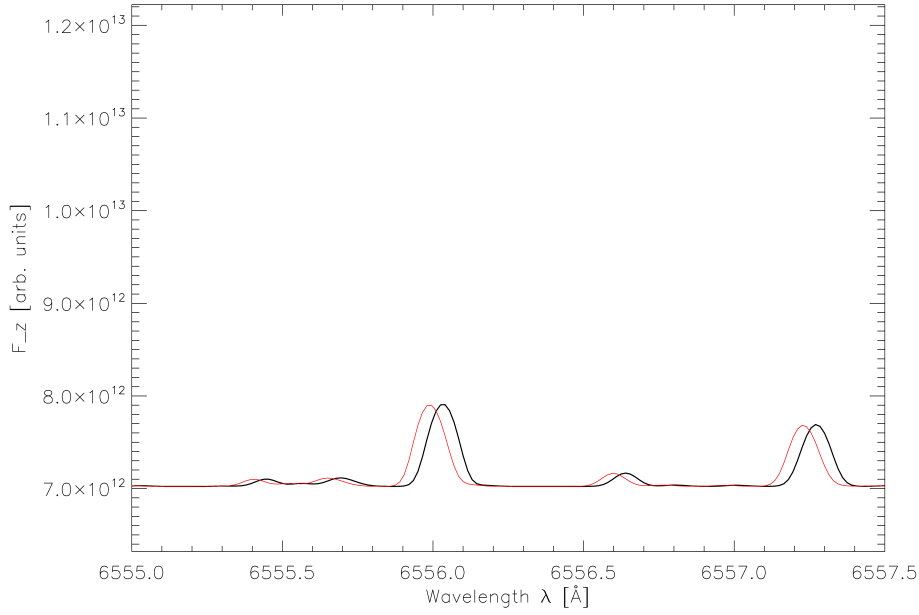


Figure 7.7: The emergent spectrum from the central voxel on top of the cartesian geometry without PBC for a separated spectral line from figure 7.5. Black: static atmosphere and red: with a velocity field with $v_{\max} = 10 \text{ km s}^{-1}$, which corresponds to roughly five Doppler width of the smallest spectral line in figure 7.5. This figure shows Gaussian shaped lines.

range. Figure 7.6 and 7.7 shows two separated lines of the spectrum in figure 7.5. In those figures the influence of the velocity field onto the spectrum formation is clearly visible.

7.2 Cylindrical

In cylindrical geometry, it is also not possible to construct a simple atmosphere structure to investigate the influence of a velocity field onto the spectrum formation in all outermost voxels, for the same reasons as in the cartesian geometry without PBCs. Therefore, no spectra are shown here. The formulation of the Eulerian formalism in this work is similar in each geometry³ and the construction of the scattering operator has been verified in cylindrical geometry. Detailed analysis of how a velocity field influences spectral lines in cylindrical geometry is subject of further work.

³because the radiative transfer is solved along characteristics

Chapter 8

Application examples

After the description of the Eulerian formalism, the comparison to the Lagrangian formalism and the adaption of Eulerian formalism to other three dimensional coordinate systems in the last chapters, we proceed to application examples. This chapter outlines a few properties of the application of the Eulerian frame formalism to a model of solar convection in section 8.2 and onto a global circulation model of a Hot Jupiter in section 8.3. Section 8.1 summarizes a few properties of three dimensional hydro-dynamical models. A detailed analysis and the comparison to observed objects are subject of further work as the results presented here should only show the application of the Eulerian formalism in atmospheres with arbitrary velocity fields.

8.1 Three dimensional hydro-dynamical models

In general, hydro-dynamical models are based on the conservation of mass, momentum and energy. The energy is usually considered to consist of convection, thermal and radiative energy. The equations of hydro-dynamics describe the exchange of those energy forms, usually the radiation is treated in a very simple manner¹. The high computational costs to calculate the radiation field in three dimensions with the inherent, arbitrary, velocity field which, in turn, would be used as input in the next step of the the hydro-dynamical calculation is one reason for this.

Based on the specific three dimensional hydro-dynamical problem, classical assumption necessary in one dimensional models can be dropped. For example, the concept of micro- and macro-turbulence (Asplund, 2000). The Eulerian frame method applied to a hydro-dynamical snapshot structure from the sun with a inherent velocity field, reproduces the typical line profile including the asymmetries, as we shall see in section 8.2. Furthermore, the concept of the mixing length theory (Böhm-Vitense, 1958; Canuto & Mazzitelli, 1991) which was necessary to compute the convective energy flux in 1D models are obsolete in 3D hydro-dynamical models. Those advantages, including the Eulerian frame formalism developed in this work, lead to more realistic three dimensional simulations of stellar/solar atmospheres.

8.2 A model of solar convection

The solar convection model used in this work is a snapshot from a hydro-dynamical calculation (Caffau et al., 2007) from the CO⁵BOLD computer code (Freytag et al., 2008;

¹usually, only a formal solution is performed

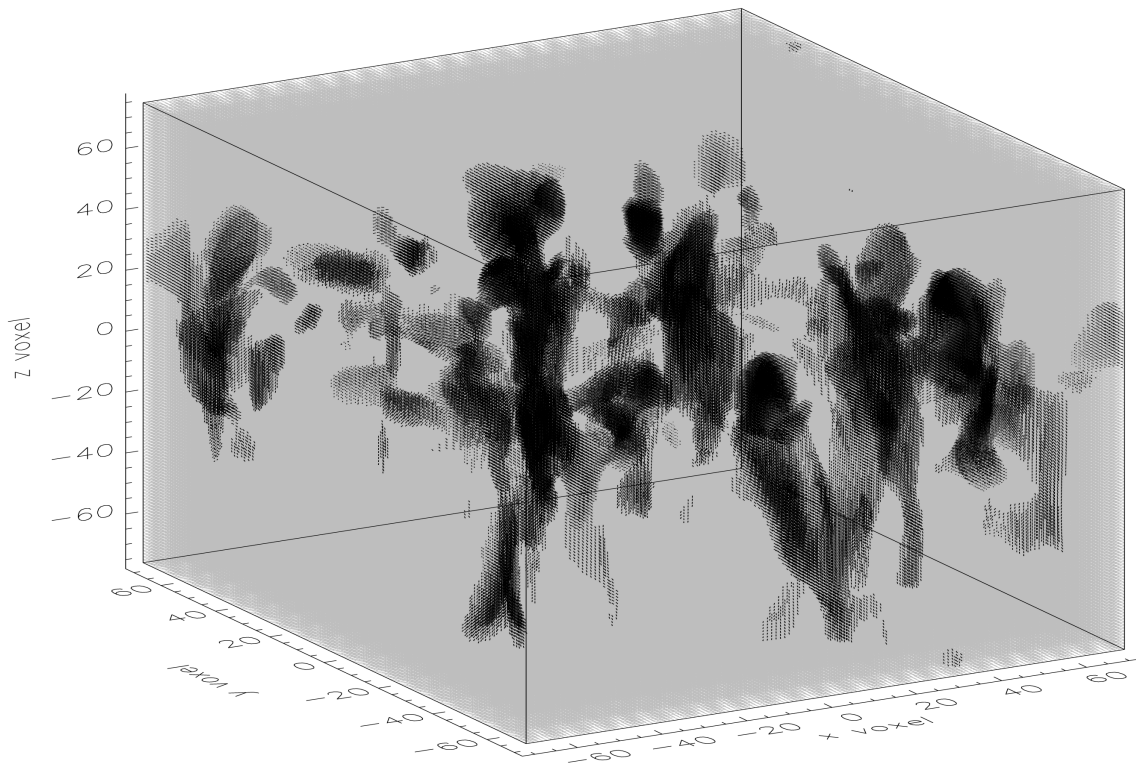


Figure 8.1: The velocity field vectors in the solar convection structure with magnitudes higher than $1/2$ of the maximum value in the whole structure. The figure shows the global structure of the velocity field in the solar convection model.

Wedemeyer et al., 2004).

The spatial extend of the atmosphere in x and y direction is 5.600 km and in z direction 2.253 km, a single voxel has a spatial extend of $(x, y, z) = (40 \text{ km}, 40 \text{ km}, 15.02 \text{ km})$. Therefore, the number of voxels is $(n_x, n_y, n_z) = (140, 140, 150)$ which gives a total of 2.940.000 voxels. The gas temperature ranges from $T_{\max} = 16,319.1 \text{ K}$ to $T_{\min} = 2,986.8 \text{ K}$ and the velocity has a maximum magnitude of $v_{\max} = 11.6 \text{ km s}^{-1}$, a minimum of $v_{\min} = 0.01 \text{ km s}^{-1}$ and a mean velocity of 2.287 km s^{-1} in the whole three dimensional grid.

The velocity field in the solar convection model is arbitrary ('chaotic') and parts of the atmosphere are rising up or falling down. Figure 8.1 shows the velocity vectors which have a absolute value with more than a half of the maximum velocity in the whole model. It is clearly visible that parts of the atmosphere are either moving up or down in 3D bubbles. To visualize the velocity field in greater detail, figure 8.2 shows the temperature and the inherent velocity field in the central $(x - z)$ plane and figure 8.3 shows the values in the central $(x - y)$ plane.

The rising or falling bubbles produce a visible granulation on the atmospheric surface of the sun, the average (observed) size of those cells is 1.300km (Gray, 2008). This granulation effect is translated into spectral line asymmetries in the emergent spectrum of the object (Dravins, 1987*b,a*). For example, in normal solar granulations more light comes from the hot, rising material and less from the cold, falling material (Gray, 2008), figure 8.4 shows this effect on the example of the emergent spectrum. In the top panel, the cool, falling material produces a slightly red shifted line whereas the hot, rising material produces a much stronger blue shifted line. The combination of the two lines gives the line asymmetry,

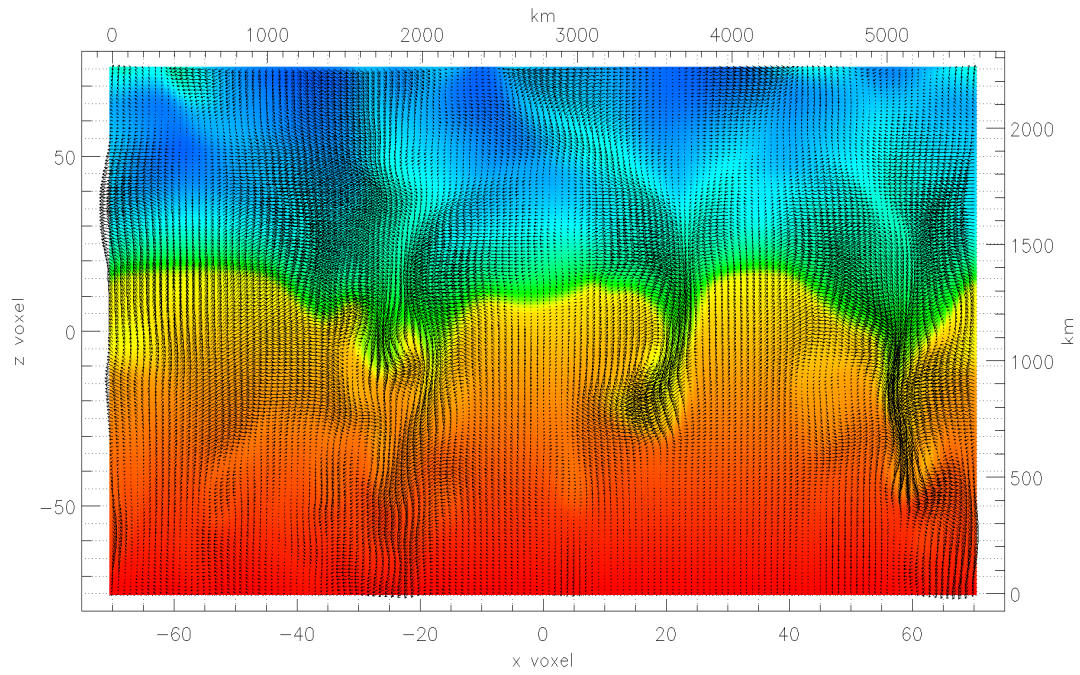


Figure 8.2: The arbitrary velocity field (arrows) and the temperature (colors) in the solar convection model in the central ($x - z$) plane

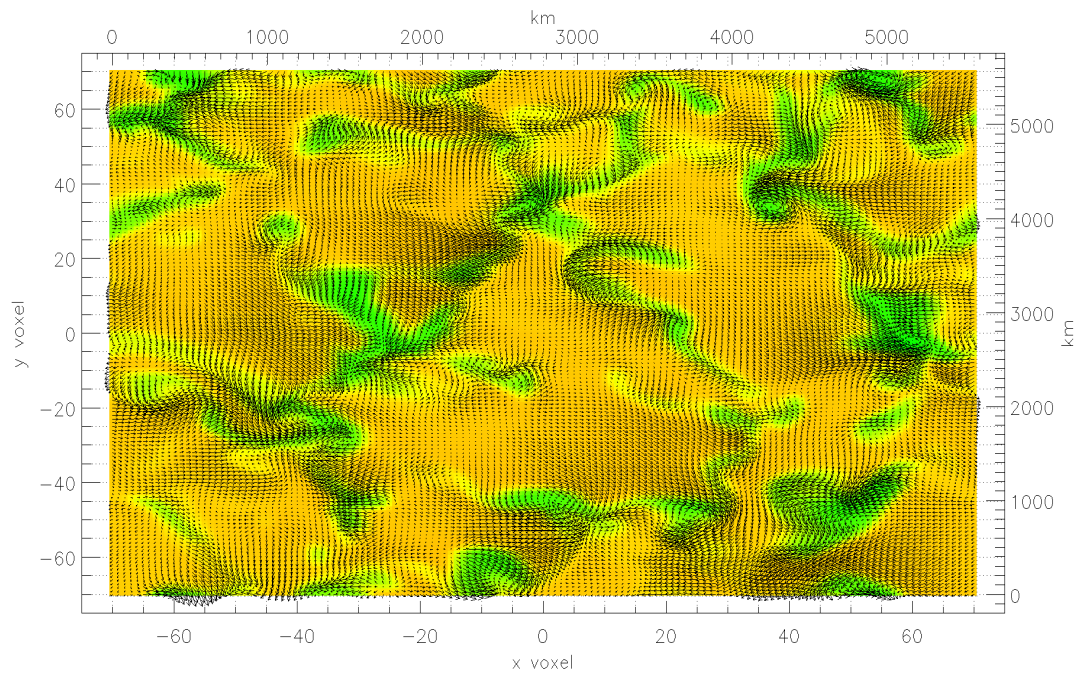


Figure 8.3: The arbitrary velocity field (arrows) and the temperature (colors) in the solar convection model in the central ($x - y$) plane

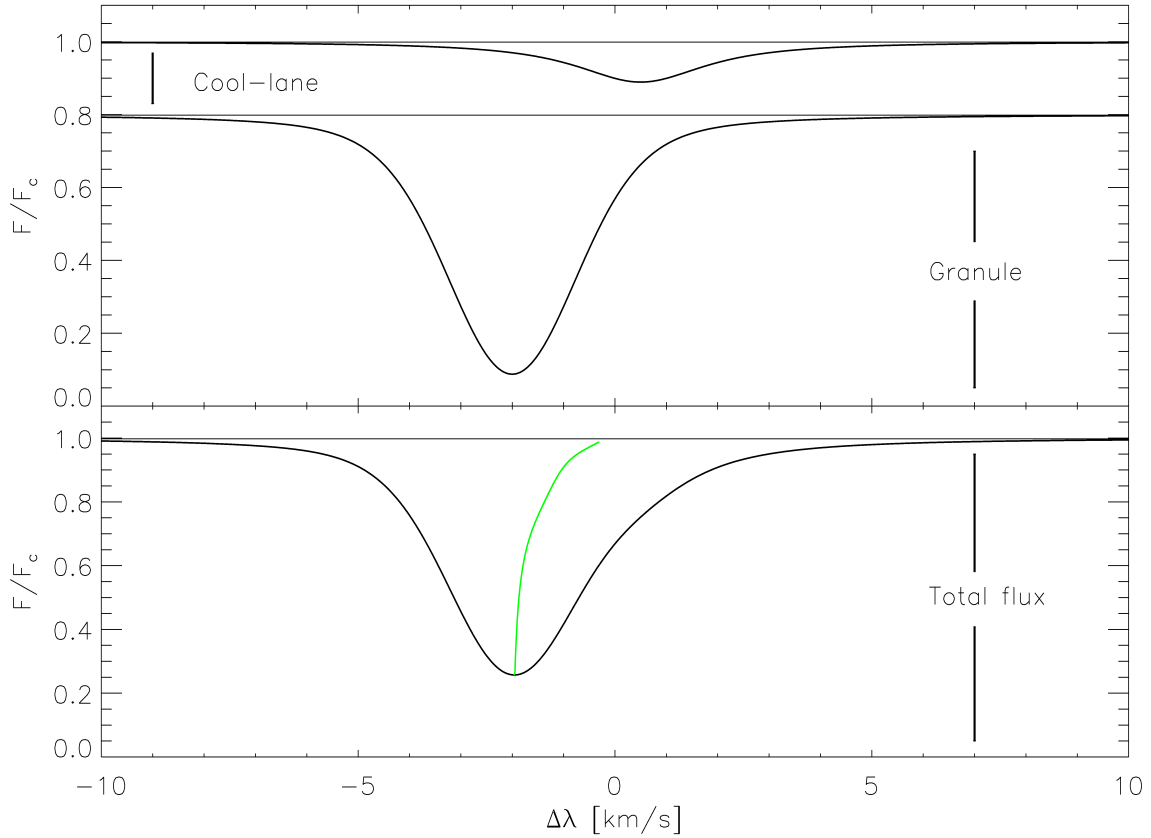


Figure 8.4: Profile formation in a convective atmosphere. The upper panel shows the spectral line in the Cool-lane and the spectral line in the Granule. The emergent spectrum is the summation of both, as shown in the bottom panel. The bisector (in green) is plotted to visualize this typical asymmetries in convective atmospheres.

as shown in the bottom panel in figure 8.4. The main part of the profile comes from the granules and is blue-shifted. The red-shifted spectral line from the Cool-lane is much weaker and acts mainly as a perturbation on the profile of the granules. This results in a depressed red wing of the spectral line. Therefore, the bisector² of such profiles has a drift to the redward side of the spectrum.

This asymmetry is reproduced in the solar convection models with the inherent velocity field. As an input for the radiative transfer calculation in the Eulerian frame, the solar convection model, as described, in cartesian geometry with PBCs is used and interpolated onto a $(n_x, n_y, n_z) = (141, 141, 151)$ voxel grid. In order to verify the asymmetries, a Li line with the solar abundances of $\epsilon_{Li} = 1.05$ was taken³. The radiation field was discretized with $n_{\theta,c} = n_{\phi,c} = 128$ solid angle points. In order to account for the limitations in the Eulerian frame, a further calculation with more solid angle points should have been made to verify that the differences in the spectral lines vanishes (see section 5.4). Unfortunately, this was not possible due to insufficient computer resources⁴.

²the bisector connects points of equal flux and marks the middle between them

³the minimum Doppler width of Li in the model is $2.105 \cdot 10^{-2}$ Å, the minimal thermal velocity is 0.941 km s^{-1} , therefore, the maximum magnitude of the velocity field corresponds to approximately 12,4 Doppler widths

⁴This calculation with approximately three million voxels, 126 wavelength points and $n_{\theta,c} = n_{\phi,c} = 128$ solid angle points in the Eulerian frame took 41,5h on 4096 CPUs

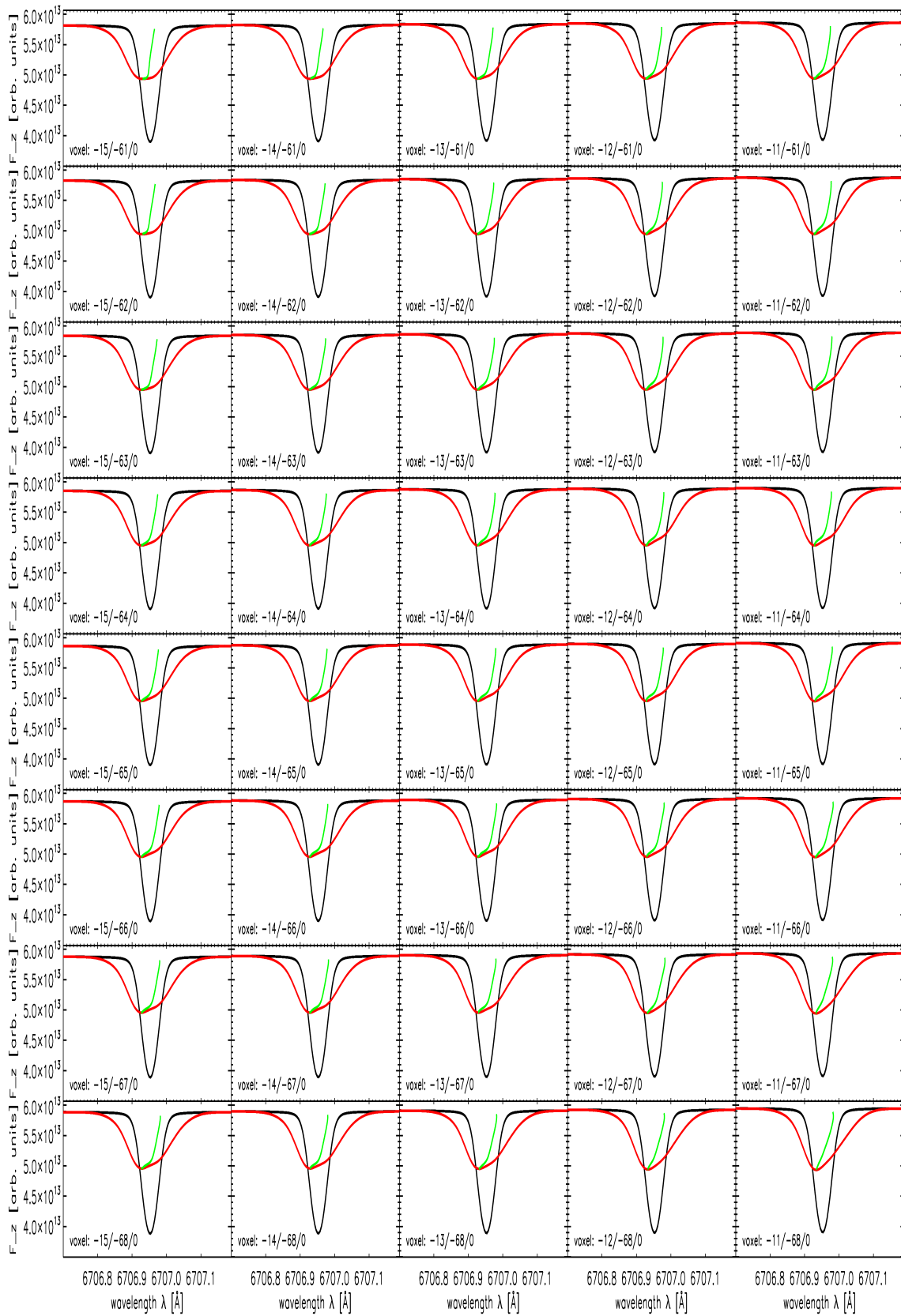


Figure 8.5: Selected spectra from the top of the cartesian solar convection model. The black line shows the spectrum with no velocity field, the red the spectrum with the treatment of the velocity field. The green line is the bisector of the asymmetric line.

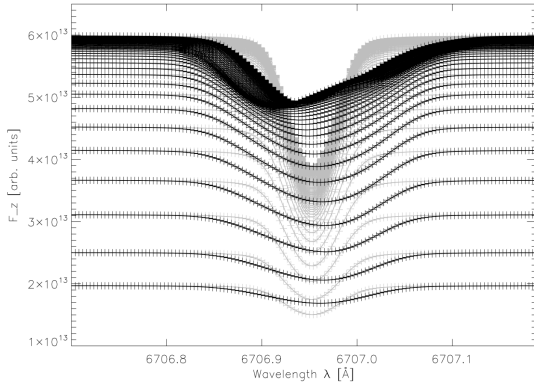


Figure 8.6: The formation of the spectral line in voxels along the z axis for the first 65 layer from the top. The voxel coordinates in the (x, y) plane are $(x, y) = (-13, -64)$. Grey: static atmosphere and black: moving atmosphere

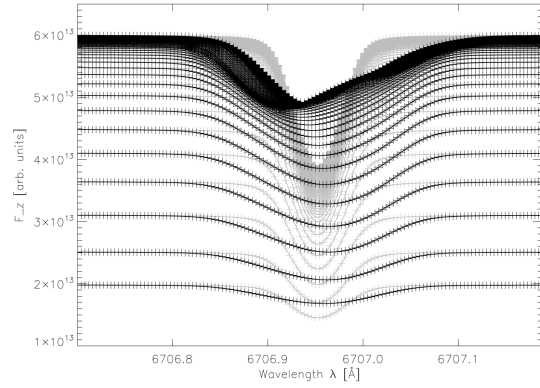


Figure 8.7: The formation of the spectral line in voxels along the z axis for the first 65 layer from the top. The voxel coordinates in the (x, y) plane are $(x, y) = (-13, -65)$. Grey: static atmosphere and black: moving atmosphere

The micro-turbulence parameter ξ (equation 3.20) was set to zero, as mentioned in section 8.1. Figure 8.5 shows the emergent spectrum on top of the cartesian atmosphere for a few selected voxels. The black line shows the calculation with no velocity field, the red line the calculation in the Eulerian frame with a velocity field, and the green bisectors show the asymmetries of the lines. The synthetic model atmosphere including the Eulerian radiative transfer calculation reproduces the expected line asymmetries very good. The formation of the spectral line in different voxels along the z axis is shown in figure 8.6 and 8.7. The grey lines show the spectral lines in the static atmosphere, the black line the spectra with the treatment of the velocity field. The figures shows only the first 65 layer

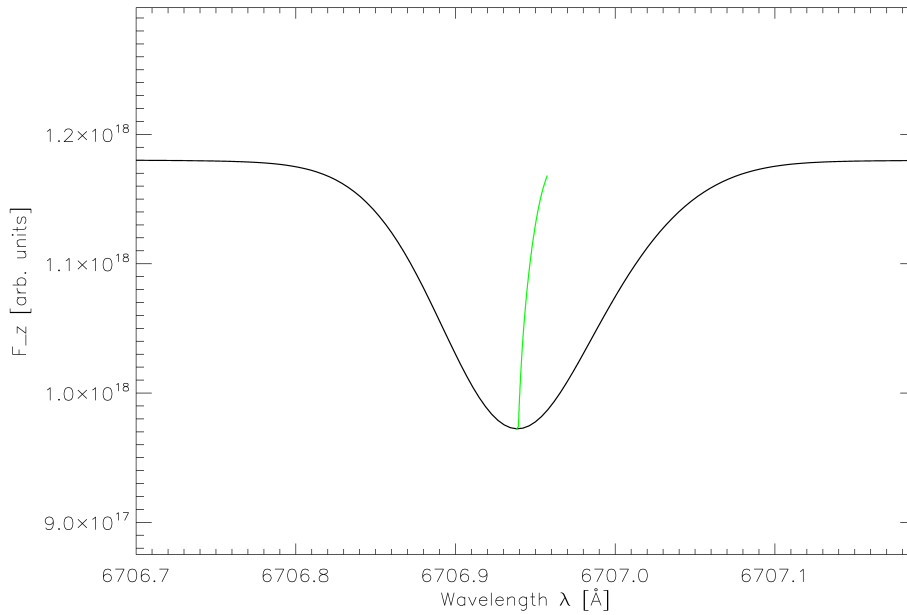


Figure 8.8: This figure shows the summarized spectrum from all outermost voxels in the cartesian grid. The green line is the bisector, the asymmetry is clearly visible.

from the top. It is clearly visible that the velocity field moves the line depending on the current velocity vector in the voxel.

Finally, figure 8.8 shows the emergent spectrum summed over all outermost voxels in the cartesian grid. The asymmetric line profile is still clearly visible.

8.3 Hot Jupiter

The second model atmosphere with an 'arbitrary' velocity field used in this work is, in general, a Intermediate General Circulation Model (IGCM). It is a model atmosphere representing the Hot Jupiter exoplanet HD209458b (Rauscher & Menou, 2010) in spherical coordinates. Detailed analyses of the atmospheric properties and structure is given in Rauscher & Menou (2010), the relevant physics are explained in Menou & Rauscher (2009), here only a few properties are mentioned. Hot Jupiters are orbiting their parent stars with a period of a few days having a day and night side. The upper atmospheric layers are circulating due to the asymmetric temperature distribution on the day and night side leading to transonic wind speeds. Figure 8.9 and figure 8.10 visualizes⁵ the temperature and the velocity field in two selected layers, the day and night side is clearly visible.

The atmospheric structure has a numerical resolution of $(n_r, n_\theta, n_\phi) = (33, 48, 96) = 152.064$ voxels. The gas temperature in the whole grid ranges from 152.04 K to 2049.4 K, the velocity field has a maximum magnitude of 12.69 km s^{-1} , a minimum of $0.217 \cdot 10^{-4} \text{ km s}^{-1}$ and a mean velocity of 1.395 km s^{-1} . It is common to use the pressure as the vertical coordinate in IGCM models, therefore, the radius differs from column to column.

⁵for simplicity, no Miller cylindrical projection is used

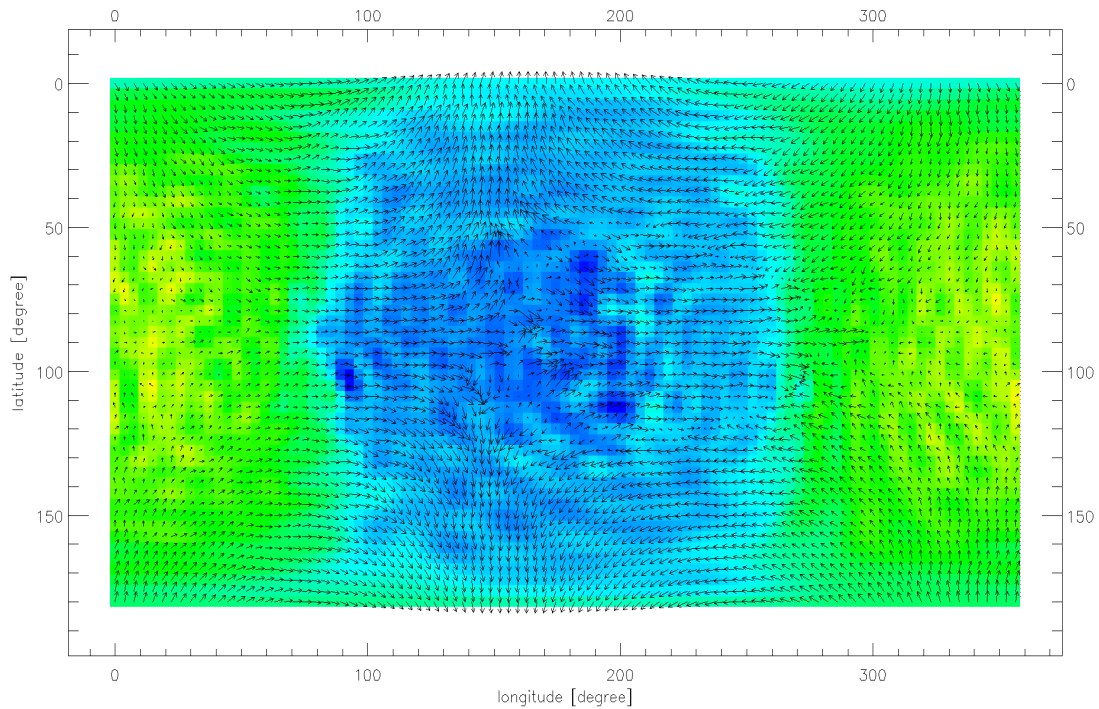


Figure 8.9: Temperature (colors) and the velocity field (arrows) in the Hot Jupiter model in the second layer from the top

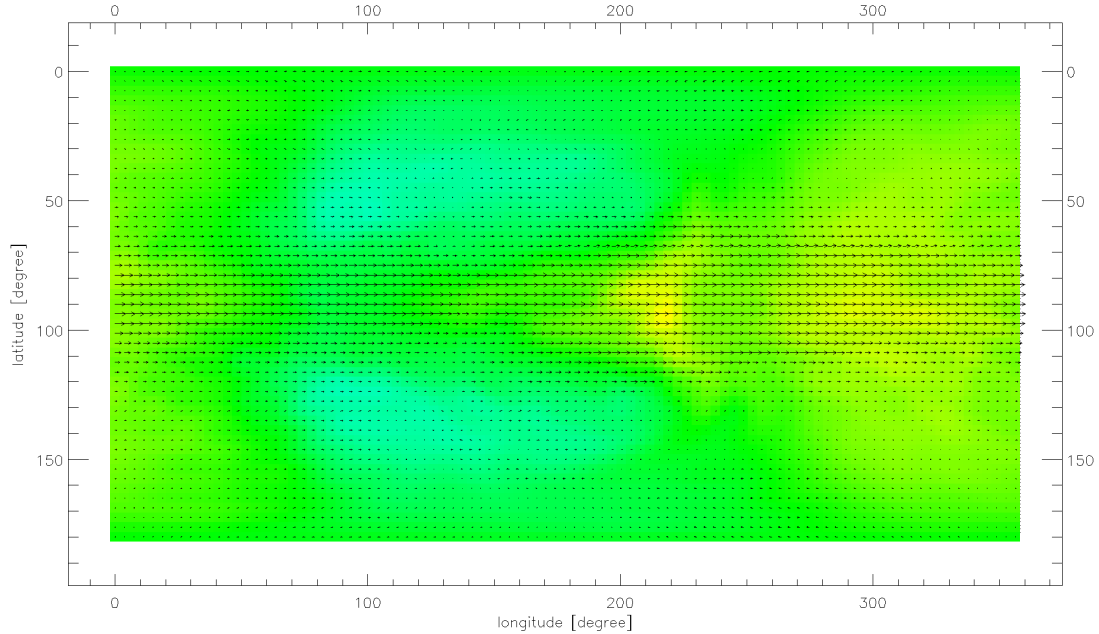


Figure 8.10: Temperature (colors) and the velocity field (arrows) in the Hot Jupiter model in the 28th layer from the top

The radiative transfer equations are solved in this work in spatial coordinate systems, thus, the original structure has to be interpolated: In a specific layer, the maximum and minimum radius is used. Then, in every column, the other atmospheric quantities are interpolated onto the radius grid. As no extrapolation is desired, the physical quantities are kept constant if the maximum radius in a specific column is reached, this leads to a reduced maximum velocity of 9.76 km s^{-1} . The resulting numerical resolution of the grid is then $(n_r, n_\theta, n_\phi) = (65, 49, 97)$ which gives 308.945 voxels.

For testing, a CO line⁶ out of a CO band was isolated and used⁷ in the calculation in order to show the influence of the velocity field onto the spectrum formation. The micro-turbulence parameter is set to $\xi = 2 \text{ km s}^{-1}$ (equation 3.20) for simplicity. Furthermore, the radiation field is discretized by $n_\theta = n_\phi = 256$ solid angle points. Computing time restrictions did not allow us to compute another model with a higher solid angle discretization in order to account for the limitations⁸ neither a calculation with $\xi = 0 \text{ km s}^{-1}$. The here presented results are, therefore, only schematic.

As estimated by Menou & Rauscher (2010), the influence of the atmospheric motion is clearly visible in the emergent spectrum. Figure 8.11 shows the spectrum in one outermost voxel⁹ on the equator on the day side and figure 8.12 shows the spectrum in one outermost voxel on the night side¹⁰ at the equator. In those figures it is clearly visible that the influence of the velocity field onto the spectrum formation is much stronger on

⁶the minimum Doppler width of the CO line in the model is $3.209 \cdot 10^{-1} \text{ \AA}$, the minimal thermal velocity is 2.03 km s^{-1} , therefore, the maximum magnitude of the velocity field corresponds to approximately 4,8 Doppler widths

⁷assuming solar abundances and a Voigt shaped line

⁸the differences in the spectra between different solid angle discretizations has to vanish, see section 5.4

⁹at longitude of 0°

¹⁰at longitude of 160°

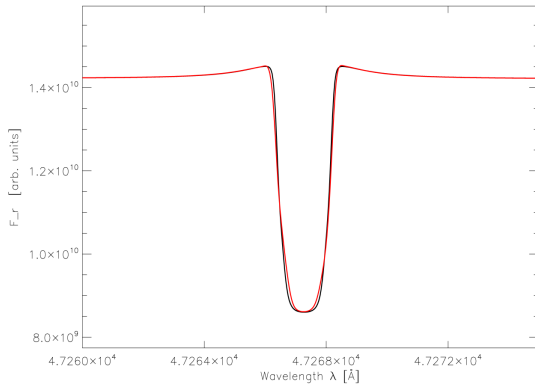


Figure 8.11: The spectrum from one voxel at (longitude, latitude) = $(0^\circ, 90^\circ)$ (day-side). Black: without the treatment of the velocity field and red: with the treatment of the velocity field.

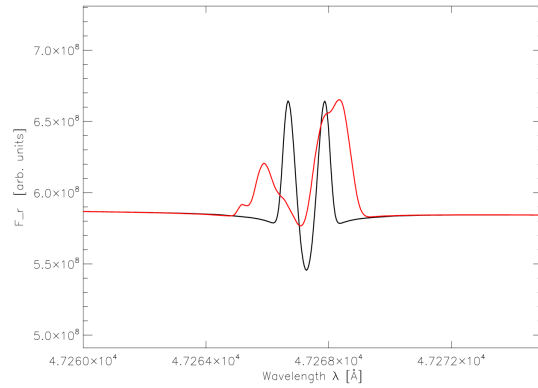


Figure 8.12: The spectrum from one voxel at (longitude, latitude) = $(160^\circ, 90^\circ)$ (night-side). Black: without the treatment of the velocity field and red: with the treatment of the velocity field.

the night side. Assuming that the Hot Jupiter has a inclination of 90° and a position direct in front of the host star, the observer sees only the surface of the star which has $0^\circ - 90^\circ$ in latitude and $90^\circ - 270^\circ$ in longitude. Figure 8.13 shows the summation of the flux vectors of the outermost voxels for this visible surface. This is only a schematic figure as a formal solution in the direction of the observer would be necessary to show the spectrum as the observer would observe it¹¹.

A detailed analysis of the relevant voxels the observer would see, a new calculation with $\xi = 0$ and a formal solution into the direction of the observer is subject of future work.

¹¹and, of course, the spectrum from the host star has to be added.

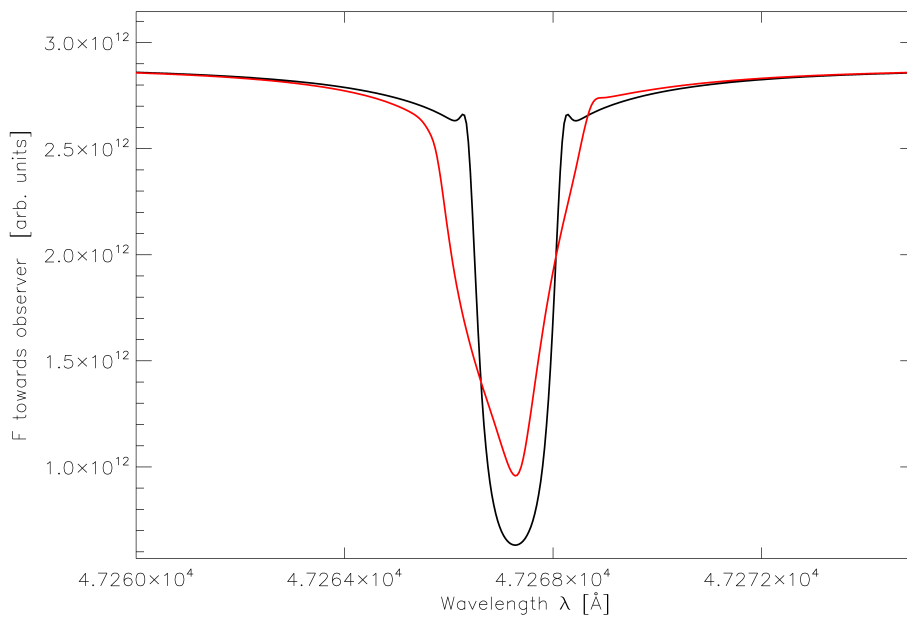


Figure 8.13: Summarized flux vectors towards the observer. Black: without the treatment and red: with the treatment of the velocity field.

Chapter 9

Conclusions and Outlook

9.1 Conclusions

This work described the treatment of arbitrary velocity fields in the Eulerian frame. The consistency of the new developed Eulerian frame method was verified. The results of Eulerian frame radiative transfer calculations in test atmospheres with two-level atoms with complete redistribution in spherical coordinates were compared to the Lagrangian frame formalism. This comparison showed that limitations on the usability of the Eulerian frame formalism have to be posed:

- The wavelength resolution has to be fine enough that the profile of the line can be resolved.
- The solid angle resolution of the radiation field has to ensure that the profile of the line is resolved.
- The Eulerian frame formalism is non-relativistic, therefore, the atmospheric velocity field should not extend 1.000 km s^{-1} .
- The gradient of the velocity field has to be small compared to the spatial resolution.

The agreement was shown to be very good when the limitations of the Eulerian frame formalism are taken into account.

The formalism was extended in its usability to handle atoms and molecules in local thermodynamic equilibrium with coherent scattering. Then, the results of 'real world' model atmospheres with radial velocity fields in the Eulerian and Lagrangian frame were compared. The agreement between the two formulations is excellent.

Depending on the specific problem, different coordinate systems are required to describe the problem in a useful manner. Therefore, the Eulerian frame formalism has been adopted to cartesian¹ and cylindrical coordinate systems. The consistency of the Eulerian frame formalism was verified in those geometries and an emergent spectrum of an atmosphere with a monotonic velocity field in cartesian geometry is shown.

Two snapshots from model atmospheres from hydro-dynamical calculation in cartesian and spherical geometry with an inherent velocity field were used as input into the Eulerian frame radiative transfer calculations. The influence of the inherent velocity fields onto the spectrum formation was shown. The spectrum of the solar convection model, calculated in the Eulerian frame, reproduced the typical asymmetries of convective atmospheres. The influence of a atmospheric velocity field onto the spectrum formation in the IGCM model

¹with and without periodic boundary conditions

of a Hot Jupiter atmosphere is clearly visible. These obtained results are only schematic, as only application examples of the Eulerian frame formalism in arbitrary velocity fields are shown in this work, a direct comparison to observations are pending.

9.2 Outlook and future work

One of the most crucial applications of the Eulerian frame formalism would be to compare the results of the Eulerian radiative transfer calculation of the sun to observations. This comparison would allow an estimate of the solar abundances based on 'realistic' radiative transfer calculations. The Eulerian frame formalism in the context of Hot Jupiter models would also deliver new insights in this very interesting topic: This work showed that the global circulation has an influence on the formation of the spectrum, however, a detailed analysis is pending. The Eulerian frame formalism can also be used to calculate, e.g., the radiation field within and emerging from a circumstellar disk or interstellar moving medium models.

The application of the Eulerian frame formalism in radiative transfer problems in this work showed that the method has high computational demands in both, time and hardware. Appendix A gives an overview over this issue and explains how the formalism is implemented into the stellar atmosphere code PHOENIX. Furthermore, it gives an idea of how to speed up the calculation. Further improvements would be

- Opacity tables can be created so that the opacity can be read from a file during the radiative transfer calculation instead of being calculated in advance for every wavelength point and angle. Hard disks are slow but, in an Eulerian frame calculation, this would avoid the time to calculate the direction dependent opacities.
- The memory demands could be reduced by using single-precision.
- In a Eulerian frame calculation, the communication in the parallel implementation after the opacity calculation for every solid angle can be avoided. To achieve this, the spatial grid should not be distributed over the central processing units that work on a specific wavelength point but the parallelization should use optimized shared memory techniques². Then, a wavelength point should be computed on a single computer node and all central processing units on that node would have the number densities of the whole three dimensional grid. Finally, only the central processing units that do the formal solution for a specific solid angle calculate the opacity for that solid angle. This would avoid the communication because the central processing units have the necessary data already in their memory.

The Eulerian frame method can now be used in any atmosphere structure in cylindrical, cartesian and spherical coordinate systems with arbitrary velocity fields as long as the limitations are considered. This work provides, furthermore, a correct treatment of three dimensional radiative transfer for hydro-dynamical models of various atmospheres. It can be used as a module to account for the radiative feedback in those hydro-dynamical calculations when enough computer power will be available in the future.

²for example OpenMP or OpenCL

Appendix A

Implementation in PHOENIX/3D

This chapter describes technical details of the implementation of the Eulerian formalism into the stellar atmosphere code PHOENIX. It gives an insight into the internal domain decomposition in section A.1. In section A.2 the storage requirements and an idea of how to speed up the computation is given. Section A.3 outlines the handling of the Eulerian formalism in the PHOENIX/3D code.

A.1 Domain decomposition in PHOENIX/3D

With the increasing availability of supercomputers in the last years, computer codes describing physical problems advance very quickly. Depending on the specific physical problem and its complexity, the need to store physical quantities in the random access memory (RAM) can easily exceed available capacities. Nowadays supercomputers are usually set up as distributed memory systems, where central processing units (CPUs) are combined to shared memory multiprocessor (SMP) computer nodes. For example, the HLRN¹ supercomputer is using computer nodes with eight CPUs and 48 GB of RAM. To reduce the memory footprint in complex (physical) models a domain decomposition method is used that allows to store data only on computer nodes which are in need of it.

The stellar atmosphere code PHOENIX/3D has huge memory demands mainly because of the need to store the number densities of atoms and molecules and the three dimensional Λ^* operator in every volume element. For example, in a calculation with 1.000.000 volume elements and 1000 spectral lines and, therefore, 1000 number densities, the memory demands on, for example, each HLRN computer node would be

$$\begin{aligned} M(\text{number densities}) &\approx 7.4 \text{ GB} \times 8 \text{ CPUs} \approx 58 \text{ GB} \\ M(\Lambda^*) &\approx 0.4 \text{ GB} \times 8 \text{ CPUs} \approx 3.2 \text{ GB} \\ M(\text{total}) &\approx 61.2 \text{ GB}. \end{aligned}$$

This already exceeds nowadays capacities for only the storage of those two quantities, not even considering the other essential physical quantities as, for example, the temperature, pressure, radiative moments, etc. Therefore, PHOENIX is domain decomposed. The realization of domain decomposition in PHOENIX described in this section is explained for the spatial three dimensional part PHOENIX/3D as it will be important for the realization of the Eulerian formalism.

The treatment of radiative transfer in computer codes can be domain decomposed as follows: The total number of CPUs used in the calculation can be divided in CPUs

¹Norddeutscher Verbund für Hoch- und Höchstleistungsrechnen

that work on a specific wavelength point. All CPUs that work on a wavelength point are called, for example, a *wavelength cluster* (in short: wl-cluster). Furthermore, the wl-cluster CPUs can be subdivided in CPUs that work on different solid angle points. These CPUs can be called a *formal solution cluster* (in short: fs-cluster). All wl-cluster CPUs work on the computation of the opacity whereas only the subdivided fs-cluster CPUs work on the radiative transfer. For the computation of the opacity, the number densities must be known and, for the solution of the radiative transfer, the Λ^* operator has to be constructed.

To split up the memory demands for the storage of the number densities, every wl-cluster CPU works only in different regions of the spatial three dimensional grid. This reduces significantly the memory demand of a single wl-cluster CPU, as it stores only the number densities of a part of the spatial grid. When the opacity is calculated, which is only one number per volume element, the wl-cluster CPUs communicate with each other. After the communication, every wl-cluster CPU has the opacity of the whole spatial grid in its memory. As the fs-cluster CPUs are a subgroup of the wl-clusters CPUs, the opacity is also accessible for them. The storage of the number densities are kept spatially distributed over the wl-cluster CPUs.

The subdivision of the wl-cluster CPUs into fs-cluster CPUs has only an advantage, in terms of reducing the memory demands, when more computer nodes are used. The 3DRT module tracks characteristics globally through the spatial three dimensional grid. Therefore, a spatial division of the grid for the formal solution is not suitable. But the amount of fs-cluster CPUs per computer node reduces the memory demands on the node.

For example: Using eight computer nodes with eight CPUs on each node a total of 64 CPUs is available for the calculation. 32 CPUs (or four computer nodes) are used in a wl-cluster and four CPUs are used in the subdivided fs-cluster, the setup can be visualized as in figure A.1. Using the above example, the total storage requirements were 61.2 GB per node. Due to the spatial division of the grid onto the wl-cluster CPUs, every wl-cluster CPU has to store only 1/32 of the number densities. A computer node has to store, therefore, $1.9 \text{ GB} \times 8 \text{ CPUs} = 15.2 \text{ GB}$ of number density data. The four CPUs used in the fs-cluster per wl-cluster are distributed over the four computer nodes used, on every node only one CPU is working on the solution of the radiative transfer. This fs-cluster CPU has to store the Λ^* operator. The memory demands for the construction of the Λ^* operator on a computer node is, therefore, only $3.2 \text{ GB}/8 = 0.4 \text{ GB}$ - in the example above 3.2 GB of memory per node was necessary. Due to domain decomposition, the overall memory demands, for one node, are

$$\begin{aligned} &M(\text{number densities}) + M(\text{construction of } \Lambda^* \text{ on one CPU on that node}) \\ &\rightarrow 15.2 \text{ GB} + 0.4 \text{ GB} = 15.6 \text{ GB}. \end{aligned}$$

The memory requirement have been reduced by 45.6 GB per computer node. This makes the computation of the example setup feasible.

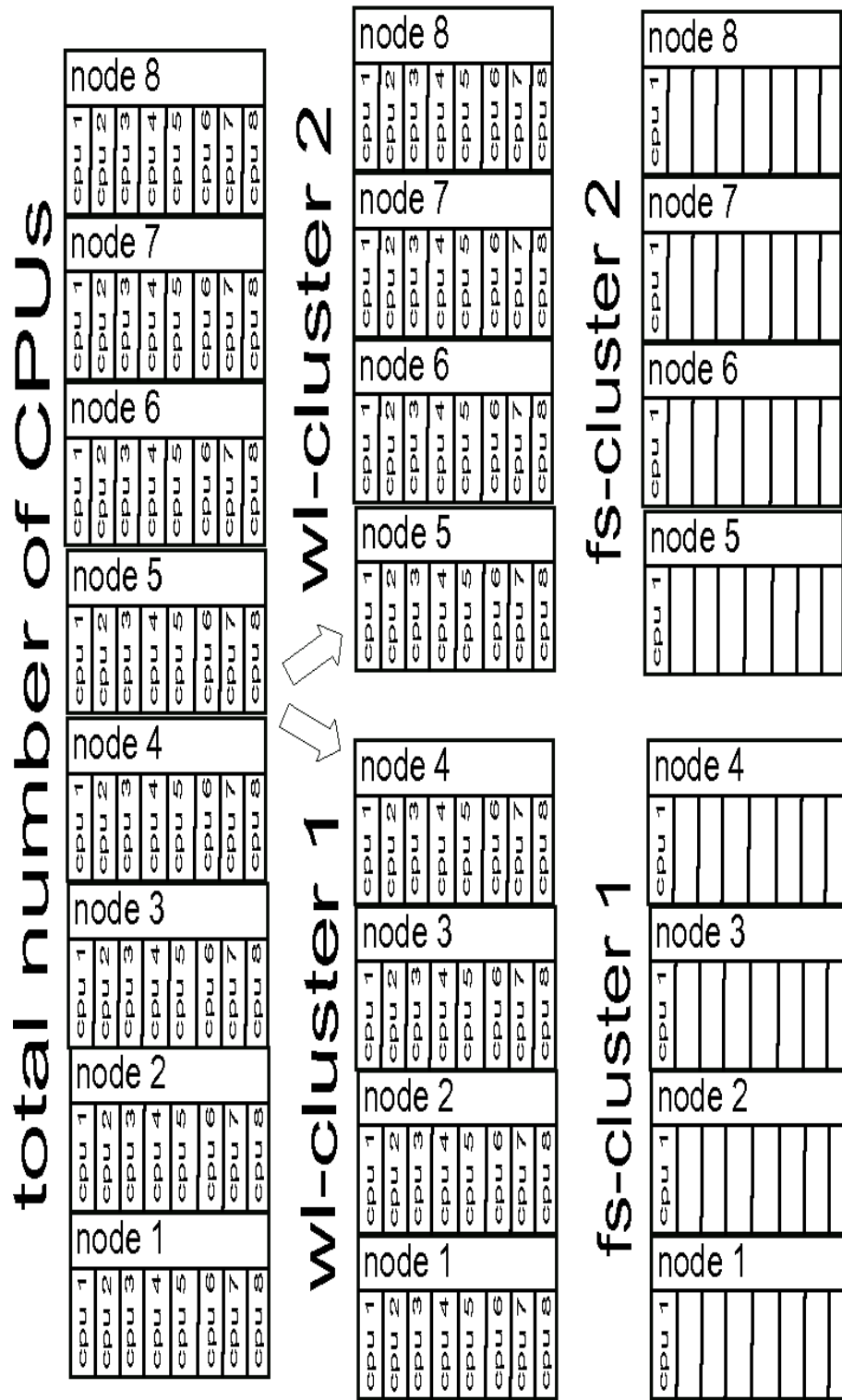


Figure A.1: Domain decomposition in the main PHOENIX/3D code

A.2 Numerical performance and storage issues

A basic demand in the Eulerian frame formalism, in terms of computer hardware requirements, is the storage of the angle-dependent opacities. In general, these calculations are very time consuming compared to the time needed to solve the radiative transfer equations in three spatial dimensions. Therefore, not only the fs-cluster CPUs are used to calculate the opacities which would be obvious as the opacities are angle dependent. The calculation is performed by the wl-cluster CPUs for every solid angle point used in the calculation, in the spatial region they have the number densities for. In the Eulerian frame formalism, the (opacity) communication within a wl-cluster has to be carried out for each solid angle point. After the communication it must be ensured that only the fs-cluster CPUs will have the solid-angle dependent opacities of the solid angle points they will work on. Depending on the usage of the Eulerian formalism, this data can be read from hard disk¹ or is kept in memory. If the opacities are saved on hard disk, the filename contains information about the wl-cluster and the specific solid angle point for which the opacities are calculated for. For the formal solution, those files are read, depending on the wl-cluster and the solid angle point a specific fs-cluster CPU is working on. When the opacities are kept in the RAM, it is ensured that they are only saved for the solid angle points a specific fs-cluster CPU will work on. This reduces the memory footprint of the algorithm. The demands on the hardware of the computer system, either if the opacities are saved on hard disk or kept in memory, is nevertheless huge in terms of storage requirements on hard disk or memory and in terms of computing time compared to the requirements of the rest of the code.²

Section A.2.1 explains the aspects of storing the opacities on hard disk or in memory and section A.2.2 gives an idea of how to optimize the computation in terms of reducing the computing time of the calculation.

A.2.1 Storage issues

The storage of the opacities on hard disk can be done in the ASCII file format or in binary file format. The ASCII format is suitable if a further investigation of the angle-dependent opacities is desired³. The binary format is optimal if not enough RAM is available in the computer system and a fast I/O is desired. The memory needed on the hard disk is, theoretically, as follows⁴

$$\text{GB to save} = (\text{number of wl-cluster}) \cdot \text{voxels} \cdot (n_{\theta,c} \cdot n_{\phi,c}) \cdot \frac{8 \text{ byte}}{1024^3}. \quad (\text{A.1})$$

The real size of the files is, of course, dependent on the file system and also on the file format. Binary saved files are smaller than files saved in the ASCII format.

When the opacities are kept in the RAM, the memory demands are⁵

$$\text{GB per FS_CPU} = \frac{1}{\text{FS_SIZE}} \cdot \text{voxels} \cdot (n_{\theta,c} \cdot n_{\phi,c}) \cdot \frac{8 \text{ byte}}{1024^3}, \quad (\text{A.2})$$

per fs-cluster CPU. To obtain the overall memory demand on a computer node, this value has to be added to the demands of storing the number densities and the Λ^* operator for

¹hard disks are slow compared to the memory, but in some cases it might be useful to use the hard disk

²this, of course, depends on the specific problem

³to do this, it must be ensured that the number of wavelength points equal the number of wl-clusters. If a wavelength cluster works on more than one wavelength point, the angle depended opacities files are overwritten

⁴it is assumed that double precision numbers are used

⁵see footnote 4

all CPUs on a compute node¹.

A.2.2 Overall speedup

The relation of time of the calculation to the number of CPUs used, cannot be linear within the Eulerian formalism. As the wl-cluster CPUs are working in different spatial regions of the three dimensional grid, they are using different temperatures to evaluate the Doppler width of a given spectral line. Therefore, the time to compute the opacity² depends on the spatial region. Before the communication within a specific wl-cluster for a specific solid angle point, all CPUs have to be finished with the opacity calculation. Therefore, CPUs which work in colder spatial regions have to wait for CPUs working in hot regions before the communication can be carried out. Furthermore, the time for the communication within a wl-cluster depends on the number of CPUs working in it and on the computer system.

The overall time for the opacity calculation is, of course, increasing with the number of spectral lines, the number of wavelength points, the number of voxels and the number of solid angle points used. Therefore, this section should only give an idea of how to minimize the time needed for the calculation of a specific problem. In the results presented here, only one Gaussian shaped spectral line was used³.

Figure A.2 shows the relation of the time needed for a computation of the spectrum to the number of CPUs used in a wl-cluster. Figure A.3 shows the corresponding times spend in the opacity calculation to the time spend to solve the radiative transfer equation. The figures show clearly that the total computation time is dominated by the fact that the wl-cluster CPUs have to communicate⁴ within a wl-cluster. The communication at a specific wavelength point can not be reduced because the opacity must be available in the whole spatial grid for every solid angle point.

Figures A.4 and A.5 show a different distribution of the total CPUs used in the calcu-

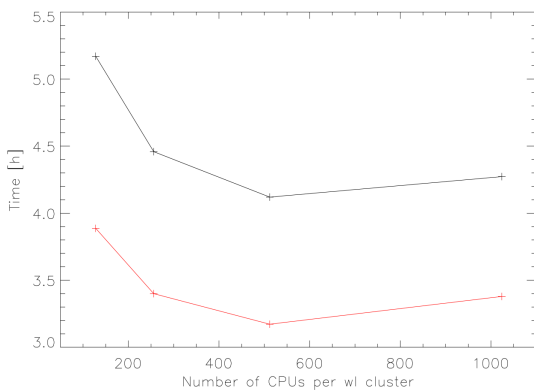


Figure A.2: Black: overall time for the calculation for a increasing number of CPUS per wl-cluster. Red: time spend in waiting for the other CPUs before the communication within a wl-cluster and the time for the communication itself.

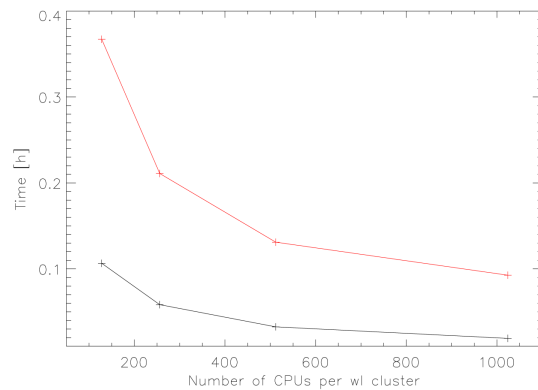


Figure A.3: Black: time for the opacity calculation and red: time for the solution of the radiative transfer. The graph shows the performance with a increasing number of CPUs per wl-cluster.

¹plus essential atmospheric data which is small compared to the opacities and number densities

²in other words: to compute the exponential function which is needed for the evaluation of the opacity

³therefore, the computing time and memory demands in the figures are 'small'

⁴and wait for each other before the communication

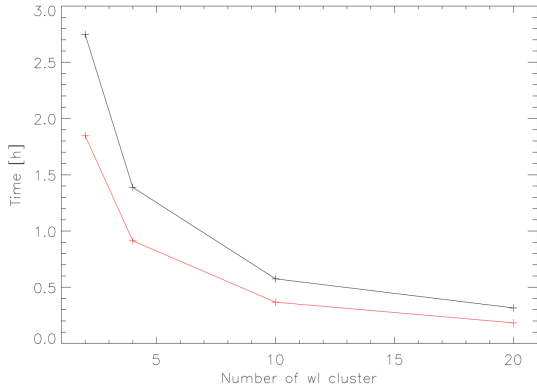


Figure A.4: Total time against number of wl-clusters. In every wl-cluster 64 CPUs are working. Black: total time and red: time for the communication

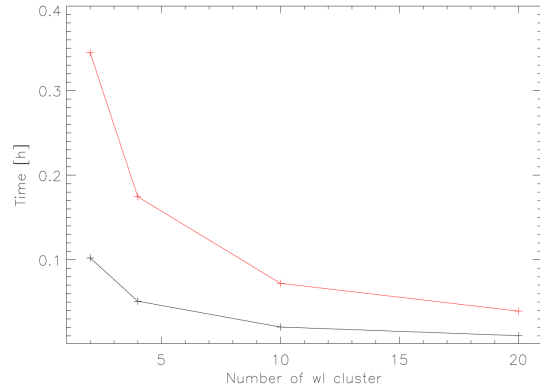


Figure A.5: Time for the opacity calculation (red) and time the solution of the radiative transfer (black) with increasing number of wl-clusters. In every wl-cluster 64 CPUs are working.

lation over the wl-clusters. Here, 64 CPUs are working in every wl-cluster. The increase of the number of wl-cluster significantly decreases the total computing time. Still, the computing time is dominated by the communication time, but it is decreased significantly by using more wl-clusters. The usage of more wl-clusters decreases the number of communications a single wl-cluster CPU has to do because it has to work on less wavelength points.

Figure A.6 shows the communication a single wl-cluster CPU has to accomplish for more CPUs per wl-cluster and more wl-clusters. The decrease in the number of communications is clearly visible.

On the other side, more CPUs per wl-cluster and, therefore, less wl-clusters are reducing the memory demand either on hard disk or in the RAM. Equations A.1 and A.2 are

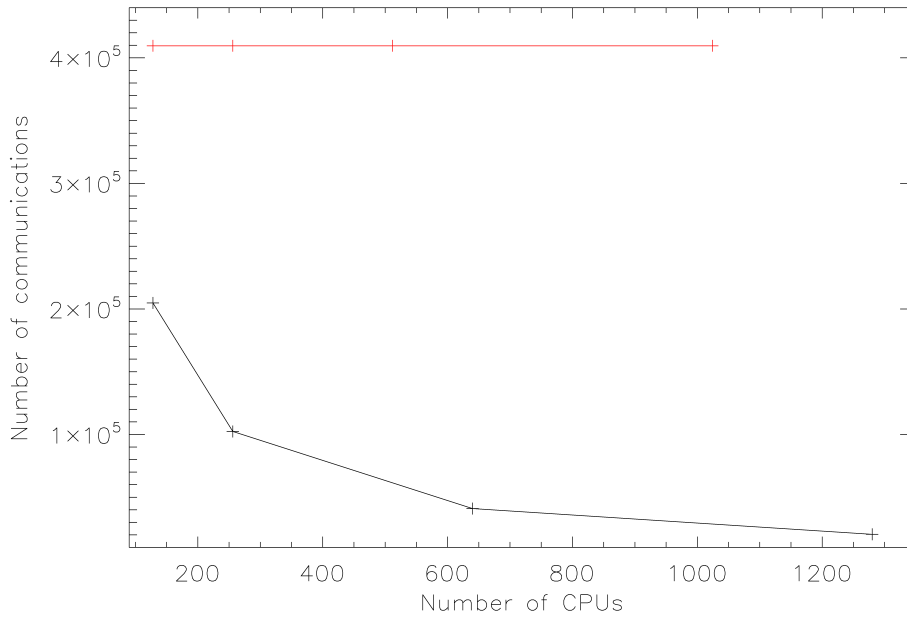


Figure A.6: Number of communication a single wl-cluster CPU has to accomplish. Black: Using more wl-cluster and red: using more CPUs per wl-cluster

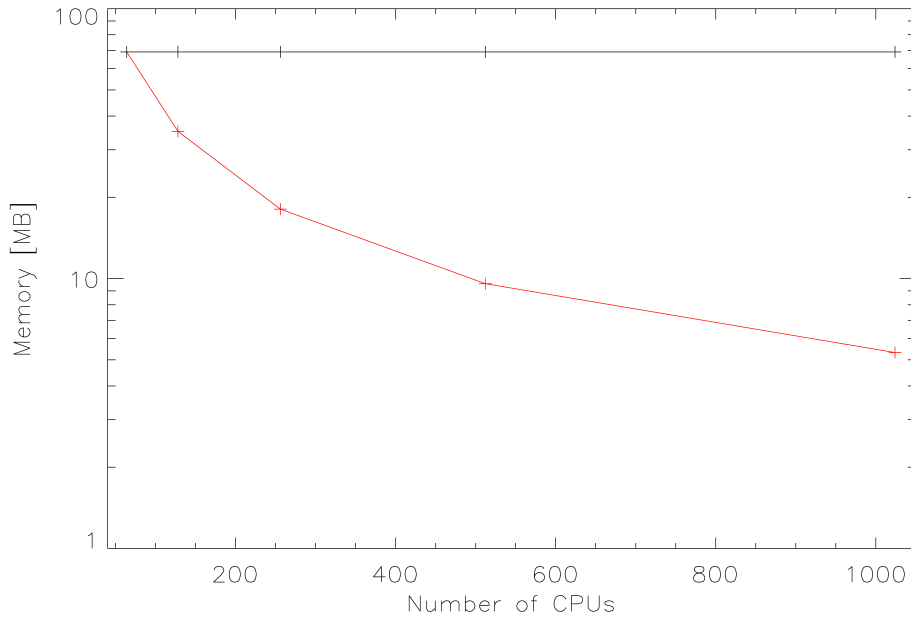


Figure A.7: Memory demands in the RAM for a single fs-cluster CPU in the Eulerian frame by either using more wl-cluster (black) or more CPUs per wl-cluster (red)

describing those demands. Figure A.7 shows the demands in the RAM for one CPU for the presented setups.

For an optimal speedup of an Eulerian frame calculation, a balance must be found between the available memory on hard disk or in RAM and the time for the opacity calculation with the number of wl-clusters. In general, the time for the opacity calculation can easily overtake the time for the solution of the radiative transfer and the communication time, depending on how many spectral lines, how many wavelength points, how many solid angle points and how many voxels are used in the calculation. But it is always desirable to reduce the communication time between the CPUs.

A.3 Logical variables regarding the Eulerian frame

This section describes shortly logical variables in PHOENIX/3D to manage the Eulerian frame formalism, in table A.1 those variables are listed. The `euler_test*` variables are used to test the construction of the $\bar{\Lambda}^{*,O}$ operator in the corresponding 3DRT setup. The `eulerian_mode*` enables the usage of the Eulerian frame in the setups. The parameter `euler_show_thermal_velocities` is very important for applications with atoms in LTE. To ensure that the formalism works correctly, the Doppler widths of the spectral lines in the desired atmosphere must be known to ensure that the wavelength displacement due to the velocity field at a specific wavelength point is taken into account in the opacity routines⁵. Therefore, all parameters of the desired atmosphere should be set up in the configuration file and `euler_show_thermal_velocities` should be set to `TRUE`⁶. Then a PHOENIX/3D run is needed to obtain the thermal velocities of the spectral lines. The output to `STDOUT` shows the thermal velocities and gives a suggestion of how to change the corresponding parameter in the configuration file. As the Doppler width does not

⁵the PHOENIX/3D parameter `gausswin` must be modified to account for this

⁶'true.' or simply 't'/'T' in fortran

variable	usage
<code>eulerian_mode_2lvl</code>	enables the two-level atom formulation with complete redistribution in the Eulerian frame routines.
<code>eulerian_mode</code>	enables the formulation of the Eulerian frame formalism for atoms in LTE and coherent scattering.
<code>euler_save_files</code>	enables the storage of the angle-dependent opacities on hard disk.
<code>use_binary_files_euler</code>	writes the data in binary file format.
<code>euler_test_lstar</code>	enables the test construction of the $\Lambda^{O,*}$ operator in the Eulerian frame routines.
<code>euler_test_lstarBAR</code>	enables the test construction of the $\Lambda^{O,*}$ operator in the Eulerian frame routines. Only used in the two-level atom setup.
<code>euler_show_thermal_velocities</code>	enable the output of the thermal velocities and Doppler widths of the spectral lines used for the adjustment of the search window for the Eulerian frame formalism. Works only for atoms in LTE.

Table A.1: Logical variables in PHOENIX/3D to control the Eulerian frame formalism

depend on the shape of the spectral line, this approach is only implemented for Gaussian shaped lines. The time needed to perform that calculation depends only on the number of wavelength points and the number of voxels as no radiation field is calculated. Then `euler_show_thermal_velocities` is set to `FALSE` and the spectrum should be calculated with the same configuration file.

Appendix B

Doppler widths

Rest wavelength [\AA]	v_{th} [cm/h]	Doppler width [\AA]	Rest wavelength [\AA]	v_{th} [cm/h]	Doppler width [\AA]
6554.0698	2.48270E+05	5.42768E-02	6559.8235	2.31560E+05	5.06681E-02
6554.0894	2.48270E+05	5.42769E-02	6560.0104	2.35443E+05	5.15192E-02
6554.1058	2.28963E+05	5.00562E-02	6560.3712	2.29410E+05	5.02020E-02
6554.1484	2.28963E+05	5.00565E-02	6560.4926	2.35443E+05	5.15230E-02
6554.3385	2.29410E+05	5.01558E-02	6560.7386	2.11684E+05	4.63255E-02
6554.4565	2.27642E+05	4.97702E-02	6561.3291	2.28963E+05	5.01113E-02
6554.4860	2.33441E+05	5.10382E-02	6561.4013	2.33441E+05	5.10920E-02
6554.8628	2.11684E+05	4.62840E-02	6561.5817	2.28963E+05	5.01133E-02
6555.0267	2.27642E+05	4.97745E-02	6561.6408	2.48270E+05	5.43395E-02
6555.3151	2.29410E+05	5.01633E-02	6561.6539	2.30962E+05	5.05515E-02
6555.4463	2.28963E+05	5.00664E-02	6561.6736	2.48270E+05	5.43397E-02
6555.4790	2.28963E+05	5.00667E-02	6561.6834	2.28963E+05	5.01141E-02
6555.4856	2.29410E+05	5.01646E-02	6561.7523	2.28963E+05	5.01146E-02
6555.5315	2.30962E+05	5.05043E-02	6561.8705	2.07341E+05	4.53828E-02
6555.5643	2.28963E+05	5.00673E-02	6562.0148	2.28963E+05	5.01166E-02
6555.6593	2.28963E+05	5.00680E-02	6562.0903	2.28963E+05	5.01172E-02
6555.6691	2.33441E+05	5.10474E-02	6562.1001	2.28963E+05	5.01172E-02
6555.6823	2.31560E+05	5.06361E-02	6562.1067	2.28963E+05	5.01173E-02
6555.6921	2.54369E+05	5.56240E-02	6562.2543	2.48270E+05	5.43445E-02
6555.7052	2.31560E+05	5.06363E-02	6562.2543	2.48270E+05	5.43445E-02
6555.7478	2.28963E+05	5.00687E-02	6562.2543	2.48270E+05	5.43445E-02
6555.8625	2.48270E+05	5.42916E-02	6562.2707	2.28963E+05	5.01185E-02
6555.9576	2.27537E+05	4.97584E-02	6562.3790	2.54369E+05	5.56808E-02
6555.9576	2.27537E+05	4.97584E-02	6562.9204	2.28963E+05	5.01235E-02
6556.0330	2.33441E+05	5.10502E-02	6563.1141	2.33441E+05	5.11053E-02
6556.1707	2.27537E+05	4.97601E-02	6563.2847	2.28963E+05	5.01263E-02
6556.3313	2.28963E+05	5.00732E-02	6563.7146	2.54369E+05	5.56921E-02
6556.3542	2.28963E+05	5.00734E-02	6563.7638	2.31560E+05	5.06985E-02
6556.5280	2.48270E+05	5.42971E-02	6563.8328	2.28963E+05	5.01305E-02
6556.6395	2.33441E+05	5.10549E-02	6564.0133	2.28963E+05	5.01318E-02
6556.8034	2.33441E+05	5.10562E-02	6564.1905	2.28963E+05	5.01332E-02
6557.0066	2.28963E+05	5.00783E-02	6564.2200	2.31560E+05	5.07020E-02
6557.0132	2.33441E+05	5.10578E-02	6564.3119	2.28963E+05	5.01341E-02
6557.2722	2.54369E+05	5.56374E-02	6564.3710	2.28963E+05	5.01346E-02
6557.4460	2.33441E+05	5.10612E-02	6564.6106	8.53451E+05	1.86882E-01
6557.4984	2.29410E+05	5.01800E-02	6564.7813	2.33441E+05	5.11183E-02
6557.5050	2.28963E+05	5.00821E-02	6565.0636	2.48270E+05	5.43678E-02
6557.6394	2.27642E+05	4.97943E-02	6565.0636	2.28963E+05	5.01399E-02
6557.6788	2.28963E+05	5.00835E-02	6565.2113	2.27537E+05	4.98287E-02
6557.6788	2.27537E+05	4.97715E-02	6565.2999	2.39399E+05	5.24270E-02
6557.8722	2.33441E+05	5.10645E-02	6565.4181	2.28963E+05	5.01426E-02
6558.1313	2.28963E+05	5.00869E-02	6565.5264	2.27537E+05	4.98311E-02
6558.1378	2.10115E+05	4.59638E-02	6565.5724	2.48270E+05	5.43720E-02
6558.3182	2.54369E+05	5.56463E-02	6565.5790	2.29410E+05	5.02418E-02
6558.3182	2.54369E+05	5.56463E-02	6565.6085	2.27537E+05	4.98317E-02
6558.5969	2.28963E+05	5.00905E-02	6565.6118	2.48270E+05	5.43724E-02
6558.6428	2.54369E+05	5.56491E-02	6565.6578	2.48270E+05	5.43727E-02
6558.7576	2.30962E+05	5.05292E-02	6565.6578	2.48270E+05	5.43727E-02
6558.7641	2.28963E+05	5.00918E-02	6565.9499	2.30962E+05	5.05846E-02
6558.7674	3.12676E+05	6.84064E-02	6566.0714	2.33441E+05	5.11284E-02
6558.7969	2.28963E+05	5.00920E-02	6566.0878	2.28963E+05	5.01477E-02
6558.9445	2.27537E+05	4.97811E-02	6566.3373	2.30962E+05	5.05876E-02
6558.9445	2.27537E+05	4.97811E-02	6566.4030	2.54369E+05	5.57149E-02
6559.0232	2.33441E+05	5.10735E-02	6566.4161	2.11953E+05	4.64244E-02
6559.0724	2.33441E+05	5.10739E-02	6566.4719	2.28963E+05	5.01506E-02
6559.1806	2.18641E+05	4.78366E-02	6566.4752	2.28963E+05	5.01506E-02
6559.2200	2.28963E+05	5.00952E-02	6566.4884	2.28963E+05	5.01508E-02
6559.2594	2.28963E+05	5.00955E-02	6566.5573	2.28963E+05	5.01513E-02
6559.6300	2.54369E+05	5.56574E-02	6566.6361	2.48270E+05	5.43808E-02
6559.6398	2.35443E+05	5.15163E-02	6566.6361	2.48270E+05	5.43808E-02
6559.8169	2.29410E+05	5.01977E-02	6566.6361	2.48270E+05	5.43808E-02

Table B.1: Rest wavelengths, the minimum of the thermal velocities and Doppler widths in the whole three dimensional grid for the spectral lines in chapters 6 and 7.

Bibliography

- Allard, F. & Hauschildt, P. H. (1995), ‘Model atmospheres for M (sub)dwarf stars. 1: The base model grid’, *ApJ* **445**, 433–450.
- Asplund, M. (2000), ‘Line formation in solar granulation. III. The photospheric Si and meteoritic Fe abundances’, *A&A* **359**, 755–758.
- Asplund, M., Grevesse, N. & Sauval, A. J. (2005), The Solar Chemical Composition, *in* T. G. Barnes III & F. N. Bash, ed., ‘Cosmic Abundances as Records of Stellar Evolution and Nucleosynthesis’, Vol. 336 of *Astronomical Society of the Pacific Conference Series*, pp. 25–+.
- Auer, L. H. & van Blerkom, D. (1972), ‘Electron Scattering in Spherically Expanding Envelopes’, *ApJ* **178**, 175–182.
- Avrett, E. H. (1965), ‘Solutions of the Two-Level Line Transfer Problem with Complete Redistribution’, *SAO Special Report* **174**, 101–+.
- Baron, E. & Hauschildt, P. H. (2004), ‘Co-moving frame radiative transfer in spherical media with arbitrary velocity fields’, *A&A* **427**, 987–994.
- Baron, E. & Hauschildt, P. H. (2007), ‘A 3D radiative transfer framework. II. Line transfer problems’, *A&A* **468**, 255–261.
- Baron, E. & Hauschildt, P. H. (2009), 3-D Radiative Transfer in the Next Decade, *in* ‘astro2010: The Astronomy and Astrophysics Decadal Survey’, Vol. 2010 of *ArXiv Astrophysics e-prints*, pp. 11–+.
- Baron, E., Hauschildt, P. H. & Chen, B. (2009), ‘A 3D radiative transfer framework. V. Homologous flows’, *A&A* **498**, 987–992.
- Böhm-Vitense, E. (1958), ‘Über die Wasserstoffkonvektionszone in Sternen verschiedener Effektivtemperaturen und Leuchtkräfte. Mit 5 Textabbildungen’, *ZAp* **46**, 108–+.
- Caffau, E., Steffen, M., Sbordone, L., Ludwig, H. & Bonifacio, P. (2007), ‘The solar photospheric abundance of phosphorus: results from CO⁵BOLD 3D model atmospheres’, *A&A* **473**, L9–L12.
- Cannon, C. J. (1973), ‘Angular quadrature perturbations in radiative transfer theory.’, *Journal of Quantitative Spectroscopy and Radiative Transfer* **13**, 627–633.
- Canuto, V. M. & Mazzitelli, I. (1991), ‘Stellar turbulent convection - A new model and applications’, *ApJ* **370**, 295–311.
-

- Caroff, L. J., Noerdlinger, P. D. & Scargle, J. D. (1972), ‘Transfer of Resonance-Line Radiation in Differentially Expanding Atmospheres. I. General Considerations and Monte Carlo Calculations’, *ApJ* **176**, 439–+.
- Castor, J. I. (1970), ‘Spectral line formation in Wolf-Rayet envelopes.’, *MNRAS* **149**, 111–127.
- Castor, J. I. (1972), ‘Radiative Transfer in Spherically Symmetric Flows’, *ApJ* **178**, 779–792.
- de Groot, M. & Sterken, C., eds (2001), *P Cygni 2000 - Four hundred years of progress*, Vol. 233 of *Astronomical Society of the Pacific Conference Series*.
- Dravins, D. (1987*a*), ‘Stellar Granulation - Part Two - Stellar Photospheric Line Asymmetries’, *A&A* **172**, 211–+.
- Dravins, D. (1987*b*), ‘Stellar granulation. I - The observability of stellar photospheric convection’, *A&A* **172**, 200–224.
- Freytag, B., Steffen, M., Ludwig, H. & Wedemeyer-Boehm, S. (2008), ‘Radiation hydrodynamics simulations of stellar surface convection’, *Astrophysics Software Database* pp. 36–+.
- Gray, D. F. (2008), *The Observation and Analysis of Stellar Photospheres*.
- Hauschildt, P. H. (1992*a*), ‘A fast operator perturbation method for the solution of the special relativistic equation of radiative transfer in spherical symmetry’, *J. Quant. Spec. Radiat. Transf.* **47**, 433–453.
- Hauschildt, P. H. (1992*b*), ‘A fast operator perturbation method for the solution of the special relativistic equation of radiative transfer in spherical symmetry’, *J. Quant. Spec. Radiat. Transf.* **47**, 433–453.
- Hauschildt, P. H. & Baron, E. (2006), ‘A 3D radiative transfer framework. I. Non-local operator splitting and continuum scattering problems’, *A&A* **451**, 273–284.
- Hauschildt, P. H. & Baron, E. (2008), ‘A 3D radiative transfer framework. III. Periodic boundary conditions’, *A&A* **490**, 873–877.
- Hauschildt, P. H. & Baron, E. (2010), ‘A 3D radiative transfer framework. VI. PHOENIX/3D example applications’, *A&A* **509**, A36+.
- Hauschildt, P. H. & Wehrse, R. (1991), ‘Solution of the special relativistic equation of radiative transfer in rapidly expanding spherical shells’, *J. Quant. Spec. Radiat. Transf.* **46**, 81–98.
- Hauschildt, P. H., Störzer, H. & Baron, E. (1994), ‘Convergence properties of the accelerated Λ -iteration method for the solution of radiative transfer problems.’, *J. Quant. Spec. Radiat. Transf.* **51**, 875–891.
- Labs, D. (1950), ‘Eine einfache Näherungslösung für das Strahlungsgleichgewicht einer ‘grauen’ Atmosphäre’, *Z. Astrophysik* **27**, 153.
- Magnan, C. (1970), ‘Monte-Carlo calculation of line profiles in expanding and rotating atmospheres.’, *J. Quant. Spec. Radiat. Transf.* **10**, 1–9.
-

- Mayor, M. & Queloz, D. (1995), ‘A Jupiter-mass companion to a solar-type star’, *Nature* **378**, 355–359.
- McCrea, W. H. & Mitra, K. K. (1936), ‘Schuster’s Problem for a Moving Atmosphere. Mit 5 Abbildungen.’, *ZAp* **11**, 359–+.
- Menou, K. & Rauscher, E. (2009), ‘Atmospheric Circulation of Hot Jupiters: A Shallow Three-Dimensional Model’, *ApJ* **700**, 887–897.
- Menou, K. & Rauscher, E. (2010), ‘Radiation Hydrodynamics of Hot Jupiter Atmospheres’, *ApJ* **713**, 1174–1182.
- Mihalas, D. (1970), *Stellar atmospheres*, Series of Books in Astronomy and Astrophysics, San Francisco: Freeman, —c1970.
- Mihalas, D. (1978), *Stellar atmospheres /2nd edition/*, San Francisco, W. H. Freeman and Co., 1978. 650 p.
- Mihalas, D. (1980), ‘Solution of the comoving-frame equation of transfer in spherically symmetric flows. VI - Relativistic flows’, *ApJ* **237**, 574–589.
- Mihalas, D., Kunasz, P. B. & Hummer, D. G. (1975), ‘Solution of the comoving frame equation of transfer in spherically symmetric flows. I - Computational method for equivalent-two-level-atom source functions’, *ApJ* **202**, 465–489.
- Mihalas, D., Kunasz, P. B. & Hummer, D. G. (1976), ‘Solution of the Comoving-Frame Equation of Transfer in Spherically Symmetric Flows. III. Effect of Aberration and Advection Terms’, *ApJ* **206**, 515–524.
- Ng, K.-C. (1974), ‘Hypernetted chain solutions for the classical one-component plasma up to Gamma equals 7000’, *J. Chem. Phys.* **61**, 2680–2689.
- Olson, G. L. & Kunasz, P. B. (1987), ‘Short characteristic solution of the non-LTE transfer problem by operator perturbation. I. The one-dimensional planar slab.’, *Journal of Quantitative Spectroscopy and Radiative Transfer* **38**, 325–336.
- Olson, G. L., Auer, L. H. & Buchler, J. R. (1986), ‘A rapidly convergent iterative solution of the non-LTE line radiation transfer problem’, *J. Quant. Spec. Radiat. Transf.* **35**, 431–442.
- Peraiah, A. (2001), *An Introduction to Radiative Transfer*, Cambridge University Press.
- Press, W. H., Teukolsky, S. A., Vetterling, W. T. & Flannery, B. P. (1992), *Numerical recipes in FORTRAN. The art of scientific computing*.
- Rauscher, E. & Menou, K. (2010), ‘Three-dimensional Modeling of Hot Jupiter Atmospheric Flows’, *ApJ* **714**, 1334–1342.
- Rutten, R. (2003), *Radiative Transfer in Stellar Atmospheres*, Utrecht University lecture notes, 8th edition.
- Rybicki, G. (1970), ‘Spectrum Formation in Stars with Steady State Extended Atmospheres’.
- Scharmer, G. B. (1981), ‘Solutions to radiative transfer problems using approximate lambda operators’, *ApJ* **249**, 720–730.
-

- Schuster, A. (1905), 'Radiation Through a Foggy Atmosphere', *ApJ* **21**, 1–+.
- Wedemeyer, S., Freytag, B., Steffen, M., Ludwig, H. & Holweger, H. (2004), 'Numerical simulation of the three-dimensional structure and dynamics of the non-magnetic solar chromosphere', *A&A* **414**, 1121–1137.
- Wehrse, R. & Kalkofen, W. (2006), 'Advances in radiative transfer', *A&A Rev.* **13**, 3–29.
-

Acknowledgments

Zunächst möchte ich bei Peter für die vier wundervolle Jahre an der Hamburger Sternwarte, für die Betreuung meiner Arbeit und für das lockere Arbeitsklima in der Theoriegruppe bedanken.

Andreas möchte ich für seine Geduld mit allen von uns, für seinen Überblick und Scharfsinn in jeglicher Hinsicht und seinen Frohsinn danken - oft war sein Lachen der erste Schritt Probleme zu lösen.

Dank gebührt auch meinen langjährigen Bürokollegen Soeren und Marianna: Vielen Dank für das entspannte Klima in unserem Büro und die unzähligen Diskussionen über die Physik, die Welt und überhaupt.

Dank auch den Korrekturlesern und den anderen Gruppenmitgliedern: Dennis, Veronica, Knop,....

Meinen Eltern danke ich für jegliche Unterstützung in den letzten Jahren, nicht nur finanzieller Art sondern auch für Kraft und Verständniss das sie mir mit auf den Weg gegeben haben.

Du das alles nicht mehr erlebt Oma, dir hätte das alles sehr gefallen - Du wärest ja so gerne mit nach Hamburg gekommen. Danke für die unvergessene Zeit mit dir.

Miss Denmark my love, thanks for the support over the last years, your intelligence and for being like you are.